UNIVERSITY OF CALIFORNIA
RIVERSIDE

Modeling and Analysis of Fluid Driven Fracture Propagation under the Plane Strain Condition

A Dissertation submitted in partial satisfaction
of the requirements for the degree of

Doctor of Philosophy

in

Mechanical Engineering

by

Young Hoon Kim

March 2013

Dissertation Committee:

Dr. Guanshui Xu, Chairperson
Dr. Javier Garay
Dr. David Oglesby

The Dissertation of Young Hoon Kim is approved:

Committee Chairperson

University of California, Riverside

Acknowledgments

I would like to express my gratitude to my advisor, Professor Guanshui Xu, for his support, patience, and encouragement throughout my graduate studies. As my teacher and mentor, he has taught me more than I could ever give him credit for here. During my time as his student he frequently had more faith in me than I had in myself and he has always built my confidence and sustained faith in my abilities. He has also shown me, by his example, what a good scientist and engineer should be.

My thanks also go to the members of my dissertation committee, Professor Javier Garay and Professor David Oglesby for their willingness to serve on the committee, and for their valuable suggestions and efforts in reviewing this dissertation.

I thank to my former advisor Professor Qing Jiang, guided me through the previous research on micro-electromechanical systems.

In particular, I wish to acknowledge the Republic of Korea Navy for giving me an excellent opportunity to study in United States.

Last, but not least, I would like to thank my wife Yunju for her understanding and love during the past few years. Her support and encouragement was in the end what made this dissertation possible.

To my parents, my wife Yunju and my beautiful children Haein and Haechan

for all their loving support

and to the memory of my beloved grandfather.

ABSTRACT OF THE DISSERTATION

Modeling and Analysis of Fluid Driven Fracture Propagation
under the Plane Strain Condition

by

Young Hoon Kim

Doctor of Philosophy, Graduate Program in Mechanical Engineering
University of California, Riverside, March 2013
Dr. Guanshui Xu, Chairperson

The process of fracture propagation driven by the pressure of the fluid flow between the fracture surfaces has been of considerable interest for understanding natural geological phenomena such as the formation of volcanic dikes and developing hydraulic fracturing technologies for industrial applications. Man-made hydraulic fracturing has been most commonly used for stimulation of oil and gas reservoirs to increase hydrocarbon production, stimulation of geothermal reservoirs, remediation of soil and groundwater aquifers, injection of wastes, goafing and fault reactivation in mining, and measurement of underground in situ stresses. Computational modeling and simulation of fluid driven fracture propagation in realistic geological formation has been a challenging problem because of various complexities including formation heterogeneities and the use of highly nonlinear engineered fluids. At present, one of the main obstacles for the robust industrial application of the simulating technology is the computational efficiency and stability. The objective of this study is to investigate the numerical efficiency and stability of various algorithms that can be potentially used in modeling of fluid driven fracture propagation. For simplicity, we have focused on fracture

propagation in the plane strain condition. The fracture is assumed to in homogeneous linear elastic medium and modeled using displacement discontinuity boundary element method (DDBEM). The nonlinear power-law fluid flow is modeled using conventional lubrication theory. The coupled equations are then discretized using zero order elements for its efficiency. The coupled equations become increasingly stiff and difficulty to solve when the power law indices become smaller. Various numerical algorithms such as Newton iteration with line search, trust-region and quasi-Newton method are investigated and compared. We have also extended the model to the fluid driven non-planar fracture propagation. A numerical crack propagation criterion based on the minimum local shear stress under mixed loading condition is proposed and compared with conventional theoretical and numerical criteria. The new crack propagation criterion provides more accurate and smooth crack initiation paths. Finally we have studied the geomechanics interaction between two simultaneous fluid driven fractures. The results provided some useful inputs for optimal design of multiple stage and multiple fracturing treatments along horizontal wells currently adopted by the oil and gas industry for the economical recovery of unconventional resources such as shale gas and oil.

Contents

List of Figures

List of Tables

Part I

Modeling and Analysis of Fluid Driven Fracture Propagation under the Plane Strain Condition

Chapter 1

Introduction

1.1 Hydraulic fracturing

The petroleum engineering mainly focuses on estimation of the recoverable volume of oil and gas trapped in porous rock formation subjected to high in-situ stress. This is related with many disciplines, such as drilling, production, operation, reservoir evaluation, reservoir stimulation, oil and gas facilities engineering. The hydraulic fracturing is one of the methods used in reservoir stimulation and nowadays this plays the most important role in petroleum engineering.

Hydraulic fracturing is a process to make channels from well bore to the rock formations that contain oil or gas. The channel is created by designed crack propagation due to an internal flow of pressurized fluid. During the production stage, when the fluid pressure is removed, the crack is closed due to existing in-situ stress. But the conductive channels for oil or gas is maintained by sands or sand-like proppants that mixed and transported by fracturing fluid. Consequently, the permeability of rock formation is increased and oil or gas

can flow through the fractured formation and seep into well bore. It has been proved that the hydraulic fracturing technology have improved the production efficiency and recovery of oil and gas in history. And it also increases the recoverable reserves of oil and natural gas [1–3]. After the first hydraulic fracturing is performed in Kansas by Stanolind Oil in 1947 on a gas well in the Hugoton field, approximately 2.5 million hydraulic fracture operations have been conducted world wide and it is reported that 60% of current drilled wells use hydraulic fracturing [4].

In usual hydraulic fracturing, wells are drilled straight down, vertically through the pay zone. The conventional vertical drilling would need to drill and fracture multiple wells to cover the area. Commonly, such a solution is not very economically rewarding. Recently, using advanced drilling technology, such as coiled tubing and horizontal driller, the horizontal drilled well was introduced. In horizontal drilling, the well is first drilled straight down, then slowly turn the drilled well horizontally within the rock formation with the turn radius of 300-500 feet. Then continue to drill for several thousand meters more in horizontal direction. By this technology, the well has a pay zone of several thousand feet as shown in Fig. 1.1. The horizontal drilling also allow us to exploit previously determined uneconomic area [5]. The horizontal well is currently limited to the the reservoir that the vertical well is not economically rewarding because the cost of horizontal well is three times expensive than the cost of vertical wells. In such condition, the production of horizontal well is 2.5 to 7 times the rate and reserves of vertical well [6].

The hydraulic fracturing treatment begins with the creation of initial path for the fracture. In this process called perforation, a specially designed explosive charge makes a deep hole

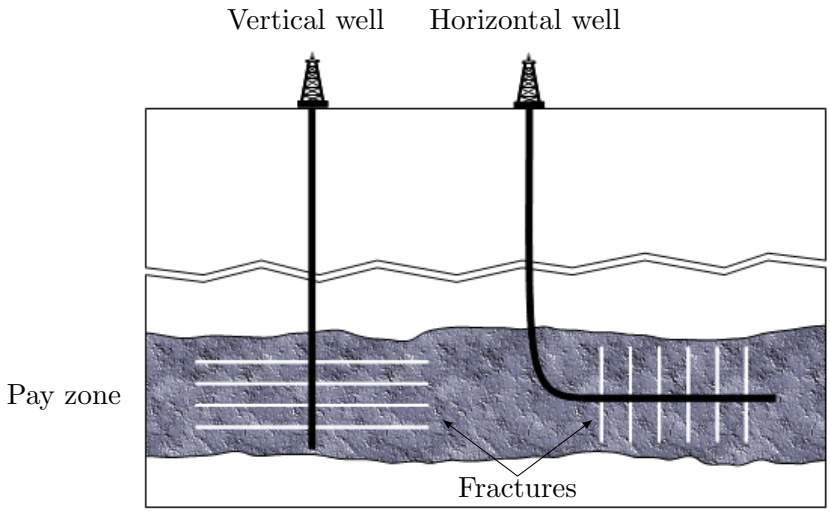

Figure 1.1: Vertical and horizontal wells

through the casing and rock formation. Then, viscous fracturing fluid is injected into well bore at high pressure. When the fluid pressure inside man-made crack in rock formation exceeds the in-situ stress plus the tensile stress of rock, tensile failure or splitting of rock occurs. The length and width of crack is basically increases as long as the fluid pressure is maintained. The crack will grow in the direction having minimum resistance and eventually propagates along the direction to the smallest principal stress in formation [7].

In-site fracture geometry design involves the situation of pay zone, such as in-situ stress profile, formation permeability, formation modulus, etc and it also includes estimation of the required resources, such as volume of fluid, injection time, hydraulic horse power for pumping and schedule, selection of propping agent and amount, etc [8]. The recent hydraulic fracturing job uses from 60,000 gal of fluid and 100,000 lbm of propping agents to the maximum of 1 million fluid and 5 million proppants in the largest fracturing treatment [4]. Therefore, accurate prediction of crack propagation is the most essential process to optimize the design of hydraulic fracturing and for efficient use resources.

1.2 Numerical models of hydraulic fracturing

As hydraulic fracturing becomes an essential stimulation technique for oil and gas productions, there has long been great interest in understanding how hydraulic fractures grow in certain conditions. Because the cracks are growing thousands of feet below the ground, predicting physical behavior of crack propagation has been quite challenging. There are two classical models of fracture geometry exist. The first crack propagation model for breaking rock formation using Sneddon's plane strain crack solution is proposed by Perkins and Kern in 1961 [9, 10]. This model is improved by Nordgren who includes fluid loss effect in the model [11]. The another important model is developed by Khristianovic and Zheltov, and also by Greertsma and de Klerk [12, 13] in 1955 and 1969, respectively. This model is adapted to the power-law fluids case by Daneshy [14]. The first model is called Perkins-Kern-Nordgren (PKN) model and the later is called Kristonovich-Geertsma-Daneshy (KGD) model. The schematics of these two basic models are illustrated in Fig. 1.2.

The most of early hydraulic fracturing models were designed by applying one of these models. The PKN model have limited hight but relatively large length whereas the KGD model is height independent and plane strain condition is applied to horizontal plane. Therefore, the PKN model is normally used when the fracture length is much greater than the fracture height, while the KGD model is used if fracture height is more larger than the fracture length [16]. Generally, either of these two models can be used in certain formations to design hydraulic fractures. The major purpose of using hydraulic fracturing models to make better decisions in process, rather than trying to determine accurate dimensions of fracture. In fracture design process, the estimated geometry from model calculations must be com-

(a) PKN model

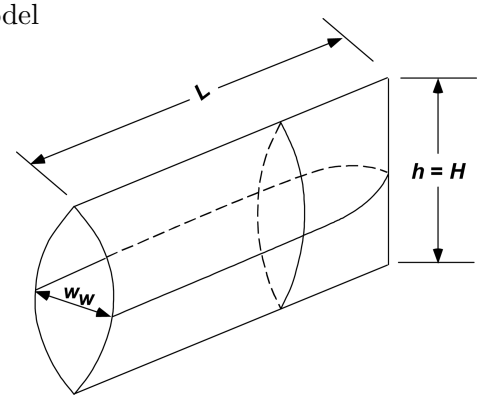

(b) KGD model

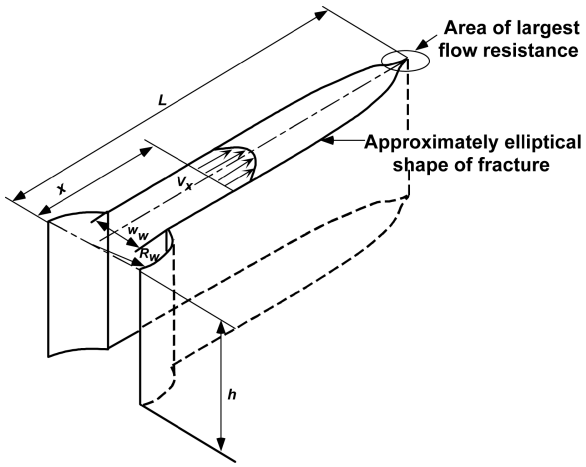

Figure 1.2: PKN and KGD geometries [15]

pared with actual results. By this calibrating process of fracture models with field results, the models can be used to make design changes and improve the success of stimulation treatments. If the correct fracture height value and the other parameters, such as in-situ stress, shear modulus, formation permeability, and total leak-off coefficient are reasonably known and used in the models, it will provide more accurate estimates of created fracture length and width [8].

Although significant progress has been made in engineering hydraulic fracturing treatments

as described earlier, numerical solutions for hydraulic fractures, especially the prediction of crack propagation driven by non-Newtonian fluid is still difficult because of the nonlinearity of the equation governing the flow of fluid in the fracture and the nonlocal character of the elastic response. This difficulty is caused by three important physical facts. First, the local opening displacements of crack is depends on not only the local fluid pressure but also the fluid pressure at another point. Second, the rate of local fluid flow is depends highly on the local crack opening displacement and power-law index of fluid. Third, the process is time dependent, in which the fracture propagates with an unknown speed, which also changes with time. Numerous efforts to overcome the complexity of fracture geometry by improving the classical models or to develop new hydraulic fracturing model have been made in decades from two dimensional model to pseudo three dimensional and fully three dimensional [15, 17–32].

The most of given models are based on fixed or moving mesh along the crack path and also the surrounding area. With significant improvements in hydraulic fracturing treatment technology, such as the simultaneous fracturing and horizontal drilling, the fractured area becomes more large and complicated which means the total number of required elements also rapidly increases and costs massive computations for the prediction of fracture geometry. Therefore, the need of more efficient numerical model of hydraulic fracturing arises. Our research focuses on developing an efficient and robust numerical model of crack propagation driven by internal fluid flow which applicable to the complicated and large fractured area problem.

Chapter 2

Crack opening displacement

2.1 Stress field and dislocation

Consider a plane crack having a width $2L$ located at the region $-L < x < L$ and $y = 0$ in a two dimensional body subjected to uniform tension $\sigma_{yy} = S$ at its remote boundaries as shown in Figure 2.1. The analytical solution for this problem can be obtained by applying

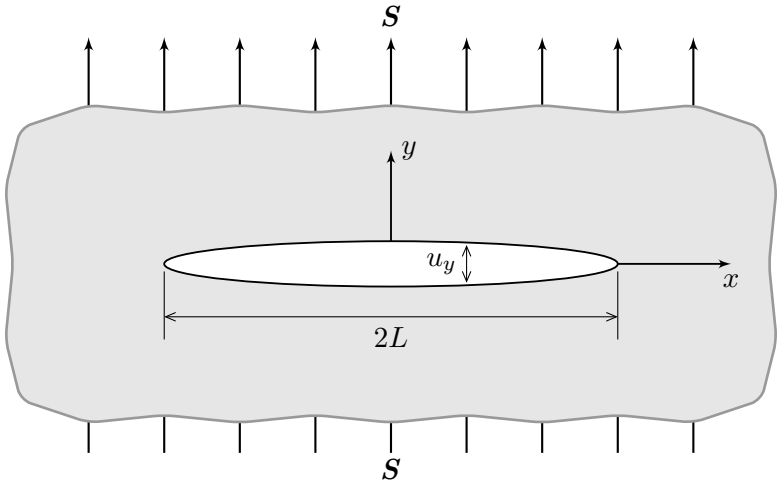

Figure 2.1: A plane crack under tensile field

the Flamant and Kelvin solutions in elasticity problem and Fourier transform [33–35] (see Appendix A for detail). The traction $\sigma_{yy}(x,0)$ due to the dislocation $u_y(\xi,0)$ is expressed by

$$\sigma_{yy} = -\frac{G u_y(\xi) d\xi}{2\pi(1-\nu)(x-\xi)} \tag{2.1}$$

The traction due to the whole distribution of dislocations can be written by a integral form:

$$\sigma_{yy} = -\frac{G}{2\pi(1-\nu)} \int_{-L}^{+L} \frac{u_y(\xi) d\xi}{(x-\xi)} \tag{2.2}$$

where

$$u_y(\xi) = -\frac{2S(1-\nu)}{G} \frac{\xi}{\sqrt{L^2-\xi^2}} \tag{2.3}$$

The complete stress field and crack opening displacement are given by

$$\sigma_{yy} = \frac{S|x|}{\sqrt{x^2-L^2}}, \qquad |x| > L, \quad y = 0 \tag{2.4}$$

$$u_y(x,0^+) - u_y(x,0^-) = \int_{-L}^{x} u_y(\xi) d\xi = \frac{2S(1-\nu)}{G} \sqrt{L^2-x^2} \tag{2.5}$$

2.2 Displacement discontinuity method (DDM)

2.2.1 Displacement discontinuity over a finite line segment

The displacement discontinuity boundary element method (DDBEM) is proposed by Crouch in 1976 [36,37]. Under plane strain conditions for the z direction, the $x-$ and $y-$components of displacement in a homogeneous, isotropic, linearly elastic body are given by [33]

$$u_x = B_x - \frac{1}{4(1-\nu)} \frac{\partial}{\partial x}(xB_x + yB_y + \beta) \tag{2.6a}$$

$$u_y = B_y - \frac{1}{4(1-\nu)} \frac{\partial}{\partial y}(xB_x + yB_y + \beta) \tag{2.6b}$$

where ν is Poisson's ratio and B_x, B_y and β are the Papkovitch functions, which in the absence of body forces satisfy Laplace's equation:

$$\nabla^2 B_x = 0, \quad \nabla^2 B_y = 0, \quad \nabla^2 \beta = 0 \tag{2.7}$$

with $\nabla^2 = \dfrac{\partial^2}{\partial x^2} + \dfrac{\partial^2}{\partial y^2}$. The two particular sets of Papkovitch functions are chosen, one is free from shear traction and the other is free from normal traction on the plane $y = 0$. These two sets of functions can be found by substituting Eq. (2.6) into the stress-strain relations for plane strain and choosing B_x, B_y and β satisfying $\sigma_{xy} = 0$ for shear traction free or $\sigma_{yy} = 0$ for normal traction free.

In case of shear traction free, the Papkovitch functions are taken as

$$B_x = 0 \tag{2.8a}$$

$$B_y = 4(1-\nu)\frac{\partial \phi}{\partial y} \tag{2.8b}$$

$$\beta = 4(1-\nu)(1-2\nu)\phi \tag{2.8c}$$

where $\nabla^2 \phi = 0$, the displacement and stresses can be expressed in terms of a single harmonic function ϕ as

$$u_x = -(1-2\nu)\frac{\partial \phi}{\partial x} - y\frac{\partial^2 \phi}{\partial x \partial y} \tag{2.9a}$$

$$u_y = 2(1-\nu)\frac{\partial \phi}{\partial y} - y\frac{\partial^2 \phi}{\partial y^2} \tag{2.9b}$$

and

$$\sigma_{xx} = 2G\left(\frac{\partial^2 \phi}{\partial y^2} + y\frac{\partial^3 \phi}{\partial y^3}\right) \tag{2.10a}$$

$$\sigma_{yy} = 2G\left(\frac{\partial^2 \phi}{\partial y^2} - y\frac{\partial^3 \phi}{\partial y^3}\right) \tag{2.10b}$$

$$\sigma_{xy} = -2Gy\frac{\partial^3 \phi}{\partial x \partial y^2} \tag{2.10c}$$

The expression for σ_{xy} shows that the shear stress vanishes on $y = 0$ because $\dfrac{\partial^3 \phi}{\partial x \partial y^2}$ is finite on $y = 0$.

For the case of a body free from normal traction, Papkovitch functions are given by

$$B_x = 0 \tag{2.11a}$$

$$B_y = 4(1-\nu)\frac{\partial \chi}{\partial x} \tag{2.11b}$$

$$\beta = 8(1-\nu)^2 \int \frac{\partial \chi}{\partial x} dy \tag{2.11c}$$

where $\nabla^2 \chi = 0$, the displacement and stresses in terms of χ are

$$u_x = 2(1-\nu)\frac{\partial \chi}{\partial y} + y\frac{\partial^2 \chi}{\partial y^2} \tag{2.12a}$$

$$u_y = (1-2\nu)\frac{\partial \chi}{\partial x} - y\frac{\partial^2 \chi}{\partial x \partial y} \tag{2.12b}$$

and

$$\sigma_{xx} = 2G\left(2\frac{\partial^2 \chi}{\partial x \partial y} + y\frac{\partial^3 \chi}{\partial x \partial y^2}\right) \tag{2.13a}$$

$$\sigma_{yy} = -2Gy\frac{\partial^3 \chi}{\partial x \partial y^2} \tag{2.13b}$$

$$\sigma_{xy} = 2G\left(\frac{\partial^2 \chi}{\partial y^2} + y\frac{\partial^3 \chi}{\partial y^3}\right) \tag{2.13c}$$

The expression for σ_{yy} shows that this stress component vanishes on $y = 0$ because $\dfrac{\partial^3 \chi}{\partial x \partial y^2}$ is finite on $y = 0$.

A constant displacement discontinuity over a finite line segment $-a \leq x \leq a$ on $y = 0$ can be solved in two parts, for a displacement discontinuity in the normal displacement u_y and for a discontinuity in the transverse displacement u_x.

The boundary conditions for a normal displacement discontinuity D_y are

$$\sigma_{xy}(x, 0) = 0, \qquad -\infty < x < \infty \tag{2.14a}$$

$$u_y(x,0) = 0, \qquad x < -a \text{ and } x > a \tag{2.14b}$$

$$\lim_{y\to 0^+} u_y(x,y) - \lim_{y\to 0^-} u_y(x,y) = D_y, \qquad -a < x < a \tag{2.14c}$$

The harmonic function ϕ which satisfy the boundary conditions Eq. (2.14) with Eq. (2.9) is found by

$$\phi(x,y) = \frac{D_y}{4\pi(1-\nu)} \left\{ y \arctan\frac{x+a}{y} - y\arctan\frac{x-a}{y} + (x+a)\ln\left[(x+a)^2+y^2\right]^{\frac{1}{2}} - (x-a)\ln\left[(x-a)^2+y^2\right]^{\frac{1}{2}} \right\} \tag{2.15}$$

Similarly, the harmonic function χ is given by

$$\chi(x,y) = \frac{D_x}{4\pi(1-\nu)} \left\{ y \arctan\frac{x+a}{y} - y\arctan\frac{x-a}{y} + (x+a)\ln\left[(x+a)^2+y^2\right]^{\frac{1}{2}} - (x-a)\ln\left[(x-a)^2+y^2\right]^{\frac{1}{2}} \right\} \tag{2.16}$$

2.2.2 Dislocation discontinuity in an infinite body

The displacement discontinuity D_i in Eq. (2.14) can be rewritten as

$$D_x = u_x(x,0^-) - u_x(x,0^+) \tag{2.17a}$$

$$D_y = u_y(x,0^-) - u_y(x,0^+) \tag{2.17b}$$

From Eq. (2.6) to Eq. (2.17), we obtain the displacements

$$u_x = D_x\left[2(1-\nu)\phi_{,y} - y\phi_{,xx}\right] + D_y\left[-(1-2\nu)\phi_{,x} - y\phi_{,xy}\right] \tag{2.18a}$$

$$u_y = D_x\left[(1-2\nu)\phi_{,x} - y\phi_{,xy}\right] + D_y\left[2(1-\nu)\phi_{,y} - y\phi_{,yy}\right] \tag{2.18b}$$

and stresses

$$\sigma_{xx} = 2GD_x\left(2\phi_{,xy} + y\phi_{,xyy}\right) + 2GD_y\left(\phi_{,yy} + y\phi_{,yyy}\right) \tag{2.19a}$$

$$\sigma_{yy} = 2GD_x\left(-y\phi_{,xyy}\right) + 2GD_y\left(\phi_{,yy} - y\phi_{,yyy}\right) \tag{2.19b}$$

$$\sigma_{xy} = 2GD_x\left(\phi_{,yy} + y\phi_{,yyy}\right) + 2GD_y\left(-y\phi_{,xyy}\right) \tag{2.19c}$$

The function f and its derivatives are

$$f(x,y) = -\frac{1}{4\pi(1-\nu)}\left\{y\left(\arctan\frac{y}{x-a} - \arctan\frac{y}{x+a}\right)\right.$$
$$\left. -(x-a)\ln[(x-a)^2] + y^2]^{\frac{1}{2}} + (x+a)\ln[(x+a)^2] + y^2]^{\frac{1}{2}}\right\} \tag{2.20a}$$

$$f_{,x} = \frac{1}{4\pi(1-\nu)}\left\{\ln[(x-a)^2] + y^2]^{\frac{1}{2}} - \ln[(x+a)^2] + y^2]^{\frac{1}{2}}\right\} \tag{2.20b}$$

$$f_{,y} = -\frac{1}{4\pi(1-\nu)}\left(\arctan\frac{y}{x-a} - \arctan\frac{y}{x+a}\right) \tag{2.20c}$$

$$f_{,xy} = \frac{1}{4\pi(1-\nu)}\left[\frac{y}{(x-a)^2+y^2} - \frac{y}{(x+a)^2+y^2}\right] \tag{2.20d}$$

$$f_{,xx} = -f_{,yy} = \frac{1}{4\pi(1-\nu)}\left[\frac{x-a}{(x-a)^2+y^2} - \frac{x+a}{(x+a)^2+y^2}\right] \tag{2.20e}$$

$$f_{,xyy} = -f_{,xxx} = \frac{1}{4\pi(1-\nu)}\left\{\frac{(x-a)^2-y^2}{[(x-a)^2+y^2]^2} - \frac{(x+a)^2-y^2}{[(x+a)^2+y^2]^2}\right\} \tag{2.20f}$$

$$f_{,yyy} = -f_{,xxy} = \frac{2y}{4\pi(1-\nu)}\left\{\frac{x-a}{[(x-a)^2+y^2]^2} - \frac{x+a}{[(x+a)^2+y^2]^2}\right\} \tag{2.20g}$$

The displacements on $y = 0$ are then defined by substituting Eq. (2.20) into Eq. (2.18),

$$u_x = -\frac{1}{2\pi}D_x\lim_{y\to 0^{\pm}}\left(\arctan\frac{y}{x-a} - \arctan\frac{y}{x+a}\right) - \frac{1-2\nu}{4\pi(1-\nu)}D_y\ln\left|\frac{x-a}{x+a}\right| \tag{2.21a}$$

$$u_y = \frac{1-2\nu}{4\pi(1-\nu)}D_x\ln\left|\frac{x-a}{x+a}\right| - \frac{1}{2\pi}D_y\lim_{y\to 0^{\pm}}\left(\arctan\frac{y}{x-a} - \arctan\frac{y}{x+a}\right) \tag{2.21b}$$

Due to the discontinuity of $\arctan\left(\frac{y}{x-a}\right)$ and $\arctan\left(\frac{y}{x+a}\right)$, we have

$$\lim_{y\to 0^{\pm}}\left(\arctan\frac{y}{x-a} - \arctan\frac{y}{x+a}\right) = \begin{cases} 0 & \text{for } |x| > a, \quad y = 0^{\pm} \\ \pi & \text{for } |x| < a, \quad y = 0^{+} \\ -\pi & \text{for } |x| < a, \quad y = 0^{-} \end{cases} \tag{2.22}$$

The Eq. (2.21) must be limited for three separate cases

for $|x| > a, y = 0^{\pm}$

$$u_x(x,0) = -\frac{1-2\nu}{4\pi(1-\nu)} D_y \ln\left|\frac{x-a}{x+a}\right| \tag{2.23a}$$

$$u_y(x,0) = \frac{1-2\nu}{4\pi(1-\nu)} D_x \ln\left|\frac{x-a}{x+a}\right| \tag{2.23b}$$

for $|x| < a, y = 0^{+}$

$$u_x(x,0^+) = -\frac{1}{2} D_x - \frac{1-2\nu}{4\pi(1-\nu)} D_y \ln\left|\frac{x-a}{x+a}\right| \tag{2.23c}$$

$$u_y(x,0^+) = \frac{1-2\nu}{4\pi(1-\nu)} D_x \ln\left|\frac{x-a}{x+a}\right| - \frac{1}{2} D_y \tag{2.23d}$$

for $|x| < a, y = 0^{+}$

$$u_x(x,0^-) = \frac{1}{2} D_x - \frac{1-2\nu}{4\pi(1-\nu)} D_y \ln\left|\frac{x-a}{x+a}\right| \tag{2.23e}$$

$$u_y(x,0^-) = \frac{1-2\nu}{4\pi(1-\nu)} D_x \ln\left|\frac{x-a}{x+a}\right| + \frac{1}{2} D_y \tag{2.23f}$$

The stress components on $y = 0$ are also obtained by substituting Eq. (2.20) into Eq. (2.19)

$$\sigma_{xx}(x,0) = -\frac{G}{\pi(1-\nu)} D_y \frac{a}{x^2-a^2} \tag{2.24a}$$

$$\sigma_{yy}(x,0) = -\frac{G}{\pi(1-\nu)} D_y \frac{a}{x^2-a^2} \tag{2.24b}$$

$$\sigma_{xy}(x,0) = -\frac{G}{\pi(1-\nu)} D_x \frac{a}{x^2-a^2} \tag{2.24c}$$

2.2.3 A plane crack under tensile

As shown in Fig. 2.1, a plane crack under tensile field problem can be defined by the following boundary conditions,

$$\begin{aligned} \sigma_{xy}(x,0) &= 0, && -\infty < x < \infty \\ \sigma_{yy}(x,0) &= -p, && |x| < L \\ D_y(x,0) &= 0. && |x| > L \end{aligned} \tag{2.25}$$

The normal stress σ_{yy} at a point $(x, 0)$ due to a constant displacement discontinuity D_y over the interval $|x| \leq a$, $y = 0$ is given by Eq. (2.24)

$$\sigma_{yy}(x, 0) = -\frac{G}{\pi\,(1-\nu)} D_y \frac{a}{x^2 - a^2}$$

For the numerical solution of the crack problem, we divide the crack into n line segments. If discontinuity presents on the line segment of length $2a_j$ centered at the point $x = x_i$, $y = 0$, then above equation can be written as

$$\sigma_{yy}(x, 0) = -\frac{G}{\pi\,(1-\nu)} D_{y,k} \frac{a_k}{(x - x_k)^2 - (a_k)^2} \tag{2.26}$$

where, $D_{y,k}$ is the displacement discontinuity over the interval $|x - x_k| \leq a_k$, $y = 0$.

The stress at the mid point of ith element due to a displacement discontinuity at the kth element can be obtained by setting $x = x_i$,

$$\sigma_{yy}(x_i, 0) = -\frac{G}{\pi\,(1-\nu)} D_{y,k} \frac{a_k}{(x_i - x_k)^2 - (a_k)^2} \tag{2.27}$$

The stress at the mid point of ith element due to a displacement discontinuity over the all elements can be expressed in a summation form,

$$\sigma_{yy}(x_i, 0) = \sigma_{yy,i} = \sum_{k=1}^{N} A_{ik} D_{y,k} \tag{2.28}$$

where, the influence coefficient A_{ik} are

$$A_{ik} = -\frac{G}{\pi(1-\nu)} \frac{a_k}{(x_i - x_k)^2 - (a_k)^2} \tag{2.29}$$

By applying boundary condition Eq. (2.25) to Eq. (2.28), we get

$$\sigma_{yy,i} = -p = \sum_{k=1}^{N} A_{ik} D_{y,k} \tag{2.30}$$

The displacement discontinuity D_y can be obtained by solving the system of N liner equations of Eq. (2.30).

2.3 Stress intensity factor

Stress and displacement field near crack tip

The stresses in the cracked body subjected to external forces is given by [38]

$$\sigma_{ij} = \left(\frac{k}{\sqrt{r}}\right) f_{ij}(\theta) + \sum_{m=0}^{\infty} A_m r^{\frac{m}{2}} g_{ij}^{(m)}(\theta) \tag{2.31}$$

where, σ_{ij}, k and f_{ij} are stress tensor, stress intensity factor defined by $k = K/\sqrt{2\pi}$ and dimensionless function of θ in the leading term, respectively.

For the higher-order terms, A_m and g_m are the amplitude and a dimensionless function of θ for the mth term. The higher order terms depend on geometry. Since the first term is proportional to $1/\sqrt{r}$, the first term approaches to infinity while the other terms remain finite or approach to zero. Therefore, stress near crack tip varies with $1/\sqrt{r}$ and near tip displacement varies with $\sqrt{r}$.

The near crack tip stress field for mode I in a linear elastic, isotropic material is given by

$$\sigma_{xx} = \frac{K_I}{\sqrt{2\pi r}} \cos\left(\frac{\theta}{2}\right)\left[1 - \sin\left(\frac{\theta}{2}\right)\sin\left(\frac{3\theta}{2}\right)\right] \tag{2.32a}$$

$$\sigma_{yy} = \frac{K_I}{\sqrt{2\pi r}} \cos\left(\frac{\theta}{2}\right)\left[1 + \sin\left(\frac{\theta}{2}\right)\sin\left(\frac{3\theta}{2}\right)\right] \tag{2.32b}$$

$$\sigma_{xy} = \frac{K_I}{\sqrt{2\pi r}} \cos\left(\frac{\theta}{2}\right)\sin\left(\frac{\theta}{2}\right)\cos\left(\frac{3\theta}{2}\right) \tag{2.32c}$$

and displacement field for mode I is

$$u_x = \frac{K_I}{2G}\sqrt{\frac{r}{2\pi}} \cos\left(\frac{\theta}{2}\right)\left[\kappa - 1 + 2\cos^2\left(\frac{\theta}{2}\right)\right] \tag{2.33a}$$

$$u_y = \frac{K_I}{2G}\sqrt{\frac{r}{2\pi}} \sin\left(\frac{\theta}{2}\right)\left[\kappa + 1 - 2\cos^2\left(\frac{\theta}{2}\right)\right] \tag{2.33b}$$

The Mode II near tip stress and displacement fields are as follows

$$\sigma_{xx} = -\frac{K_{II}}{\sqrt{2\pi r}} \sin\left(\frac{\theta}{2}\right)\left[2 + \cos\left(\frac{\theta}{2}\right)\cos\left(\frac{3\theta}{2}\right)\right] \tag{2.34a}$$

$$\sigma_{yy} = \frac{K_{II}}{\sqrt{2\pi r}} \sin\left(\frac{\theta}{2}\right) \cos\left(\frac{\theta}{2}\right) \cos\left(\frac{3\theta}{2}\right) \tag{2.34b}$$

$$\sigma_{xy} = \frac{K_{II}}{\sqrt{2\pi r}} \cos\left(\frac{\theta}{2}\right) \left[1 - \sin\left(\frac{\theta}{2}\right) \sin\left(\frac{3\theta}{2}\right)\right] \tag{2.34c}$$

and

$$u_x = \frac{K_{II}}{2G} \sqrt{\frac{r}{2\pi}} \sin\left(\frac{\theta}{2}\right) \left[\kappa + 1 + 2\cos^2\left(\frac{\theta}{2}\right)\right] \tag{2.35a}$$

$$u_y = -\frac{K_{II}}{2G} \sqrt{\frac{r}{2\pi}} \cos\left(\frac{\theta}{2}\right) \left[\kappa - 1 - 2\sin^2\left(\frac{\theta}{2}\right)\right] \tag{2.35b}$$

Stress or displacement matching

When displacement or stress near crack tip are known, the stress intensity factor can be obtained by matching the the displacement or stress with Eq. (2.32) to Eq. (2.35).

$$K_I = \lim_{r \to 0} \left[\sigma_{yy} \sqrt{2\pi r}\right] \qquad (\theta = 0) \tag{2.36}$$

$$K_I = \lim_{r \to 0} \left[\frac{G u_y}{2\,(1-\nu)} \sqrt{\frac{2\pi}{r}}\right] \qquad (\theta = \pi) \tag{2.37}$$

Energy release rate

Energy release rate and stress intensity factor for a mode I crack in a linear elastic solid is given by [39]

$$G_I = \frac{1-\nu}{2G} K_I^2 \tag{2.38}$$

Energy release rate for a crack can also calculated by evaluating the path-independent line integral for any contour that starts on one crack face and ends on the other:

$$G_i = \int_\Gamma \left(W \delta_{i1} - \sigma_{ij} \frac{\partial u_i}{\partial x_1}\right) m_j ds \tag{2.39}$$

where W, σ_{ij}, u_i and m_i are strain energy density given by $W = \sigma_{ij}\epsilon_{ij}/2$, stress tensor, displacement vector and a unit vector normal to Γ, respectively. The mode I stress intensity factor is then be obtained by comparison Eq. (2.38) with Eq. (2.39).

Strain energy

Relationship between strain energy and the mode I stress intensity factor is given by [40–42]

$$\frac{\partial W}{\partial b} = \frac{1-\nu}{G} K_I^2 \tag{2.40}$$

Strain energy for the pressurized crack problem can be obtained by calculating the work done by crack opening displacement.

$$W = -\frac{1}{2} p \int_{-a}^{a} \hat{u}_y(x) dx \doteq -p \sum_{j=1}^{N} a^j D_y^j \tag{2.41}$$

or by numerical estimation for slightly different crack length

$$\frac{\partial W}{\partial b} \doteq \frac{1}{2\Delta b} \left[W(b + \Delta b) - W(b - \Delta b) \right] \tag{2.42}$$

2.4 Use of special crack-tip element

As mentioned in Section 2.3, The analytical solution of the pressurized crack problem shows that the stresses at a distance r from the crack tip always vary as $r^{-1/2}$ if r is small. The example of a plane crack corresponds to mode I and for a crack length $2L$ subjected to internal pressure p , the mode I stress intensity factor can be defined by Eq. (A.36) and Eq. (2.36).

$$K_I = \lim_{x \to L^+} \sigma_{yy}(x) \sqrt{2\pi(x - L)} \tag{2.43a}$$

$$= \lim_{x \to L^+} \frac{px\sqrt{2\pi(x - L)}}{\sqrt{x^2 - L^2}} \tag{2.43b}$$

$$= p\sqrt{\pi L} \tag{2.43c}$$

But in more complex situation, the stress intensity factor need be evaluated numerically hence the requirement in fracture mechanics for accuracy close to the crack tip. The $r^{-1/2}$ variation of the stresses near the tip is from the relative displacement between the crack surfaces proportional to $x^{1/2}$ close to the tip. The special crack tip element $\bar{d}_y$, the relative normal displacement between the crack surfaces, is given by [37]

$$\bar{d}_y = D_y(x/a)^{1/2} \tag{2.44}$$

where $2a$ is the length of the crack tip element and D_y is the displacement discontinuity at the center of this element. From Eq. (2.24), the normal stress σ_{yy} at a point $(x, 0)$ due to a constant displacement discontinuity D_y over the interval $|x| \leq a$, $y = 0$ is given by,

$$\sigma_{yy}(x, 0) = -\frac{G}{\pi\,(1-\nu)} D_y \frac{a}{x^2 - a^2} \tag{2.45}$$

The above equation is derived by substituting $\bar{d}_y(\xi) = D_y$, in the integral,

$$\sigma_{yy}(x, 0) = -\frac{G}{2\pi(1-\nu)} \lim_{y \to 0} \int_{-a}^{a} \bar{d}_y(\xi) \frac{1}{(x-\xi)^2 + y^2} d\xi \tag{2.46}$$

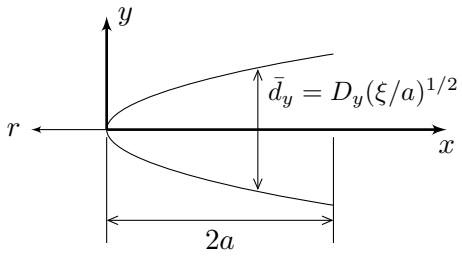

Figure 2.2: A special crack tip element

For the crack tip element, we have $\bar{d}_y(\xi) = D_y(\xi/a)^{1/2}$ in $0 \le \xi \le 2a$ and the above equation can be written as

$$\sigma_{yy}(x,0) = -\frac{GD_y}{2\pi(1-\nu)} \lim_{y\to 0} \int_0^{2a} (\xi/a)^{1/2} \frac{1}{(x-\xi)^2+y^2} d\xi \tag{2.47}$$

Upon evaluation of the integral, we have

$$\sigma_{yy}(x,0) = -\frac{GD_y}{2\pi(1-\nu)} \left(\frac{\sqrt{2}}{x-2a} + \frac{1}{2\sqrt{ax}} \ln \left| \frac{\sqrt{x}-\sqrt{2a}}{\sqrt{x}+\sqrt{2a}} \right| \right) \qquad (\text{for } x > 0) \tag{2.48a}$$

$$\sigma_{yy}(x,0) = -\frac{GD_y}{2\pi(1-\nu)} \frac{1}{\sqrt{ar}} \left(\arctan\sqrt{2a/r} - \frac{\sqrt{2a/r}}{r+2a} \right) \qquad (\text{for } x < 0) \tag{2.48b}$$

Similar expression can be derived for the special crack tip element on the right-hand end of the crack. The numerical solution can be obtained by dividing the crack into N elements such that element i of length $2a_i$ is center at the point $x = x_i$, $y = 0$. If the first and the last elements are the crack tip elements, the boundary influence coefficients Eq. (2.29) becomes

$$A_{ij} = -\frac{G}{\pi(1-\nu)} \frac{a_j}{(x_i-x_j)^2-(a_j)^2} \qquad \text{for } 2 \le j \le N-1 \tag{2.49a}$$

$$A_{ij} = -\frac{G}{2\pi(1-\nu)} \left[\frac{\sqrt{2}}{S-2a_j} + \frac{1}{2\sqrt{a_j S}} \ln \left| \frac{\sqrt{S}-\sqrt{2a_j}}{\sqrt{S}+\sqrt{2a_j}} \right| \right] \qquad \text{for } j = 1,\ j = N \tag{2.49b}$$

where $S = a_j + |\bar{x}_i - x_j|$

Then, a numerical solution to the pressurized crack problem can be obtained by solving the N simultaneous equations of Eq. (2.30).

More accurate results can be obtained by assuming a more complex form for $\hat{u}_y$ in the vicinity of the crack tip, such as $\bar{u}_d(\xi) = c_0\xi^{1/2} + c_1\xi^{3/2}$ over the first two elements. The constants c_0 and c_1 are related to the displacement discontinuities $D_{y,1}$ and $D_{y,2}$ at the mid-point of these elements and the corresponding boundary influence elements can be derived by following similar procedure to Eq. (2.49). Even more accuracy can also be achieved by

adding a term in $\xi^{5/2}$ to $\bar{d}_y$.

Fig. 2.3 shows displacement discontinuities of the right wing of a plane crack under tensile. The displacement discontinuities of ordinary and crack tip element are obtained from Eq. (2.30) with Eq. (2.29) and Eq. (2.49) and analytical solution is given by Eq. (2.4). From Fig. 2.1, the parameters are set to $G = 1.0$GPa, $\nu = 0.2$, $p = -1.0$MPa and 10 elements are used. As shown in Fig. 2.4, use of a special crack tip element provides better estimation of displacement discontinuity specially at the crack. Additionally, Table 2.1 shows that crack tip element also allow us to obtain more accurate stress intensity factor in followed crack propagation analysis.

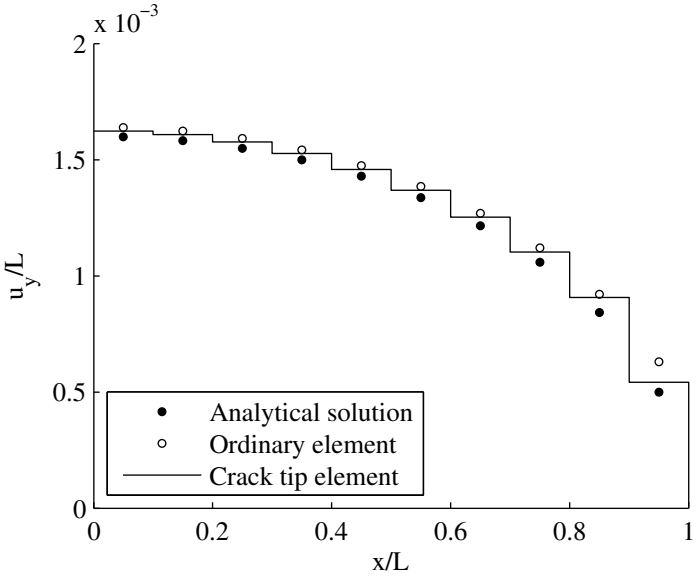

Figure 2.3: Comparison of displacement discontinuity

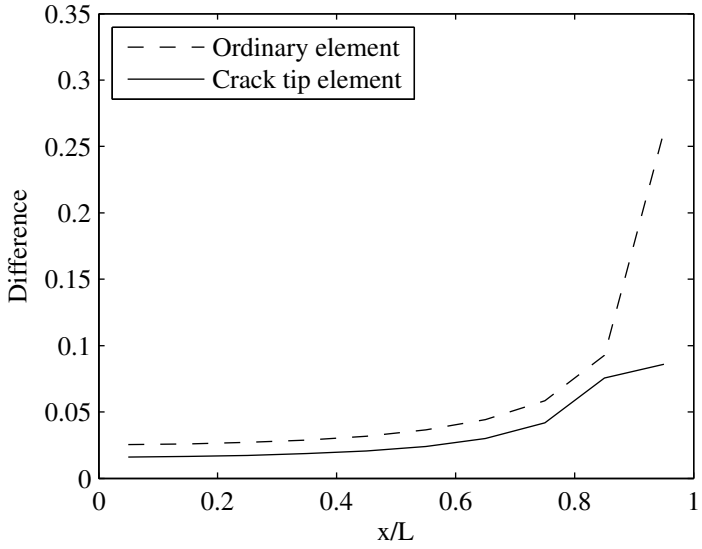

Figure 2.4: Difference in displacement

Method	**Analytical**	**Ordinary element**	**Crack tip element**
Displacement matching	1.77	2.21 (24.8%)	1.90 (7.3%)
Strain energy		1.82 (2.8%)	1.80 (1.7%)

Table 2.1: Comparison of Mode I stress intensity factor (MPa$\sqrt{\text{m}}$)

Chapter 3

Propagation of crack driven by internal fracturing fluid flows

3.1 Dynamics of a fracturing fluid flow inside crack

3.1.1 Newtonian fluids

The governing equations of fluid flow are continuity, equation of motion and constitutive equation. The continuity equation can be described that the system mass remain constant as the system moves through the flow field, given by

$$\frac{DM_{sys}}{Dt} = 0 \tag{3.1}$$

where $\frac{D}{Dt}$ and M_{sys} are material derivative or substantial derivative of system mass given by

$$\frac{D}{Dt} = \frac{\partial}{\partial t} + u\frac{\partial}{\partial x} + v\frac{\partial}{\partial y} + w\frac{\partial}{\partial z} \tag{3.2a}$$

$$M_{sys} = \int_{sys} \rho dV \tag{3.2b}$$

The equation of motion is given by

$$\sigma_{ij,j} + \rho b_i = \rho \dot{u}_i \qquad \text{or} \qquad \sigma_{ij,j} + \rho b_i = \rho \left(\frac{\partial u_i}{\partial t} + u_j \frac{\partial u_i}{\partial x_j} \right) \tag{3.3}$$

where ρb_i is the distributed body forces and $\dot{u}_i$ is the material derivative of u_i given by

$$\dot{u}_i = \frac{\partial u_i}{\partial t} + u_j u_{i,j} \tag{3.4}$$

The constitutive equation is

$$\sigma_{ij} = -p\delta_{ij} + \mu e_{ij} \tag{3.5}$$

where μ is viscosity coefficients, and e_{ij} is the rate of deformation tensor

$$e_{ij} = \frac{1}{2}(u_{i,j} + u_{j,i}) \tag{3.6}$$

Using Reynolds transport theorem for a system and a fixed, non-deforming control volume, Eq. (3.2) can be written as

$$\frac{D}{Dt} \int_{sys} \rho dV = \frac{\partial}{\partial t} \int_{cv} \rho dV + \int_{cs} \rho \mathbf{V} \cdot \hat{\mathbf{n}} dA = 0 \tag{3.7}$$

then,

$$\frac{\partial}{\partial t} \int_{cv} \rho dV = - \int_{cs} \rho \mathbf{V} \cdot \hat{\mathbf{n}} dA \tag{3.8}$$

by integrating above equation, we obtain the continuity equation

$$\frac{\partial w}{\partial t} = q_I - q_L - \frac{\partial q_x}{\partial x} - \frac{\partial q_y}{\partial y} \tag{3.9}$$

For one-dimensional fluid flow, above equation becomes

$$\frac{\partial w}{\partial t} = -\frac{\partial q_x}{\partial x} + q_I - q_L \tag{3.10}$$

where w, q and q_L are wall thickness, volume flow rate per unit length and fluid loss, respectively. From Navier-Stokes equation for Newtonian fluid,

$$\frac{\partial u_i}{\partial t} + u_j u_{i,j} = b_i - \frac{1}{\rho} p_{,i} + \nu u_{i,jj} \tag{3.11}$$

The components of Navier-stokes equation can be described by follow, first term: local acceleration of the fluid particle, second term: convective acceleration of the fluid particle, third term: body force or acceleration due to gravity, fourth term: pressure acceleration due to the pumping action of flow, last term: viscous deceleration due to the fluid's frictional resistance to objects moving through it. Therefore, if we assume the fluid is steady ($\partial u_i/\partial t = 0$) and has no body force or gravitational force is applied ($b_i = 0$), the first and third terms are dropped. Then, if the fluid is incompressible ($u_{i,i} = 0$)and u is not varies in the y and z direction, the second term can also be neglected. Thus Navier-Stokes equation reduces to

$$p_{,i} = \mu u_{i,jj} \quad \text{or} \quad \frac{\partial p}{\partial x} = \mu \frac{\partial^2 u}{\partial y^2} \tag{3.12}$$

by integrating above equation for u with boundary conditions $u = 0$ for $y = \pm w/2$,

$$u = \frac{1}{2\mu} \left(\frac{\partial p}{\partial x} \right) \left[y^2 - \left(\frac{w}{2} \right)^2 \right] \tag{3.13}$$

The volume rate of flow q passing between the plates, can be obtained by integrating the velocity field over the height of plates,

$$q_x = \int_{-w/2}^{w/2} u dy = -\frac{w^3}{12\mu} \left(\frac{\partial p}{\partial x} \right) \quad \text{or} \quad \frac{\partial p}{\partial x} + \frac{12\mu}{w^3} q_x = 0 \tag{3.14}$$

Shear stress at the walls can be obtained from,

$$\int_{-w/2}^{w/2} \frac{\partial \tau_{xy}}{\partial y} dy = w \frac{\partial p}{\partial x} = -\mu \frac{12}{w^2} q_x \tag{3.15}$$

3.1.2 Power-law fluids (non-Newtonian)

Power-law fluid is also called a generalized Newtonian fluid defined by

$$\tau = K' \left(\frac{\partial u}{\partial y} \right)^{n'} \tag{3.16}$$

where τ, $\partial u/\partial y$, K' and n' are shear stress, velocity gradient, flow consistency index and flow behavior index, respectively. The flow behavior index n' is given by $n' = 1$ for Newtonian, $n' < 1$ for Pseudo-plastic, $n' > 1$ for Dilatant fluid. We assume the power-law fluid discussed in following chapters is non-Newtonian fluid having fluid behavior index of $n' < 1$. Flow analysis for one-dimensional power-law fluid flow between parallel plates can be found in [19, 20, 43]. When the velocity profile for power-law fluid is given by,

$$u_x = \left(\frac{2n'+1}{n'+1} \right) \frac{2(1+\frac{1}{n'})}{w^{\frac{1}{n'}+2}} q_x \left[\left(\frac{w^{\frac{1}{n'}+1}}{2} - y^{\frac{1}{n'}+1} \right) \right] \tag{3.17}$$

where

$$q_x = \int_{-w/2}^{w/2} u_x dy \tag{3.18}$$

The shear stress at wall can be determined by

$$\int_{-w/2}^{w/2} \frac{\partial \tau_{xy}}{\partial y} = w\partial \frac{\partial p}{\partial x} = -\eta' \left(\frac{q_x}{w^2} \right)^{2n+1} \tag{3.19}$$

where η' is a viscosity parameter of power-law fluid

By integration of Eq. (3.3) with Eq. (3.17) and Eq. (3.19), we obtain the pressure gradient equation

$$\frac{\partial p}{\partial x} + \eta' \left(\frac{|q|}{w^2} \right)^{n'-1} \frac{q_x}{w^3} = 0 \tag{3.20a}$$

$$\frac{\partial p}{\partial y} + \eta' \left(\frac{|q|}{w^2} \right)^{n'-1} \frac{q_y}{w^3} = \rho F_y \tag{3.20b}$$

and continuity equation is from Eq. (3.9)

$$\frac{\partial q_x}{\partial x} + \frac{\partial q_y}{\partial y} = -\frac{\partial w}{\partial t} + q_I - q_L \tag{3.21}$$

where q_x are q_y volume flow rate in x and y direction per unit length. $|q|$ is resultant flow rate given by $|q| = \left(q_x^2 + q_y^2\right)^{1/2}$. q_L is volume leak-off rate per unit fracture area.

The viscosity parameter η' is related to the usual power-law coefficients K' and n' and it is given by

$$\eta' = 2^{(n'+1)} K' (2 + 1/n')^{n'} \tag{3.22}$$

By limiting to one-dimensional flow with constant fluid injection without leak-off, above equations become

$$\frac{\partial w}{\partial t} = -\frac{\partial q_x}{\partial x} + q_I \tag{3.23}$$

$$q_x = -\frac{n'}{2 + 4n'} \left(\frac{w^{2n'+1}}{2K'} \frac{\partial p}{\partial x} \right)^{\frac{1}{n'}} \tag{3.24}$$

$$\int_{-w/2}^{w/2} \frac{\partial \tau_{xy}}{\partial y} dy = -\eta' \left(\frac{q_x}{w^2} \right)^{n'} \tag{3.25}$$

where q_I is volume injection rate per unit fracture area and it is applied to regions near the wellbore and adjacent to perforations only

3.2 Numerical solutions of solid-fluid coupled field problem

3.2.1 Solid-fluid interaction

Consider a plane crack under in-situ stress σ_{xx} and σ_{yy} while fracturing fluid is injected at the center of crack to open and provide sufficient pressure for propagation as shown in Fig. 3.1. The fluid pressure p_f inside crack generated by constant fluid injection q_I at

wellbore produces opening displacement of crack surface through the length. When the mode I stress intensity factor K_I at crack tip reaches the mode I critical stress intensity factor K_{Ic} or crack tip opening displacement w_{tip} meets critical opening displacement w_{cr}, the crack starts growing to x direction. From Eq. (3.23), the wall width is related to volume flow rate q_x and pressure gradient $\partial p/\partial x$. we can assume the pressure field caused by internal fluid flow as tractions applied to the crack surface. Therefore, solid-fluid coupled field problem can be solved by coupling the pressure gradient equation in Eq. (3.20) with the stress created by displacement discontinuities on crack surface in Eq. (2.28). Recall

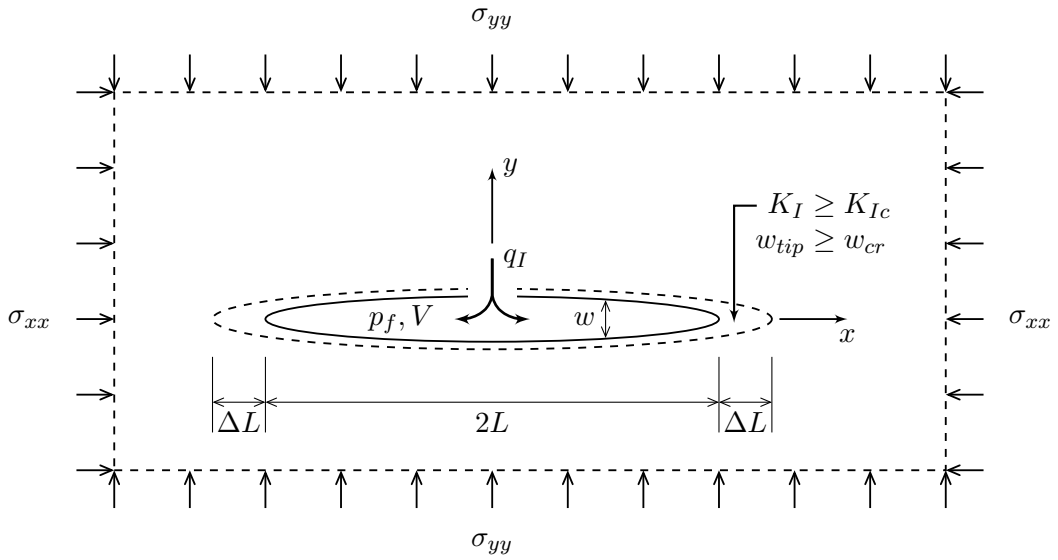

Figure 3.1: Propagation of a plane crack caused by internal fluid flow

the equations for fluid flow analysis and the displacement discontinuity solution for a plane crack under tensile, we can have the solid-fluid coupled solution,

$$\frac{\partial w}{\partial t} = -\frac{\partial q_x}{\partial x} + q_I \tag{3.26}$$

$$q_x = -\frac{n'}{2+4n'}\left(\frac{w^{2n'+1}}{2K'}\frac{\partial p}{\partial x}\right)^{\frac{1}{n'}} \tag{3.27}$$

and discretized form of displacement discontinuity solution is

$$p_i = \sum_{j=1}^{N} A_{ij} w_j = p_f - \sigma_{\text{situ}} \tag{3.28}$$

where

$$A_{ij} = -\frac{G}{\pi(1-\nu)} \frac{a_j}{(x_i - x_j)^2 - (a_j)^2} \qquad \text{for } 2 \le j \le N-1$$

$$A_{ij} = -\frac{G}{2\pi(1-\nu)} \left[\frac{\sqrt{2}}{S - 2a_j} + \frac{1}{2\sqrt{a_j S}} \ln \left| \frac{\sqrt{S} - \sqrt{2a_j}}{\sqrt{S} + \sqrt{2a_j}} \right| \right] \qquad \text{for } j = 1,\ j = N$$

The boundary, initial conditions and constraint are

$$q(0^+, t) = \frac{q_I}{2} = \text{constant} \tag{3.29a}$$

$$q(0^-, t) = -\frac{q_I}{2} = \text{constant} \tag{3.29b}$$

$$q(L, t) = 0 \tag{3.29c}$$

$$w(x, t) = 0, \quad \text{for } |x| \ge L(t) \tag{3.29d}$$

$$\frac{\partial w(0, t)}{\partial x} = 0 \tag{3.29e}$$

$$w(x, 0) = 0 \tag{3.29f}$$

$$\int_{-L}^{L} w \ \text{dx} = \int_{0}^{t} q \ \text{dt} \tag{3.29g}$$

The first two conditions are for fluid injection at well bore and q_i remains constant. The third and fourth describe there is no displacement or fluid flow beyond the crack tip. The fifth means the system is symmetry along the y axis and the last term constrains the fractured volume of the crack must be same as injected volume for given time.

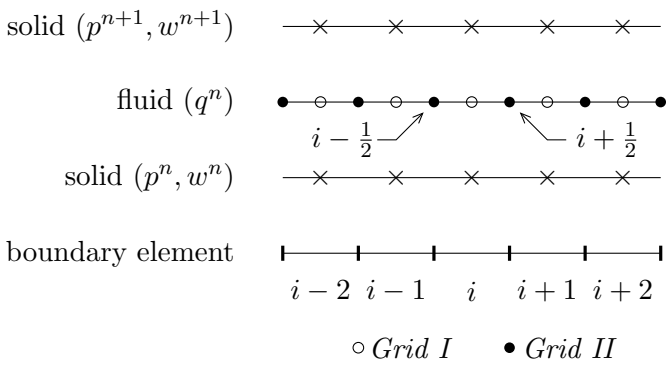

Figure 3.2: Grid systems for finite difference discretization

3.2.2 Grid systems

Two grid systems for fluid flow equations are provided as shown in Section 3.2.2. The node locations of q_i in *Grid I* are same as those of boundary element in displacement discontinuity solution which the nodes are located at the center of element. On the other hand, in *Grid II*, the q_i are located at the edge of boundary elements. The *Grid I* is comparatively easy to be coupled with displacement discontinuity solution but requires ghost elements outside crack. In *Grid II*, because q_i is located at the edge of boundary element, the exact boundary conditions can be applied. Due to the symmetry of the crack along the y -axis, only the right hand side of crack is modeled for efficiency.

3.2.3 Explicit solutions

The equations for fluid flow inside crack Eq. (3.26) and Eq. (3.27) are discretized with explicit finite difference scheme. An explicit forward difference scheme is used in time for both grid systems and a central difference in space for *Grid I* and a forward difference for *Grid II* are applied as shown in Fig. 3.3.

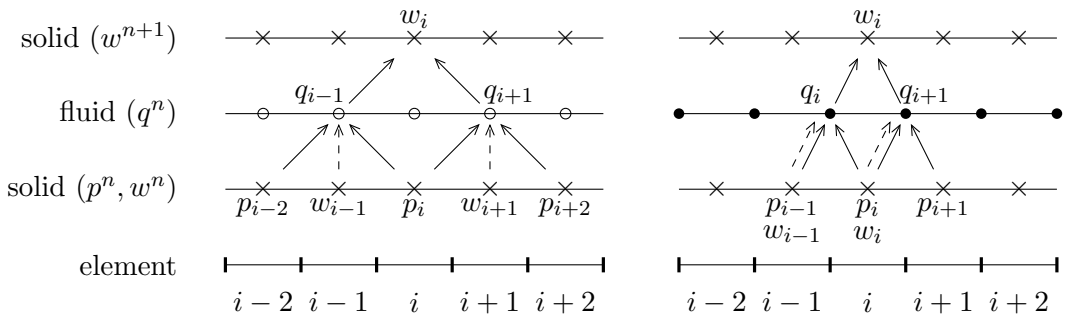

(a) *Grid I* (b) *Grid II*

Figure 3.3: Explicit finite difference schemes

For *Grid I*

The continuity equation Eq. (3.26) in *Grid I* can be discretized by

$$w_i^{m+1} = w_i^m - \frac{\Delta t}{2\Delta x}\left(q_{i+1}^m - q_{i-1}^m\right), \quad \text{for } 2 \le i \le n-1 \tag{3.30a}$$

$$w_1^{m+1} = w_1^m - \frac{\Delta t}{2\Delta x}\left(q_2^m + \bar{q}_1^m\right) + w_{\text{inj}} \tag{3.30b}$$

$$w_n^{m+1} = w_n^m + \frac{\Delta t}{2\Delta x}\left(q_{n-1}^m\right) \tag{3.30c}$$

and the pressure gradient equation Eq. (3.27) is

$$q_i^m = -\frac{n'}{2+4n'}\left[\frac{(w_i^m)^{2n'+1}}{2K'}\left(\frac{p_{i+1}^m - p_{i-1}^m}{2\Delta x}\right)\right]^{\frac{1}{n'}}, \quad \text{for } 2 \le i \le n-1 \tag{3.31a}$$

$$q_1^m = -\frac{n'}{2+4n'}\left[\frac{(w_1^m)^{2n'+1}}{2K'}\left(\frac{p_2^m - \bar{p}_1^m}{2\Delta x}\right)\right]^{\frac{1}{n'}} \tag{3.31b}$$

$$q_n^m = -\frac{n'}{2+4n'}\left[\frac{(w_n^m)^{2n'+1}}{2K'}\left(\frac{\bar{p}_n^m - p_{n-1}^m}{2\Delta x}\right)\right]^{\frac{1}{n'}} \tag{3.31c}$$

where w_{inj} is the created volume at the near well bore element by fluid injection given by $w_{\text{inj}} = \dfrac{\Delta t}{\Delta x}\dfrac{q_I}{2}$, $\bar{q}$ and $\bar{p}$ are volume flow rate and pressure of the ghost elements located

at beyond well bore and crack tip element. By combining above equations we obtain the explicit finite difference solution

$$w_i^{m+1} = w_i^m + \lambda_I \left\{ \left[\left(w_{i+1}^m\right)^{2n'+1} \left(p_{i+2}^m - p_i^m\right) \right]^{\frac{1}{n'}} - \left[\left(w_{i-1}^m\right)^{2n'+1} \left(p_i^m - p_{i-2}^m\right) \right]^{\frac{1}{n'}} \right\},$$

$$\text{for } 3 \le i \le n-2 \tag{3.32a}$$

$$w_1^{m+1} = w_1^m + \lambda_I \left\{ \left[(w_2^m)^{2n'+1} \left(p_3^m - p_1^m\right) \right]^{\frac{1}{n'}} + \left[(w_1^m)^{2n'+1} \left(p_2^m - p_1^m\right) \right]^{\frac{1}{n'}} \right\} + w_{\text{inj}} \tag{3.32b}$$

$$w_2^{m+1} = w_2^m + \lambda_I \left\{ \left[(w_3^m)^{2n'+1} \left(p_4^m - p_2^m\right) \right]^{\frac{1}{n'}} - \left[(w_1^m)^{2n'+1} \left(p_2^m - p_1^m\right) \right]^{\frac{1}{n'}} \right\} \tag{3.32c}$$

$$w_{n-1}^{m+1} = w_{n-1}^m + \lambda_I \left\{ \left[(w_n^m)^{2n'+1} \left(p_n^m - p_{n-1}^m\right) \right]^{\frac{1}{n'}} - \left[\left(w_{n-2}^m\right)^{2n'+1} \left(p_{n-1}^m - p_{n-3}^m\right) \right]^{\frac{1}{n'}} \right\}$$

(3.32d)

$$w_n^{m+1} = w_n^m - \lambda_I \left[\left(w_{n-1}^m\right)^{2n'+1} \left(p_n^m - p_{n-2}^m\right) \right]^{\frac{1}{n'}} \tag{3.32e}$$

where $\lambda_I = \dfrac{n'\Delta t}{2\Delta x(2+4n')(4K'\Delta x)^{\frac{1}{n'}}}$.

For *Grid II*

The discretized continuity and pressure gradient equations of Eq. (3.26) and Eq. (3.27) in *Grid II* system are given by

$$w_i^{m+1} = w_i^m - \frac{\Delta t}{\Delta x}\left(q_{i+1}^m - q_i^m\right), \quad \text{for } 2 \le i \le n-1 \tag{3.33a}$$

$$w_1^{m+1} = w_1^m - \frac{\Delta t}{\Delta x}\left(q_2^m - q_{\text{inj}}\right) \tag{3.33b}$$

$$w_n^{m+1} = w_n^m + \frac{\Delta t}{\Delta x} q_n^m \tag{3.33c}$$

and

$$q_i^m = -\frac{n'}{2+4n'}\left[\frac{\left(w_{i-1}^m\right)^{2n'+1}}{2K'}\left(\frac{p_i^m - p_{i-1}^m}{\Delta x}\right)\right]^{\frac{1}{n'}}, \quad \text{for } 2 \le i \le n \tag{3.34}$$

Then we obtain explicit finite difference solution

$$w_i^{m+1} = w_i^m + \lambda_{II} \left\{ \left[(w_i^m)^{2n'+1} \left(p_{i+1}^m - p_i^m \right) \right]^{\frac{1}{n'}} - \left[\left(w_{i-1}^m \right)^{2n'+1} \left(p_i^m - p_{i-1}^m \right) \right]^{\frac{1}{n'}} \right\}$$

$$\text{for } 2 \le i \le n-1 \tag{3.35a}$$

$$w_1^{m+1} = w_1^m + \lambda_{II} \left[(w_1^m)^{2n'+1} \left(p_2^m - p_1^m \right) \right]^{\frac{1}{n'}} + w_{\text{inj}} \tag{3.35b}$$

$$w_n^{m+1} = w_n^m - \lambda_{II} \left[\left(w_{n-1}^m \right)^{2n'+1} \left(p_n^m - p_{n-1}^m \right) \right]^{\frac{1}{n'}} \tag{3.35c}$$

where $w_{\text{inj}} = \dfrac{\Delta t}{\Delta x} \dfrac{q_I}{2}$ and $\lambda_{II} = \dfrac{n' \Delta t}{\Delta x (2+4n') (2K' \Delta x)^{\frac{1}{n'}}}$.

3.2.4 Courant-Friedrichs-Lewy Condition (CFL Condition)

Recall the discrete forms of fluid flow equations of Eq. (3.26) for Newtonian fluid ($n' = 1$) and elasticity equation Eq. (3.28) [26, 44].

$$\frac{w_i^{m+1} - w_i^m}{\Delta t} = \frac{w^3}{12\mu} \frac{1}{\Delta x^2} \left(p_{i+1}^m - 2p_i^m + p_{i-1}^m \right)$$

$$p_i = \sum_{k=1}^{N} A_{ik} w_k$$

$$A_{ik} = -\frac{G}{\pi(1-\nu)} \frac{a_k}{(x_i - x_k)^2 - (a_k)^2}$$

The operators of the equations can be written by

$$A_{mn} = -\frac{G}{\pi(1-\nu)} \frac{a_n}{(x_m - x_n)^2 - (a_n)^2} = \frac{G}{2\pi \Delta x (1-\nu)} \left[\frac{1}{(m-n)^2 - \frac{1}{4}} \right] \tag{3.36}$$

$$Cp_n = \frac{\bar{w}^3}{12\mu} \frac{1}{\Delta x^2} \left(p_{n+1} - 2p_n + p_{n-1} \right) \tag{3.37}$$

The eigenvalues of the operators are

$$\hat{A}_k = -\frac{G}{2\pi \Delta x (1-\nu)} \sum_{k=-\infty}^{\infty} \frac{\mathrm{e}^{ikm\Delta x}}{m^2 - \frac{1}{4}} = -\frac{G}{2\pi \Delta x (1-\nu)} \left[-2\pi \sin \left(\frac{|k| \Delta x}{2} \right) \right] \tag{3.38}$$

$$\hat{C}_k = -\frac{\bar{w}^3}{3\mu} \frac{1}{\Delta x^2} \sin^2 \left(\frac{k \Delta x}{2} \right) \tag{3.39}$$

Both are Toeplitz matrices ($a_{i,j} = a_{i+1,j+1}$) and have eigenfunctions of $e^{iknΔx}$. The system matrix AC governs the displacement vector Δw and the eigenvalue λ_k of the combined operator AC are given by

$$\lambda_k = \hat{A}_k \hat{C}_k = -\frac{G\bar{w}^3}{3\mu(1-\nu)\Delta x^3} \sin^3\left(\frac{|k|\Delta x}{2}\right) \tag{3.40}$$

For Euler's method, the time step is restricted by the form

$$\Delta t < \frac{6\mu(1-\nu)\Delta x^3}{G\bar{w}^3} \tag{3.41}$$

Similarly, for central difference scheme,

$$\Delta t < \frac{24\mu(1-\nu)\Delta x^3}{G\bar{w}^3} \tag{3.42}$$

The time step restrictions described above are for a Newtonian fluid. In case of non-Newtonian fluid $n' < 1$, the maximum allowable time step will be much smaller. Therefore, the use of implicit method is more attracted for the simulation of non-Newtonian fluid.

3.2.5 Implicit solutions

In implicit solutions, discretization of fluid flow equations is similar to explicit solutions, but the volume flow rate q_i and pressure p_i are in next time domain and they are determined from current state of displacement field as shown in Fig. 3.4. Therefore, with n elements, we obtain a system of n nonlinear equations with n unknowns.

For *Grid I*

The discretized continuity equation in *Gridn I* is given by

$$w_i^{m+1} + \frac{\Delta t}{2\Delta x}\left(q_{i+1}^{m+1} - q_{i-1}^{m+1}\right) = w_i^m, \quad \text{for } 2 \le i \le n-1 \tag{3.43a}$$

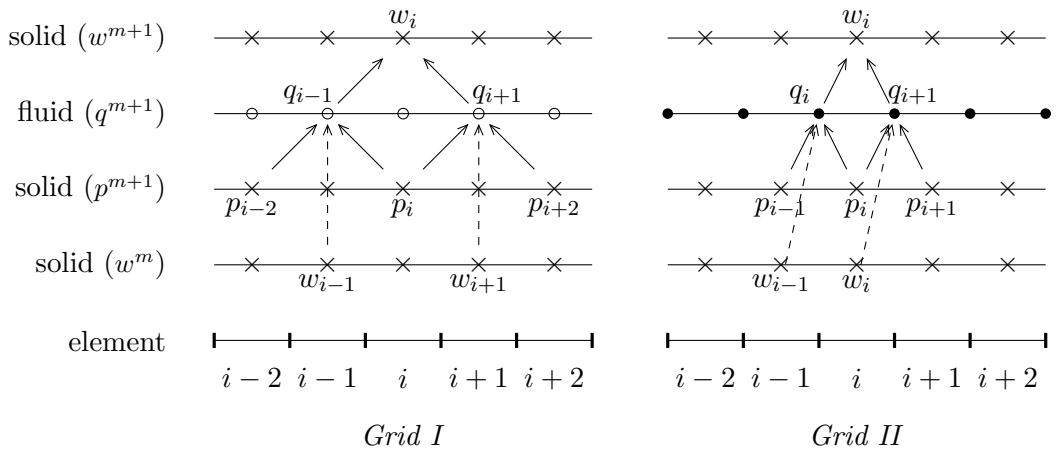

Figure 3.4: Implicit finite difference schemes

$$w_1^{m+1} + \frac{\Delta t}{2\Delta x}\left(q_2^{m+1} + \bar{q}_1^{m+1}\right) - w_{\text{inj}} = w_1^m \tag{3.43b}$$

$$w_n^{m+1} - \frac{\Delta t}{2\Delta x}\left(q_{n-1}^{m+1}\right) = w_n^m \tag{3.43c}$$

and the pressure gradient equation becomes

$$q_i^{m+1} = -\frac{n'}{2+4n'}\left[\frac{\left(w_i^{m+1}\right)^{2n'+1}}{2K'}\left(\frac{p_{i+1}^{m+1} - p_{i-1}^{m+1}}{2\Delta x}\right)\right]^{\frac{1}{n'}}, \quad \text{for } 2 \le i \le n-1 \tag{3.44a}$$

$$q_1^{m+1} = -\frac{n'}{2+4n'}\left[\frac{\left(w_1^{m+1}\right)^{2n'+1}}{2K'}\left(\frac{p_2^{m+1} - \bar{p}_1^{m+1}}{2\Delta x}\right)\right]^{\frac{1}{n'}} \tag{3.44b}$$

$$q_n^{m+1} = -\frac{n'}{2+4n'}\left[\frac{\left(w_n^{m+1}\right)^{2n'+1}}{2K'}\left(\frac{\bar{p}_n^{m+1} - p_{n-1}^{m+1}}{2\Delta x}\right)\right]^{\frac{1}{n'}} \tag{3.44c}$$

Finally, by combining continuity and pressure gradient equations, we have a system of nonlinear equations that the displacement field w^{m+1} and pressure field p^{m+1} in nest time domain can be solved from the current displacement w^m and boundary conditions.

$$w_i^{m+1} - \lambda_I\left\{\left[\left(w_{i+1}^{m+1}\right)^{2n'+1}\left(p_{i+2}^{m+1} - p_i^{m+1}\right)\right]^{\frac{1}{n'}} - \left[\left(w_{i-1}^{m+1}\right)^{2n'+1}\left(p_i^{m+1} - p_{i-2}^{m+1}\right)\right]^{\frac{1}{n'}}\right\}$$

$$= w_i^m, \quad \text{for } 3 \le i \le n-2 \tag{3.45a}$$

$$w_1^{m+1} - \lambda_I\left\{\left[\left(w_2^{m+1}\right)^{2n'+1}\left(p_3^{m+1} - p_1^{m+1}\right)\right]^{\frac{1}{n'}} + \left[\left(w_1^{m+1}\right)^{2n'+1}\left(p_2^{m+1} - p_1^{m+1}\right)\right]^{\frac{1}{n'}}\right\}$$

$$- w_{\text{inj}} = w_1^m \tag{3.45b}$$

$$w_2^{m+1} - \lambda_I \left\{ \left[\left(w_3^{m+1}\right)^{2n'+1} \left(p_4^{m+1} - p_2^{m+1}\right) \right]^{\frac{1}{n'}} - \left[\left(w_1^{m+1}\right)^{2n'+1} \left(p_2^{m+1} - p_1^{m+1}\right) \right]^{\frac{1}{n'}} \right\}$$

$$= w_2^m \tag{3.45c}$$

$$w_{n-1}^{m+1} - \lambda_I \left\{ \left[\left(w_n^{m+1}\right)^{2n'+1} \left(p_n^{m+1} - p_{n-1}^{m+1}\right) \right]^{\frac{1}{n'}} - \left[\left(w_{n-2}^{m+1}\right)^{2n'+1} \left(p_{n-1}^{m+1} - p_{n-3}^{m+1}\right) \right]^{\frac{1}{n'}} \right\}$$

$$= w_{n-1}^m \tag{3.45d}$$

$$w_n^{m+1} + \lambda_I \left[\left(w_{n-1}^{m+1}\right)^{2n'+1} \left(p_n^{m+1} - p_{n-2}^{m+1}\right) \right]^{\frac{1}{n'}} = w_n^m \tag{3.45e}$$

For *Grid II*

The fluid flow equation in *Grid II* can be obtained by applying same procedure of those in *Grid I*. The continuity and pressure becomes

$$w_i^{m+1} + \frac{\Delta t}{\Delta x}\left(q_{i+1}^{m+1} - q_i^{m+1}\right) = w_i^m, \quad \text{for } 2 \le i \le n-1 \tag{3.46a}$$

$$w_1^{m+1} + \frac{\Delta t}{\Delta x}\left(q_2^{m+1} - q_{\text{inj}}\right) = w_1^m \tag{3.46b}$$

$$w_n^{m+1} - \frac{\Delta t}{\Delta x} q_n^{m+1} = w_n^m \tag{3.46c}$$

and pressure gradient equations is

$$q_i^{m+1} = -\frac{n'}{2+4n'} \left[\frac{\left(w_{i-1}^{m+1}\right)^{2n'+1}}{2K'} \left(\frac{p_i^{m+1} - p_{i-1}^{m+1}}{\Delta x} \right) \right]^{\frac{1}{n'}}, \quad \text{for } 2 \le i \le n \tag{3.47}$$

By combining above equations, the implicit solution of fluid flow equations in *Grid II* are provided by

$$w_i^{m+1} - \lambda_{II} \left\{ \left[\left(w_i^{m+1}\right)^{2n'+1} \left(p_{i+1}^{m+1} - p_i^{m+1}\right) \right]^{\frac{1}{n'}} - \left[\left(w_{i-1}^{m+1}\right)^{2n'+1} \left(p_i^{m+1} - p_{i-1}^{m+1}\right) \right]^{\frac{1}{n'}} \right\}$$

$$= w_i^m, \quad \text{for } 2 \le i \le n-1 \tag{3.48a}$$

$$w_1^{m+1} - \lambda_{II} \left[\left(w_1^{m+1}\right)^{2n'+1} \left(p_2^{m+1} - p_1^{m+1}\right) \right]^{\frac{1}{n'}} - w_{\text{inj}} = w_1^m \tag{3.48b}$$

$$w_n^{m+1} + \lambda_{II}\left[\left(w_{n-1}^{m+1}\right)^{2n'+1}\left(p_n^{m+1} - p_{n-1}^{m+1}\right)\right]^{\frac{1}{n'}} = w_n^m \tag{3.48c}$$

3.3 Numerical solvers for implicit method

3.3.1 System of nonlinear equations and merit function

The implicit numerical solutions for given in Eq. (3.45) and Eq. (3.48) for both grid systems can be expressed by a function vector r_i to solve the system of n nonlinear equations by setting $r_i = 0$. The solution of the displacement in next time domain w^{m+1} is obtained by minimizing r_i or the merit function $f(x)$, given by [45]

$$f(x) = \sum_{i=1}^{n} r_i^2(x) = \| r(x) \|_2^2 \tag{3.49}$$

Several numerical algorithms are introduced to solve the system of n nonlinear equations $r(x)$ by minimizing the merit function $f(x)$. The equations r_i is given by following.

For *Grid I*

$$r_i = w_i - \lambda_I \left\{ \left[(w_{i+1})^{2n'+1}\left(p_{i+2} - p_i\right)\right]^{\frac{1}{n'}} - \left[(w_{i-1})^{2n'+1}\left(p_i - p_{i-2}\right)\right]^{\frac{1}{n'}} \right\} - w_i^0,$$

$$\text{for } 3 \le i \le n-2 \tag{3.50a}$$

$$r_1 = w_1 - \lambda_I \left\{ \left[(w_2)^{2n'+1}\left(p_3 - p_1\right)\right]^{\frac{1}{n'}} + \left[(w_1)^{2n'+1}\left(p_2 - p_1\right)\right]^{\frac{1}{n'}} \right\} - w_{\text{inj}} - w_1^0 \tag{3.50b}$$

$$r_2 = w_2 - \lambda_I \left\{ \left[(w_3)^{2n'+1}\left(p_4 - p_2\right)\right]^{\frac{1}{n'}} - \left[(w_1)^{2n'+1}\left(p_2 - p_1\right)\right]^{\frac{1}{n'}} \right\} - w_2^0 \tag{3.50c}$$

$$r_{n-1} = w_{n-1} - \lambda_I \left\{ \left[(w_n)^{2n'+1}\left(p_n - p_{n-1}\right)\right]^{\frac{1}{n'}} - \left[(w_{n-2})^{2n'+1}\left(p_{n-1} - p_{n-3}\right)\right]^{\frac{1}{n'}} \right\} - w_{n-1}^0 \tag{3.50d}$$

$$r_n = w_n + \lambda_I \left[(w_{n-1})^{2n'+1}\left(p_n - p_{n-2}\right)\right]^{\frac{1}{n'}} - w_n^0 \tag{3.50e}$$

For *Grid II*

$$r_i = w_i - \lambda_{II}\left\{\left[(w_i)^{2n'+1}(p_{i+1}-p_i)\right]^{\frac{1}{n'}} - \left[(w_{i-1})^{2n'+1}(p_i-p_{i-1})\right]^{\frac{1}{n'}}\right\} - w_i^0,$$

$$\text{for } 2 \le i \le n-1 \tag{3.51a}$$

$$r_1 = w_1 - \lambda_{II}\left[(w_1)^{2n'+1}(p_2-p_1)\right]^{\frac{1}{n'}} - w_{\text{inj}} - w_1^0 \tag{3.51b}$$

$$r_n = w_n + \lambda_{II}\left[(w_{n-1})^{2n'+1}(p_n-p_{n-1})\right]^{\frac{1}{n'}} - w_n^0 \tag{3.51c}$$

Through explicit and implicit solution, only the right hand side of crack is modeled. The equivalent elasticity equation is

$$p_i = \sum_{j=1}^{N} A_{ij} w_j = p_f - \sigma_{\text{situ}} \tag{3.52}$$

where the influence coefficients are given by

$$A_{ij} = -\frac{G}{\pi(1-\nu)}\left[\frac{a_j}{(x_i-x_j)^2-(a_j)^2} + \frac{a_j}{(x_i+x_j)^2-(a_j)^2}\right], \quad 1 \le j \le n-1 \tag{3.53a}$$

$$A_{ij} = -\frac{G}{2\pi(1-\nu)}\left\{\left[\frac{\sqrt{2}}{S_1-2a_j} + \frac{1}{2\sqrt{a_j S_1}}\ln\left|\frac{\sqrt{S_1}-\sqrt{2a_j}}{\sqrt{S_1}+\sqrt{2a_j}}\right|\right] + \left[\frac{\sqrt{2}}{S_2-2a_j} + \frac{1}{2\sqrt{a_j S_2}}\ln\left|\frac{\sqrt{S_2}-\sqrt{2a_j}}{\sqrt{S_2}+\sqrt{2a_j}}\right|\right]\right\}, \quad j = n \tag{3.53b}$$

and $S_1 = a_j + |\bar{x}_i - x_j|$ and $S_2 = a_j + |\bar{x}_i + x_j|$

3.3.2 Newton iteration

From multi-variable Taylor series, the nonlinear equation $r_i(w_i + \Delta)$ can be expressed by

$$\begin{aligned} r_i(w_1+\Delta w_1, w_2+\Delta w_2, \cdots, w_{n-1}+\Delta w_{n-1}, w_n+\Delta w_n) = \\ r_i(w_1, w_2, \cdots, w_{n-1}, w_n) + \frac{\partial r_i}{\partial w_1}\Delta w_1 + \frac{\partial r_i}{\partial w_2}\Delta w_2 + \\ \cdots + \frac{\partial r_i}{\partial w_{n-1}}\Delta w_{n-1} + \frac{\partial f_i}{\partial w_n}\Delta w_n \end{aligned} \tag{3.54}$$

Let $r_i(w_i + \Delta)$ equals to zero and guess the initial values of $\hat{w}_j$, then above equation can be expanded into a first-order truncated Taylor series about $\hat{w}_j$, given by

$$\sum_j \frac{\partial r_i}{\partial w_j} \Delta w_j = -r_i(\hat{w}_1, \hat{w}_2, \ldots, \hat{w}_N) \tag{3.55}$$

where the partial derivatives are the Jacobian matrix evaluated with the initial guesses. The Jacobian matrix J is given by

$$J = \frac{\partial r_i}{\partial w_j} = \begin{bmatrix} \frac{\partial r_1}{\partial w_1} & \frac{\partial r_1}{\partial w_2} & \cdots & \frac{\partial r_1}{\partial w_n} \\ \frac{\partial r_2}{\partial w_1} & \frac{\partial r_2}{\partial w_2} & \cdots & \frac{\partial r_2}{\partial w_n} \\ \vdots & \vdots & \ddots & \vdots \\ \frac{\partial r_n}{\partial w_1} & \frac{\partial r_n}{\partial w_2} & \cdots & \frac{\partial r_n}{\partial w_n} \end{bmatrix} \tag{3.56}$$

and Δw_j and r_i are vectors given by

$$\Delta w = [\Delta w_1, \Delta w_2, \cdots, \Delta w_N]^T \tag{3.57}$$

$$r = [r_1, r_2, \cdots, r_N]^T \tag{3.58}$$

The partial derivatives can be evaluated analytically or by a difference approximation.

$$\frac{\partial r_i}{\partial w_j} \approx \frac{r_i(\hat{w}_1, \ldots, \hat{w}_j + \delta w_j, \ldots, \hat{w}_N) - r_i(\hat{w}_1, \ldots, \hat{w}_j, \ldots, \hat{w}_N)}{\delta w_j} \tag{3.59}$$

where δw_j is an arbitrarily chosen small value.

If we choose Δw as the solution vector p, then we can define a model function $m(p)$ given by

$$m_k(p) = r(w_k) + J(w_k)p \tag{3.60}$$

Then we can obtain the solution vector p_k for which $m_k(p_k) = 0$,

$$p_k = -J(w_k)^{-1} r(w_k) \tag{3.61}$$

The algorithm for Newton iteration is given by

choose initial guess w_0

for $k = 0, 1, 2, \ldots$ **do**

calculate $J(w_k)$ and $r(w_k)$

solve Newton equation for p_k

$p_k = -J(w_k)^{-1} r(w_k)$

update initial value w

$w_{k+1} \leftarrow w_k + p_k$

end for

Algorithm 3.1: Newton iteration

There are some deficiencies in Newton iteration [45].

- If the initial point is remote from a solution, this method behave erratically
- The Jacobian matrix may be difficult to obtain
- It may be too expensive to obtain p_k when n is large
- When j is singular or near singular (ill-conditioned), p_k will not be well defined

Some of these deficiencies can be overcomed by numerical techniques such as modification of Jacobian matrix, quasi-Newton method and Line search method.

3.3.3 Ill-conditioned Jacobian

Singular value decomposition (SVD)

In case when the Jacobian matrix J is ill-conditioned, we can approximate the inverse of J by the singular value decomposition given by [46]

$$J = U \begin{bmatrix} S \\ 0 \end{bmatrix} V^T = \begin{bmatrix} U_1 & U_2 \end{bmatrix} \begin{bmatrix} S \\ 0 \end{bmatrix} V^T = U_1 S V^T \tag{3.62}$$

where

U is $m \times m$ orthogonal matrix

U_1 contains the first n columns of U

U_2 contains the last n columns of U

V is $n \times n$ orthogonal matrix

S is $n \times n$ diagonal matrix with elements $\sigma_1 \geq \sigma_2 \geq \cdots \geq \sigma_n \geq 0$

The diagonal elements are modified by

$$S^{-1} = \begin{cases} 1/\sigma_i & \text{for } \sigma_i > t \\ 0 & \text{otherwise} \end{cases} \tag{3.63}$$

where t is a small constant.

Then the Newton direction p_k can be found by

$$p_k = -V S^{-1} U_1^T r(w_k) \tag{3.64}$$

Levenberg-Marquardt method

When the Jacobian matrix is near singular, the newton direction can be modified by making the Hessian matrix non-singular. From the quadratic model of the objective function,

$$m_k(p) = r_k + \nabla r_k^T p + \frac{1}{2} p^T B_k p \tag{3.65}$$

The solution vector p_k is given by

$$p_k = -B_k^- 1 \nabla r_k \tag{3.66}$$

where the approximate Hessian B_k and gradient ∇r_k can be defined by

$$B_k = J_k^T J_k \tag{3.67}$$

$$\nabla r_k = J_k^T r_k \tag{3.68}$$

The modified newton direction can be obtained by adding a $\lambda_k I$ to Hessian matrix [47].

$$p_k = -\left(J_k^T J_k + \lambda_k I\right)^{-1} J_k^T r_k \tag{3.69}$$

λ_k allow modified Hessian not to approach to singularity. Explicit calculation of $J_k^T J_k$ is heavy when n is large. But we know the Cholesky factor of $(J_k^T J_k + \lambda_k I)$ is identical to R^T, where R is the upper triangular factor of QR factorization of

$$\begin{bmatrix} J \\ \sqrt{\lambda} I \end{bmatrix}$$

Then the solution vector p_k can be easily found by solving following equation

$$R^T R p_k = -J_k^T r_k \tag{3.70}$$

The disadvantage of this approach is that it is difficult to choose λ_k. If it is too large, the convergence of Newton iteration will be lost. In case λ_k is too small, it is obvious that the Jacobian is still ill-conditioned [45].

Modified Cholesky factorization

Another method to avoid singularity of Jacobian matrix is a Cholesky factorization of Hessian B_k. In usual Cholesky factorization is given by $B = LDL^T$, where L is a lower triangular matrix with unit diagonal elements and D is a diagonal matrix with positive diagonal elements. In modified Cholesky algorithm, the diagonal elements are increased to make Hessian sufficiently positive [45]. The procedure is given by

for $j = 1, 2, \ldots, n$ **do**

$c_{ij} \leftarrow a_{jj} - \sum_{s=1}^{j-1} d_s l^2 js$

$d_j \leftarrow c_{jj}$

for $i = j + 1, \ldots, n$ **do**

$c_{ij} \leftarrow a_{ij} - \sum_{s=1}^{j-1} d_s l_{is} ljs$

$l_{ij} \leftarrow c_{ij}/d_j$

end for

end for

Algorithm 3.2: Modified Cholesky factorization

Then the modified Newton step p_k can be obtained by solving

$$MM^T p_k = -J_k^T r_k \tag{3.71}$$

where $M = LD^{1/2}$.

3.3.4 Quasi-Newton method

If the function $r(x)$ is twice differentiable, the second order Taylor series gives a quadratic model of the objective function

$$m_k(p) = r_k + \nabla r_k^T p + \frac{1}{2} p^T B_k p \tag{3.72}$$

where ∇r is the gradient of the objective function and B is the Hessian matrix or its approximate. Then the solution vector can be defined by setting $m_k(p) = 0$

$$p_k = -B_k^{-1} \nabla r_k \tag{3.73}$$

In quasi-Newton method, the approximate Hessian matrix are updated using following equations without calculation of exact Hessian at every iteration. The four famous update formula are described [45, 48–50].

$$B_{k+1} = \begin{cases} \left(I - \dfrac{y_k p_k^T}{y_k^T p_k}\right) B_k \left(I - \dfrac{p_k y_k^T}{y_k^T p_k}\right) + \dfrac{y_k y_k^T}{y_k^T p_k} & \text{DFP} \\ B_k + \dfrac{y_k y_k^T}{y_k^T p_k} - \dfrac{B_k p_k (B_k p_k)^T}{p_k^T B_k p_k} & \text{BFGS} \\ B_k + \dfrac{y_k - B_k p_k}{p_k^T p_k} p_k^T & \text{Broyden} \\ B_k + \dfrac{(y_k - B_k p_k)(y_k - B_k p_k)^T}{(y_k - B_k p_k)^T p_k} & \text{SR1} \end{cases} \tag{3.74}$$

where, $y_k = \nabla r_{k+1} - \nabla r_k$.

An inverse of Hessian can be directly updated using the Sherman-Morrison formula given by [51]

$$(A + uv^T)^{-1} = A^{-1} - \frac{A^{-1} u v^T A^{-1}}{1 + v^T A^{-1} u}, \quad 1 + v^T A^{-1} u \neq 0 \tag{3.75}$$

where, A is an invertible matrix, u, v are vectors.

Then the inversed form of Hessian matrices are obtained by

$$H_{k+1} = B_{k+1}^{-1} = \begin{cases} H_k + \dfrac{p_k p_k^T}{y_k^T p_k} - \dfrac{H_k y_k y_k^T H_k^T}{y_k^T H_k y_k} & \text{DFP} \\ \left(I - \dfrac{y_k p_k^T}{y_k^T p_k}\right)^T H_k \left(I - \dfrac{y_k p_k^T}{y_k^T p_k}\right) + \dfrac{p_k p_k^T}{y_k^T p_k} & \text{BFGS} \\ H_k + \dfrac{(p_k - H_k y_k) p_k^T H_k}{p_k^T H_k y_k} & \text{Broyden} \\ H_k + \dfrac{(p_k - H_k y_k)(p_k - H_k y_k)^T}{(p_k - H_k y_k)^T y_k} & \text{SR1} \end{cases} \tag{3.76}$$

The solution vector p_k can be found by

$$p_k = -H_k \nabla r_k \tag{3.77}$$

When the model function m_k is defined as a linear model

$$m_k(p) = r(x) + B_k p \tag{3.78}$$

where B_k is the approximate Jacobian to be updated.

The quasi-Newton BFGS method for crack propagation is studied in [52]. We use Broyden's formula for updating the approximate Jacobian. The Broyden's formula is same as given in the quadratic model, but use $y_k = r(x_{k+1}) - r(x_k)$ [48].

3.3.5 Line search method

Basically, the implicit numerical solvers generate a sequence of iteration to update the solution vector p_k. The iteration stops when the change of p_k, values of r_i or merit function m_i is within acceptable accuracy ϵ. The key strategies are how to get the direction and magnitude to move the point x_k to the next state x_{k+1} to find roots or to minimize merit function. We have already discussed Newton and quasi-Newton method to find the direction

p_k which minimize the merit function m_k. The magnitude, the step length, α_k can be obtained by the line search method or the trust region method. The line search method generates a limited number of trial step length to find new position can approximate the minimum of $\min_{\alpha>0} f(x_k+\alpha p_k)$. This process is repeated at new point to find the next direction p_{k+1} and step length α_{k+1}.

The updated position can be replaced by

$$x_{k+1} = x_k + \alpha_k p_k \tag{3.79}$$

The exact step length α_k can be achieved by solving the equations [45]

$$\frac{\partial \phi(\alpha)}{\partial \alpha} = 0, \quad \frac{\partial^2 \phi(\alpha)}{\partial \alpha^2} < 0 \tag{3.80}$$

where $\phi(\alpha) = m(x + \alpha p)$. the analytical line search requires an explicit expression for $\phi(\alpha)$ and $\partial\phi(\alpha)/\partial\alpha$ which are not always available in numerical solutions. Therefore, simple inexact line search algorithms are preferred.

Wolfe conditions

A decent direction condition must be satisfied to utilize line search method. This condition ensure the function r can be reduced along this direction.

$$p_k^T \nabla r_k < 0, \quad \text{for linear model} \tag{3.81a}$$

$$p_k^T \nabla r_k = -\nabla r_k^T B_k^{-1} \nabla r_k < 0, \quad \text{for quadratic model} \tag{3.81b}$$

One of popular inexact line search method is the strong Wolfe conditions require α_k to satisfy [45, 49, 53]

$$f(x_k + \alpha_k p_k) \leq f(x_k) + c_1 \alpha_k \nabla f_k^T p_k \tag{3.82a}$$

$$|\nabla f(x_k + \alpha_k p_k)^T p_k| \leq c_2 |\nabla f_k^T p_k| \tag{3.82b}$$

where $0 < c_1 < c_2 < 1$. For a system of n nonlinear equations, the merit function f and the gradient ∇f are given by

$$f(x) = \frac{1}{2}\|r(x)\|^2 = \frac{1}{2}\sum_{i=1}^{n} r_i^2(x) \tag{3.83}$$

$$\nabla f(x) = J(x)^T r(x) \tag{3.84}$$

In loose line search, the parameters are given by $c_1 = 10^{-4}$ and $c_2 = 0.9$. The first is sufficient decrease condition and the second is curvature condition. The sufficient decrease condition ensure that the reduction in function m is proportional to the step length α_k and the directional derivative $\nabla r_k^T p_k$. The curvature condition indicates that the slope of $\phi(\alpha_k)$ should be larger than $c2$ times the initial slope $\phi'(0)$. The line search is performed in two stages. First, a trial step length is increased from the initial value α_1 until it satisfy the both conditions. If trial value is within an interval, the second stage is performed to reduce the interval and find an acceptable step length. Both stages are described in Algorithm 3.3 and Algorithm 3.4.

set $\alpha_0 \leftarrow 0$, choose $\alpha_{\max} > 0$ and $\alpha_1 \in (0, \alpha_{\max})$

$i \leftarrow 1$

repeat

evaluate $\phi(\alpha_i)$

if $\phi(\alpha_i) > \phi(0) + c_1\alpha_i\phi'(0)$ or $[\phi(\alpha_i) \geq \phi(\alpha_{i-1})$ and $i > 1]$ **then**

$\alpha_* \leftarrow$ **zoom**(α_{i-1}, α_i) and **stop**

end if

evaluate $\phi'(\alpha_i)$

if $|\phi'(\alpha_i)| \leq -c_2\phi'(0)$ **then**

$\alpha_* \leftarrow \alpha_i$ and **stop**

end if

if $\phi'(\alpha_i) \geq 0$ **then**

$\alpha_* \leftarrow$ **zoom** (α_i, α_{i-1}) and **stop**

end if

choose $\alpha_{i+1} \in (\alpha_i, \alpha_{\max})$

$i \leftarrow i + 1$;

until $i > i_{max}$

Algorithm 3.3: Strong Wolfe line search

repeat

interpolate to find a trial step length α_j between α_{lo} and α_{hi}

evaluate $\phi(\alpha_j)$

if $\phi(\alpha_j) > \phi(0) + c_1\alpha_j\phi'(0)$ or $\phi(\alpha_j) \geq \phi(\alpha_{\text{lo}})$ **then**

$\alpha_{\text{hi}} \leftarrow \alpha_j$

else

evaluate $\phi'(\alpha_j)$

end if

if $|\phi'(\alpha_j)| \leq -c_2\phi'(0)$ **then**

set $\alpha_* \leftarrow \alpha_j$ and **stop**

end if

if $\phi'(\alpha_j)(\alpha_{\text{hi}} - \alpha_{\text{lo}}) \geq 0$ **then**

$\alpha_{\text{hi}} \leftarrow \alpha_{\text{lo}}$

$\alpha_{\text{lo}} \leftarrow \alpha_j$

end if

$i \leftarrow i + 1$;

until $i > i_{max}$

Algorithm 3.4: zoom

Backtracking line search

The backtracking method is to find the trial step length α_k by the sufficient decrease condition in Eq. (3.82a).

$$f(x_k + \alpha_k p_k) \leq f(x_k) + c\alpha_k \nabla f_k^T p_k \tag{3.85}$$

It starts from the initial step length of α_0 and decrease until the trial step satisfy the sufficient decrease condition after several trials. the initial value α_0 is usually set to 1 and $c = 10^{-4}$. The procedure is summarized in Algorithm 3.5.

choose $\alpha_0 > 0$, $\rho \in (0, 1)$, $c \in (0, 1)$

set $\alpha = \alpha_0$

repeat

$\alpha \leftarrow \rho\alpha$

until $f(x_k + \alpha_k p_k) \leq f(x_k) + c\alpha_k \nabla f_k^T p_k$

Algorithm 3.5: Backtracking line search

The solution procedure of Newton iteration with line search is explained in Algorithm 3.6.

given c_1, c_2 with $0 < c_1 < c_2 < \frac{1}{2}$ and $c = c_1$

choose x_0

for $k = 0, 1, 2, \ldots$ **do**

calculate p_k from one of

if J is ill-conditioned **then**

Singular value decomposition Eq. (3.64)

Levenberg-Mardquardt Eq. (3.70)

Modified Cholesky factorization Eq. (3.71)

else

Newton equation Eq. (3.61)

Quasi-Newton Broyden's formula Eq. (3.77)

end if

if $\alpha = 0$ satisfy the strong Wolfe conditions Eq. (3.82a) and Eq. (3.82b) or sufficient decrease condition Eq. (3.85) **then**

$\alpha_k = 1$

else

perform strong Wolfe (Algorithm 3.3 and Algorithm 3.4) or backtracking (Algorithm 3.5) line search to find $\alpha > 0$ satisfy the given conditions

end if

$x_{k+1} \leftarrow x_k + \alpha p_k$

end for

Algorithm 3.6: Newton iteration with line search

3.3.6 Trust-Region method

Basically, the trust-region method is to find the step p by approximately solving the equation

$$\min_p m_k(x_k + p), \quad \text{where } x_k + p \text{ lies inside the trust region} \tag{3.86}$$

If the p doesn't provide a sufficient reduction in f, we declare that the current trust region is too large and reduce the size of the region to solve the above equation. Usually, the trust region is defined by $\| p \|_2 \leq \Delta$, where the scalar $\Delta > 0$. The trust region's approach is differ from the line search method. While the line search method fix the direction p_k and seek the optimal distance α_k, the trust region method defines a maximum distance λ_k first and seek a optimal direction p_k within the trust region constraint. If the step is unsatisfactory, the size of trust region is reduced and tried again to find p_k within the reduced trust region. The detailed procedure of trust-region method can be found in [45, 49, 50, 54]

Let merit function $f(x) = \frac{1}{2}\|r(x)\|_2^2$ and using the approximate Hessian $B_k = J(x_k)^T J(x_k)$, the model function $m_k(p)$ is defined by

$$m_k(p) = \frac{1}{2}\|r_k + J_k p\|_2^2 = f_k + p^T J^T r_k + \frac{1}{2} p^T J_k^T J_k p_k \tag{3.87}$$

The step p_k is an approximate solution of the subproblem

$$\min_p m_k(p), \qquad \text{subject to } \|p\| \leq \Delta_k, \tag{3.88}$$

where Δ_k is the radius of the trust region. and the ratio ρ_k of actual to predicted reduction is used to determine the trust region at each iteration.

$$\rho_k = \frac{\|r(x_k)\|^2 - \|r(x_k + p_k)\|^2}{\|r(x_k)\|^2 - \|r(x_k) + J(x_k)p_k\|^2} \tag{3.89}$$

The detailed procedure is listed in Algorithm 3.7.

Trust-region dogleg method

The dogleg method is one of the methods for solving the trust region subproblem in Eq. (3.88). This method obtain the solution of the subproblem based on the Cauchy point p_k^c. The Cauchy point is given by [45]

$$p_k^c = -\tau_k(\Delta_k/\|J_k^T r_k\|)J_k^T r_k \tag{3.90}$$

where $\tau_k = \min\{1, \|J_k^T r_k\|^3/(\Delta_k r_k^T J_k(J_k^T J_k)J_k^T r_k)\}$

Then, the solution step p_k is determined by

$$p_k = \begin{cases} p_k^c, & \text{if } \|p_k^c\| = \Delta_k \\ \\ p_k^c + \lambda(p_k^J - p_k^c), \text{ such that } \|p_k\| \leq \Delta_k, & \text{else} \end{cases} \tag{3.91}$$

where λ is the largest value in $[0, 1]$ and p_k^J is evaluated from Newton equation Eq. (3.61).

set $\bar{\Delta} > 0$, $\Delta_0 \in (0, \bar{\Delta})$ and $\eta \in [0, \frac{1}{4})$

for $k = 0, 1, 2, \ldots$ **do**

calculate p_k as an approximate solution of Eq. (3.88)

evaluate ρ_k from Eq. (3.89)

if $\rho_k < 1/4$ **then**

$\Delta_{k+1} = 1/4 \parallel p_k \parallel$

else

if $\rho_k < 3/4$ and $\parallel p_k \parallel = \Delta_k$ **then**

$\Delta_{k+1} = \min(2\Delta_k, \bar{\Delta})$

else

$\Delta_{k+1} = \Delta_k$

end if

end if

if $\rho < \eta$ **then**

$x_{k+1} = x_k + p_k$

else

$x_{k+1} = x_k$

end if

end for

Algorithm 3.7: Trust region algorithm

Trust-region method combined with Newton line search

The trust region method can be combined with other techniques in constructing algorithms. When the evaluated trial step p_k from trust region method is a decent direction, but it is not acceptable because $f(x_k + p_k) \geq f(x_k)$, it is possible to try line search along the trial step to satisfy $f(x_k + p_k) < f(x_k)$ [55]. The backtracking line search method is proposed and implemented in trust region algorithm just before the trust region radius is reduced.

3.4 Parameters and numerical solver settings

The numerical solution of a plane crack problem is performed with the given parameters including rock, fluid properties and simulation parameters. The required parameters are listed in Table 3.1. For implicit solutions, settings for numerical solvers also must be provided as given in Table 3.2.

Parameters			
G	shear modulus(Pa)	ν	Poisson's ratio
K_{Ic}	fracture toughness(MPa$\sqrt{\text{m}}$)		
K'	consistency index(Pa $\cdot$ s$^{n'}$)	n'	power-law index
q	volume flow rate(m^2/s)	σ	in-situ stress (Pa)
ϵ	termination criterion	Δt, Δx, L_0, $L_{\max}$, $t_{\max}$	

Table 3.1: Simulation parameters

Solver settings and options	
Solver	1. NTL: Newton method with line search 2. TRL: Trust-region (dogleg) method combined with line search 3. QNB: Quasi-Newton Broyden's method with line search
Grid	1. Grid I (5 points, nodes(w,p) = nodes(q)) 2. Grid II (3 points, nodes$(w,p) \neq$ nodes(q))
Jacobian	1. Analytical 2: Numerical
Line Search	1. Strong Wolfe conditions 2. Backtracking method
Ill-conditioned J	1. Singular value decomposition 2. Levenberg-Marquardt method 3. Modified Cholesky factorization
Crack tip	1. Use special crack tip element 2. No use

Table 3.2: Solver settings and options

3.5 Results

The explicit and implicit simulations of crack growth model are performed with the parameters given in Table 3.3. The simulation results of explicit solution is given in Table 3.4. The crack propagation is driven by a Newtonian fluid ($n' = 1.0$) up to 300m with the injection rate $q = 0.05$ m^2/s. The time step is determined by CFL condition. It is shown that the *Grid II* has an advantage in volume difference, but the *Grid I* use less computation time because the time step determined by CFL condition is much larger than the one obtained

Simulation parameters					
G	$= 1.0$ GPa	ν	$= 0.2$	K_{Ic}	$= 0.5$ MPa$\sqrt{\mathrm{m}}$
q	$= 0.01 \leq q \leq 0.11$ m^2/s	n'	$= 0.25 \leq n' \leq 1.0$	K'	$= 0.001$ Pa $\cdot$ s$^{n'}$
L_0	$= 25$m	$L_{\max}$	$= 2000$m	Δx	$= 5$m
Δt	$= 1$s				

Table 3.3: Simulation parameters (crack growth model)

from *Grid II*. Therefore, if the volume difference in *Grid I* is in acceptable range, the use of *Grid I* is preferred in explicit solution. The simulation results of implicit crack growth

Grid	Δt	**No. of time steps**	**CPU time**	**Volume difference**
I	5.5×10^{-4} s	158100	12s	0.3 %
II	3.5×10^{-5} s	1189587	96s	0.0 %

Table 3.4: Simulation results (explicit model)

model are compared in Table 3.5. First, the line search are compared in Newtons iteration solver. Line search methods overcome a drawback of Newton iteration algorithm on lower indexed fluid. The strong Wolfe conditions gives more accurate step length α_k. Total number of iteration is smaller than the other line search method but the algorithm costs more computations resulting slower solution. The backtracking line search requires more iteration than the strong Wolfe conditions but the simplicity of its algorithm makes the computation time less than the Wolfe conditions. Second, the grid systems are compared in trust-region algorithm. In explicit method, *Grid I* showed a better performance in computation time, but in implicit solution, *Grid I* is slower than *Grid II* and unstable with lower indexed fluid. The quasi-Newton shows remarkable speed in computation time with higher indexed

fluid although the numbers of iterations are much larger than the Newton iteration and trust-region method. This is because the quasi-Newton Broyden's update formula doesn't require the process for inverting large matrices. But quasi-Newton Broyden's method has serious limitations when the fluid's power-law index n' is very small. Newton iteration with backtracking line search seems good choice in computation speed and convergence if fluid's power-law index n' is not extremely small ($n' < 0.25$). The trust region method costs a little more computation time and number of iteration, but it showed more robust performance than Newton iteration when the various simulation parameters were given. The crack lengths for varying power-law index n' are given in Fig. 3.5. The time to create

iteration (CPU time)

Solver	**Line**	**Grid**	**Powe-law index (n')**			
			0.25	0.5	0.75	1.0
NTL	Wolfe	II	9958 (100s)	6711 (67s)	5920 (65s)	7580 (82s)
	Back		9992 (61s)	6874 (40s)	5967 (40s)	7571 (51s)
	None		-	9256 (45s)	6886 (41s)	7569 (50s)
TRL	Back	I	12183 (81s)	9648 (67s)	6104 (45s)	7790 (61s)
		II	10004 (60s)	6900 (46s)	5967 (44s)	7571 (55s)
QNB	Back	II	-	15837 (64s)	7397 (24s)	9006 (31s)

*Δt=0.25s is used in QNB for $n' = 0.5$, Δt=0.5s is used in TRL for $n' = 0.25, 0.5$

Table 3.5: Comparisons of numerical solvers for $q = 0.05$ m^2/s

2000m crack is reduced by using a lower indexed fluid. In the same condition, the injection time for $n' = 0.25$ is 49% of when a Newtonian fluid ($n' = 1.0$) is used. This fact allows us to use less volume of fracturing fluid as shown in Fig. 3.7. Basically, the injection time

and volume of fracturing fluid can be reduced by using a lower n' fluid, but the decrease in injection time from $n' = 0.3$ to $n' = 0.25$ is only 14.8% of the decrease in time from $n' = 1.0$ to $n' = 0.95$. The advantage in use of a lower indexed fluid is not noticeable when n' is small enough. The use of crack tip element also gives more accurate stress intensity factor K_I.

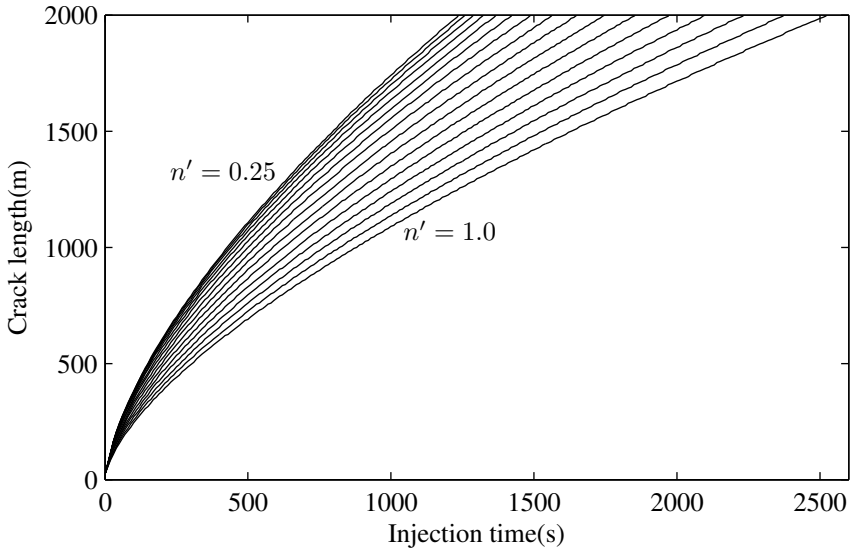

Figure 3.5: Growth of crack with time

Therefore, it prevent overestimating initiation of crack. As shown in Fig. 3.6, the ordinary element overestimates the injection time by 13.5% less than the crack tip element when the crack reaches to 2000m.

When the hydraulic fracturing is started, the higher fluid pressure is required to break down the formation and to give enough stress for propagation. But, once the crack starts growing, the well bore pressure is decreased as given in Fig. 3.8. The lower indexed fluid also make the crack propagates under less well bore pressure.

The distribution of fluid pressure is given in Fig. 3.9. The pressure gradient of $n' = 0.25$

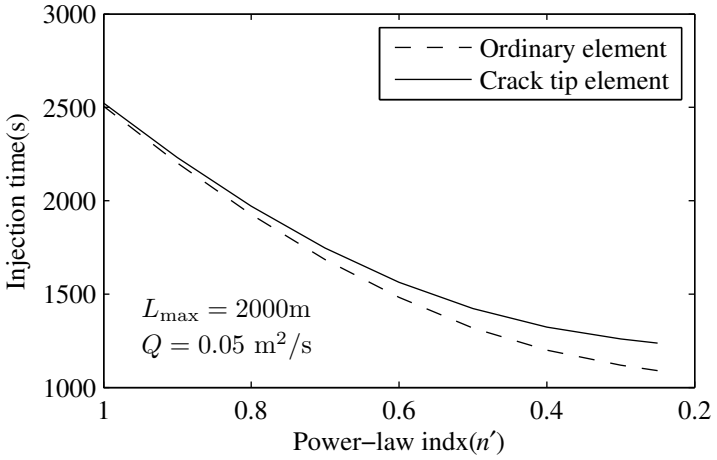

Figure 3.6: Special crack tip element

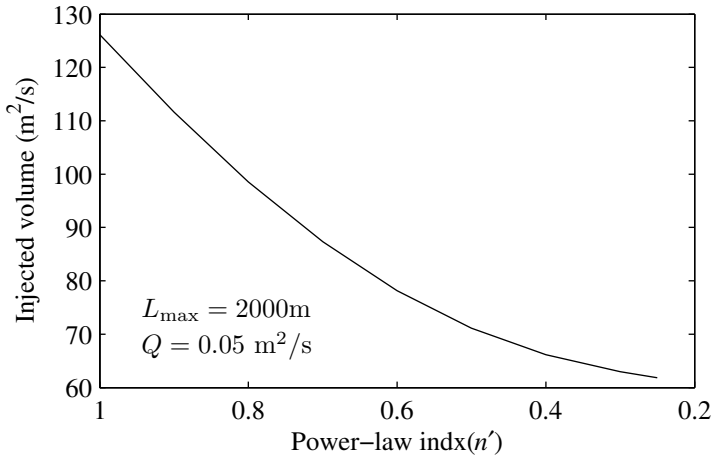

Figure 3.7: Injected fluid volume

fluid along the length of crack, except the crack tip region, is very small compare to the higher n' fluid. This makes the system unstable when the numerical solution is performed because the numerical solutions of this kind of problem Eq. (3.26) and Eq. (3.27) are based on the gradient of pressure inside crack.

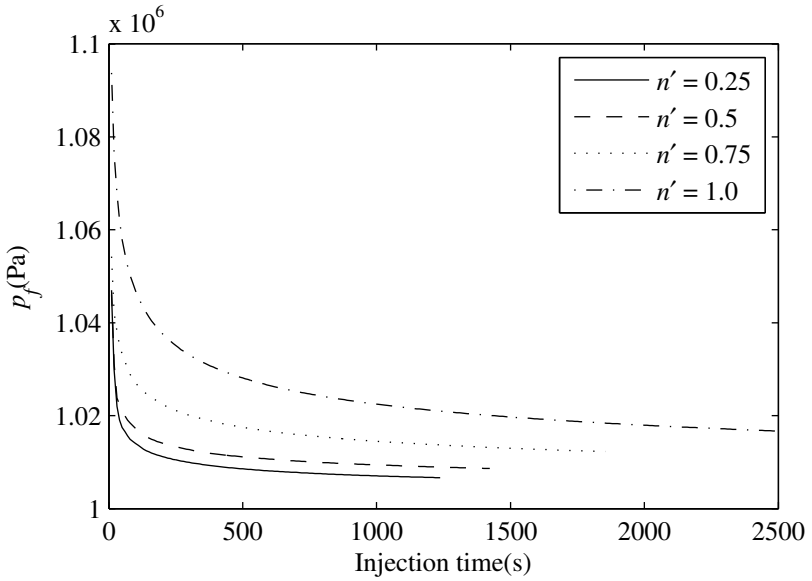

Figure 3.8: Decrease in well bore pressure

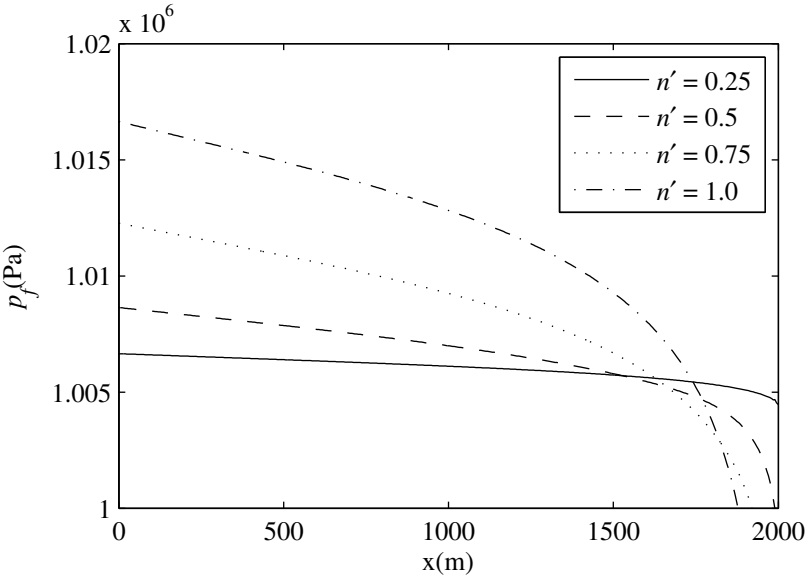

Figure 3.9: Pressure distribution inside crack

Chapter 4

Analysis of crack propagation under mixed loading condition

4.1 Curved crack problem and dislocation based solution

4.1.1 Coordinate transformation

For two orthogonal bases $\mathbf{e}$ and $\bar{\mathbf{e}}$, there is an orthogonal tensor Q such that $\bar{\mathbf{e}}_\mathbf{i} = Q\mathbf{e}_\mathbf{i}$. The transformation rules for a displacement vector u and stress tensor σ in the basis $\mathbf{e}$ to a $\bar{u}$ and $\bar{\sigma}$ in the basis $\bar{\mathbf{e}}$ are given by [56]

$$\bar{u}_i = Q_{ij} u_j \tag{4.1a}$$

$$\bar{\sigma}_{ij} = Q_{ik} Q_{jl} \sigma_{kl} \tag{4.1b}$$

The orthogonal tensor Q is expressed as the directional cosine between the two coordinate systems.

$$Q_{ij} = \bar{\mathbf{e}}_\mathbf{i} \cdot \mathbf{e}_\mathbf{j} = \cos(\bar{\mathbf{e}}_\mathbf{i}, \mathbf{e}_\mathbf{j}) \tag{4.2}$$

Additionally, a displacement vector in another local coordinate system $\hat{x} - \hat{y}$ can also be

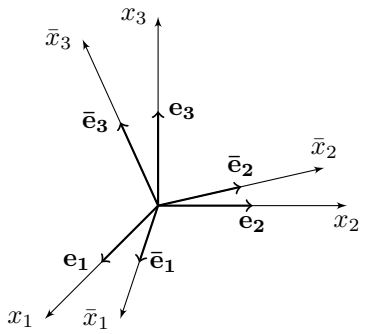

Figure 4.1: Coordinate systems

transformed to the local axis $\bar{x} - \bar{y}$ by following relationships,

$$\bar{u} = \bar{Q}u \tag{4.3a}$$

$$\hat{u} = \hat{Q}u \tag{4.3b}$$

$$\bar{u} = \bar{Q}\hat{Q}^T\hat{u} \tag{4.3c}$$

For a crack under uniform stresses σ_{xx}, σ_{yy} and σ_{xy}, the displacement u and stress σ in local coordinate $\bar{x}$ and $\bar{y}$ which is rotated by θ from $x - y$ axis are expressed in matrix form below

$$\begin{Bmatrix} \bar{x} \\ \bar{y} \end{Bmatrix} = \begin{bmatrix} \cos\theta & \sin\theta \\ -\sin\theta & \cos\theta \end{bmatrix} \begin{Bmatrix} x \\ y \end{Bmatrix} \tag{4.4a}$$

$$\begin{Bmatrix} u_{\bar{x}} \\ u_{\bar{y}} \end{Bmatrix} = \begin{bmatrix} \cos\theta & \sin\theta \\ -\sin\theta & \cos\theta \end{bmatrix} \begin{Bmatrix} u_x \\ u_y \end{Bmatrix} \tag{4.4b}$$

$$\begin{Bmatrix} \sigma_{\bar{x}\bar{x}} \\ \sigma_{\bar{y}\bar{y}} \\ \sigma_{\bar{x}\bar{y}} \end{Bmatrix} = \begin{bmatrix} \cos^2\theta & \sin^2\theta & 2\cos\theta\sin\theta \\ \sin^2\theta & \cos^2\theta & -2\cos\theta\sin\theta \\ -\cos\theta\sin\theta & \cos\theta\sin\theta & \cos^2\theta - \sin^2\theta \end{bmatrix} \begin{Bmatrix} \sigma_{xx} \\ \sigma_{yy} \\ \sigma_{xy} \end{Bmatrix} \tag{4.4c}$$

The shear and normal stresses at local element can be expressed by

$$\sigma_n = \sigma_{\bar{y}\bar{y}} = \sigma_{xx}\sin^2\theta + \sigma_{yy}\cos^2\theta - 2\sigma_{xy}\cos\theta\sin\theta \tag{4.5a}$$

$$\sigma_t = \sigma_{\bar{x}\bar{y}} = -\sigma_{xx}\cos\theta\sin\theta + \sigma_{yy}\cos\theta\sin\theta + \sigma_{xy}\cos^2\theta - \sin^2\theta \tag{4.5b}$$

4.1.2 Edge dislocation

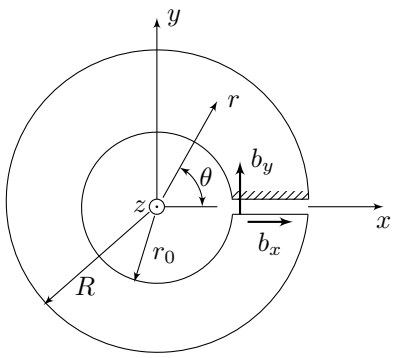

Figure 4.2: Edge dislocation [57]

Consider a hollow circular cylinder of infinite length and made of isotropic and elastic solid as shown in Fig. 4.2. The cylinder is cut and dislocated along the x direction and displace the lower side to y direction. By assuming a plane strain condition about to the direction of length and traction free on the surface of the cylinder, the Airy's stress function is given by [57]

$$\phi = -\frac{Gb_x}{\pi(\kappa+1)}\left[2r\ln r\sin\theta + \frac{1}{R^2+r_0^2}\left(R^2r_0^2\frac{\sin\theta}{r} - r^3\sin\theta\right)\right] \tag{4.6}$$

where G is the shear modulus and κ is the Kolosov's constant given by

$$\kappa = \begin{cases} 3-4\nu & \text{for plane strain} \\ \dfrac{3-\nu}{1+\nu} & \text{for plane stress} \end{cases} \tag{4.7}$$

where, ν is the Poisson's ratio.

The singular edge dislocation in the unbounded isotropic material can be obtained by letting

$R \to \infty$ and $r_0 \to 0$ in (1). The Airy stress function for a glide dislocation b_x in plane strain becomes

$$\phi = -kb_x r \ln r \sin\theta, \qquad \lambda = \frac{G}{2\pi(1-\nu)} \tag{4.8}$$

The governing equation that determines the elastic field is

$$\nabla^4 \phi = \left(\frac{\partial^2}{\partial x^2} + \frac{\partial^2}{\partial y^2}\right)\left(\frac{\partial^2}{\partial x^2} + \frac{\partial^2}{\partial y^2}\right)\phi = 0 \tag{4.9}$$

In polar coordinates,

$$\left(\frac{\partial^2}{\partial r^2} + \frac{1}{r}\frac{\partial}{\partial r} + \frac{1}{r^2}\frac{\partial^2}{\partial \theta^2}\right)^2 \phi = 0 \tag{4.10}$$

The derivatives of the stress function produce the stress components for two-dimensional problem of elasticity in the form

$$\sigma_{xx} = \frac{\partial^2 \phi}{\partial x^2}, \qquad \sigma_{yy} = \frac{\partial^2 \phi}{\partial y^2}, \qquad \sigma_{xy} = -\frac{\partial^2 \phi}{\partial x \partial y} \tag{4.11}$$

In terms of polar or cylindrical coordinates,

$$\sigma_{rr} = \frac{1}{r}\frac{\partial \phi}{\partial r} + \frac{1}{r^2}\frac{\partial^2 \phi}{\partial \theta^2}, \qquad \sigma_{\theta\theta} = \frac{\partial^2 \phi}{\partial r^2}, \qquad \sigma_{r\theta} = -\frac{\partial}{\partial r}\left(\frac{1}{r}\frac{\partial \phi}{\partial \theta}\right) \tag{4.12}$$

The Michell solution gives the corresponding stress and displacement components [58, 59].

$$\sigma_{rr} = \sigma_{\theta\theta} = -\lambda b_x \frac{\sin\theta}{r} \tag{4.13a}$$

$$\sigma_{r\theta} = \lambda b_x \frac{\cos\theta}{r} \tag{4.13b}$$

$$u_r = -\frac{\lambda b_x}{2\mu}\left[(1-2\nu)\ln r \sin\theta - 2(1-\nu)\theta\cos\theta - \frac{1}{2}\sin\theta\right] \tag{4.13c}$$

$$u_\theta = -\frac{\lambda b_x}{2\mu}\left[(1-2\nu)\ln r \cos\theta + 2(1-\nu)\theta\sin\theta + \frac{1}{2}\cos\theta\right] \tag{4.13d}$$

The stress and displacement components for Cartesian coordinate system are

$$u_x = \frac{b_x}{2\pi}\left[\theta + \frac{1}{2(1-\nu)}\frac{xy}{r^2}\right] \tag{4.14a}$$

$$u_y = -\frac{b_x}{2\pi}\left[\frac{1-2\nu}{2(1-\nu)}\ln r + \frac{1}{2(1-\nu)}\frac{x^2}{r^2}\right] \tag{4.14b}$$

$$\sigma_{xx} = -\lambda b_x \frac{y}{r^4}(3x^2+y^2) \tag{4.14c}$$

$$\sigma_{yy} = \lambda b_x \frac{y}{r^4}(x^2-y^2) \tag{4.14d}$$

$$\sigma_{xy} = \lambda b_x \frac{x}{r^4}(x^2-y^2) \tag{4.14e}$$

For a climb edge dislocation with the Burgers vector b_y can be obtained by rotating the coordinate axes. Thus, the Airy stress function is

$$\phi = -kb_y r \ln r \cos\theta, \qquad \lambda = \frac{G}{2\pi(1-\nu)} \tag{4.15}$$

Then, the stress components for Cartesian coordinate system are

$$\sigma_{xx} = kb_y \frac{x}{r^4}(x^2-y^2) \tag{4.16a}$$

$$\sigma_{yy} = kb_y \frac{x}{r^4}(x^2+3y^2) \tag{4.16b}$$

$$\sigma_{xy} = kb_y \frac{y}{r^4}(x^2-y^2) \tag{4.16c}$$

With Burgers vector **b** having components b_x and b_y at the origin, the stress induced at a point (x, y) are given by

$$\sigma_{xx}(x,y) = \lambda\left\{b_x\left[-\frac{y}{r^4}(3x^2+y^2)\right] + b_y\left[\frac{x}{r^4}(x^2-y^2)\right]\right\} \tag{4.17a}$$

$$\sigma_{yy}(x,y) = \lambda\left\{b_x\left[\frac{y}{r^4}(x^2-y^2)\right] + b_y\left[\frac{x}{r^4}(x^2+3y^2)\right]\right\} \tag{4.17b}$$

$$\sigma_{xy}(x,y) = \lambda\left\{b_x\left[\frac{x}{r^4}(x^2-y^2)\right] + b_y\left[\frac{y}{r^4}(x^2-y^2)\right]\right\} \tag{4.17c}$$

Consider the stress induced at a point (x, y) in an infinite medium, due to a dislocation at position (ξ, η), the stresses in the global coordinate system are given by [58],

$$\begin{Bmatrix}\sigma_{xx}(x,y)\\ \sigma_{yy}(x,y)\\ \sigma_{xy}(x,y)\end{Bmatrix} = \lambda\left\{b_x\begin{bmatrix}f_{xxx}\\ f_{xyy}\\ f_{xxy}\end{bmatrix} + b_y\begin{bmatrix}f_{yxx}\\ f_{yyy}\\ f_{yxy}\end{bmatrix}\right\} \tag{4.18}$$

and the influence functions are given by

$$f_{xxx}(\bar{x},\bar{y}) = -\frac{\bar{y}}{r^4}\left(3\bar{x}^2+\bar{y}^2\right) \tag{4.19a}$$

$$f_{xyy}(\bar{x},\bar{y}) = \frac{\bar{y}}{r^4}\left(\bar{x}^2-\bar{y}^2\right) \tag{4.19b}$$

$$f_{xxy}(\bar{x},\bar{y}) = \frac{\bar{x}}{r^4}\left(\bar{x}^2-\bar{y}^2\right) \tag{4.19c}$$

$$f_{yxx}(\bar{x},\bar{y}) = \frac{\bar{x}}{r^4}\left(\bar{x}^2-\bar{y}^2\right) \tag{4.19d}$$

$$f_{yyy}(\bar{x},\bar{y}) = \frac{\bar{x}}{r^4}\left(\bar{x}^2+3\bar{y}^2\right) \tag{4.19e}$$

$$f_{yxy}(\bar{x},\bar{y}) = \frac{\bar{y}}{r^4}\left(\bar{x}^2-\bar{y}^2\right) \tag{4.19f}$$

where $\bar{x} = x-\xi, \quad \bar{y} = y-\eta$ and $r^2 = \bar{x}^2+\bar{y}^2$

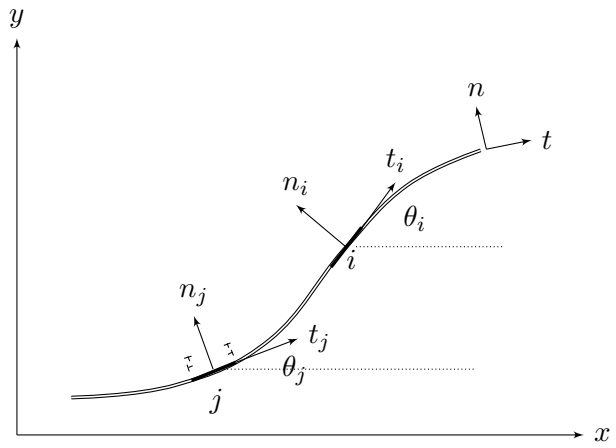

Figure 4.3: Curved crack in local coordinates

Consider a curved crack as shown in Fig. 4.3. The stresses at the ith element located at the center of a line segment between $(x_i-\alpha, y_i-\beta)$ and $(x_i+\alpha, y_i+\beta)$ due to the Burgers vector b_x^j and b_y^j on the line segment between $(x_j-\xi, y_j-\eta)$ to $(x_j+\xi, y_j+\eta)$. The inclined

angle of each segment θ_i and θ_j are given by $\arctan\dfrac{\beta}{\alpha}$ and $\arctan\dfrac{\xi}{\eta}$, respectively. Then the transformation of local systems to the global coordinate can be achieved by

$$\begin{Bmatrix} n^i \\ t^i \end{Bmatrix} = \begin{bmatrix} \cos\theta_i & \sin\theta_i \\ -\sin\theta_i & \cos\theta_i \end{bmatrix} \begin{Bmatrix} x \\ y \end{Bmatrix} \tag{4.20}$$

$$\begin{Bmatrix} n^j \\ t^j \end{Bmatrix} = \begin{bmatrix} \cos\theta_j & \sin\theta_j \\ -\sin\theta_j & \cos\theta_j \end{bmatrix} \begin{Bmatrix} x \\ y \end{Bmatrix} \tag{4.21}$$

We define the transformation matrix with θ_i as q_i and the one with θ_j as q_j

The normal and shear stresses at ith element can be obtained by

$$\sigma_t^i = K_{tt} b_x^j + K_{tn} b_y^j \tag{4.22a}$$

$$\sigma_n^i = K_{nt} b_x^j + K_{nn} b_y^j \tag{4.22b}$$

where the influence factor K are given by

$$\begin{Bmatrix} K_{tt} \\ K_{tn} \end{Bmatrix} = \lambda \begin{bmatrix} Q_{tt} & Q_{tn} \\ Q_{nt} & Q_{nn} \end{bmatrix} \begin{Bmatrix} f_{xxy}^R - f_{xxy}^L \\ f_{yxy}^R - f_{yxy}^L \end{Bmatrix} \tag{4.23a}$$

$$\begin{Bmatrix} k_{nt} \\ k_{nn} \end{Bmatrix} = \lambda \begin{bmatrix} Q_{tt} & Q_{tn} \\ Q_{nt} & Q_{nn} \end{bmatrix} \begin{Bmatrix} f_{xyy}^R - f_{xyy}^L \\ f_{yyy}^R - f_{yyy}^L \end{Bmatrix} \tag{4.23b}$$

The components of transformation matrix Q is given by

$$Q = q_i q_j^T \tag{4.24}$$

The influence functions are evaluated based on the distances transformed to the local coordinates of ith element.

$$f_{lmn}^R = f_{lmn}(q_t^i[x_i - (x_j + \xi), y_i - (y_j + \eta)]^T, q_n^i[x_i - (x_j + \xi), y_i - (y_j + \eta)]^T) \tag{4.25a}$$

$$f_{lmn}^L = f_{lmn}(q_t^i[x_i - (x_j - \xi), y_i - (y_j - \eta)]^T, q_n^i[x_i - (x_j - \xi), y_i - (y_j - \eta)]^T) \tag{4.25b}$$

where the normal and transverse transformation vectors are given by

$$q_t^i = [\cos\theta_i \ \ \sin\theta_i] \tag{4.26a}$$

$$q_n^i = [-\sin\theta_i \;\; \cos\theta_i] \tag{4.26b}$$

4.1.3 Displacement discontinuity on curved crack

Consider a curved plane crack subjected to a stress field. From Eq. (4.22), The shear and normal stresses at the midpoint of the ith element in the figure can be expressed in terms of the displacement discontinuity components at the jth element as follows

$$\sigma_t^i = K_{tt}^{ij} u_t^j + K_{tn}^{ij} u_n^j \tag{4.27a}$$

$$\sigma_n^i = K_{nt}^{ij} u_t^j + K_{nn}^{ij} u_n^j \tag{4.27b}$$

The stresses of ith element due to the displacement discontinuities at all n segments are

$$\sigma_t^i = \sum_{j=1}^{n} K_{tt}^{ij} u_t^j + \sum_{j=1}^{n} K_{tn}^{ij} u_n^j \tag{4.28a}$$

$$\sigma_n^i = \sum_{j=1}^{n} K_{nt}^{ij} u_t^j + \sum_{j=1}^{n} K_{nn}^{ij} u_n^j \tag{4.28b}$$

We can wright the equations in matrix form,

$$\begin{bmatrix} K_{tt} & K_{tn} \\ K_{nt} & K_{nn} \end{bmatrix} \begin{Bmatrix} u_t \\ u_n \end{Bmatrix} = \begin{Bmatrix} \sigma_t \\ \sigma_n \end{Bmatrix} \tag{4.29}$$

If a crack under in-situ stress σ is opened by internal fracturing fluid flow, σ_n is replaced with $p_f - \sigma_n$. Then, the normal and shear displacements can be found by

$$u_n = (K_{nn} - K_{nt}K_{tt}^{-1}K_{tn})^{-1}(p_f - \sigma_n - K_{nt}K_{tt}^{-1}\sigma_t) \tag{4.30}$$

$$u_t = K_{tt}^{-1}(\sigma_t - K_{tn}u_n) \tag{4.31}$$

The fluid pressure is given by

$$p_f = (K_{nn} - K_{nt}K_{tt}^{-1}K_{tn})u_n + K_{nt}K_{tt}^{-1}\sigma_t + \sigma_n \tag{4.32}$$

4.2 Crack propagation criteria

In practical engineering problems, cracks are usually subjected to mixed mode loading. The both K_I and K_{II} are exist on crack surface. The initiation of crack and propagation angle can be determined by using combination of the opening and glide mode stress intensity factors. This combination provides a criterion to predict the path of propagating crack. Various crack initiation criteria have been proposed in literature such as maximum circumferential tensile stress, maximum strain energy release rate and minimum strain energy density criterion. Additionally, we discuss a basic propagation angle prediction based on the ratio of stress intensity factors and numerical method to find the propagation angle that minimize the shear stress.

4.2.1 Maximum circumferential tensile stress

The maximum circumferential tensile stress criterion was introduced by Erdogan and Sih [60]. The criterion predicts the crack extension starts from its tip along the radial direction θ_c on which $\sigma_{\theta\theta}$ becomes maximum when $\sigma_{\theta\theta}$ reaches a critical stress σ_c equal to the fracture stress in uniaxial tension. When a crack is subjected to a mixed mode stress field governed by the values of the opening mode K_I and sliding mode K_{II} stress intensity factor. The singular polar stress components near the crack tip are expressed by

$$\sigma_{rr} = \frac{K_I}{\sqrt{2\pi r}}\left(\frac{5}{4}\cos\frac{\theta}{2} - \frac{1}{4}\cos\frac{3\theta}{2}\right) + \frac{K_{II}}{\sqrt{2\pi r}}\left(-\frac{5}{4}\sin\frac{\theta}{2} + \frac{3}{4}\sin\frac{3\theta}{2}\right) \tag{4.33a}$$

$$\sigma_{\theta\theta} = \frac{K_I}{\sqrt{2\pi r}}\left(\frac{3}{4}\cos\frac{\theta}{2} + \frac{1}{4}\cos\frac{3\theta}{2}\right) + \frac{K_{II}}{\sqrt{2\pi r}}\left(-\frac{3}{4}\sin\frac{\theta}{2} - \frac{3}{4}\sin\frac{3\theta}{2}\right) \tag{4.33b}$$

$$\sigma_{r\theta} = \frac{K_I}{\sqrt{2\pi r}}\left(\frac{1}{4}\sin\frac{\theta}{2} + \frac{1}{4}\sin\frac{3\theta}{2}\right) + \frac{K_{II}}{\sqrt{2\pi r}}\left(\frac{1}{4}\cos\frac{\theta}{2} + \frac{3}{4}\cos\frac{3\theta}{2}\right) \tag{4.33c}$$

Then the maximum circumferential tensile stress is defined by

$$\frac{\partial \sigma_{\theta\theta}}{\partial \theta} = 0, \quad \frac{\partial^2 \sigma_{\theta\theta}}{\partial \theta^2} < 0 \tag{4.34}$$

$$\sigma_{\theta\theta}(\theta_c) = \sigma_c \tag{4.35}$$

The circumferential stress $\sigma_{\theta\theta}$ in the direction of crack extension is a principal stress and the shear stress $\sigma_{r\theta}$ for that direction vanishes. The crack extension angle θ_c is calculated by

$$K_I \left(\sin\frac{\theta}{2} + \sin\frac{3\theta}{2} \right) + K_{II} \left(\cos\frac{\theta}{2} + \cos\frac{3\theta}{2} \right) = 0 \tag{4.36}$$

or

$$K_I \sin\theta + K_{II}(3\cos\theta - 1) = 0 \tag{4.37}$$

The angle θ_c can be determined by iterative method or analytically

$$\theta_c = 2\arctan\frac{1}{4}\left(\frac{1}{\lambda} - \sqrt{\frac{1}{\lambda^2} + 8} \right), \; K_{II} > 0 \tag{4.38}$$

$$\theta_c = 2\arctan\frac{1}{4}\left(\frac{1}{\lambda} + \sqrt{\frac{1}{\lambda^2} + 8} \right), \; K_{II} < 0 \tag{4.39}$$

where $\lambda = K_{II}/K_I$

The maximum hoop stress is given by

$$\sigma_{\theta\theta}(\theta_c) = \frac{K_I}{\sqrt{2\pi r}} \cos\frac{\theta_c}{2} \left(1 - \sin^2\frac{\theta_c}{2} \right) + \frac{K_{II}}{\sqrt{2\pi r}} \left(-\frac{3}{4}\sin\frac{\theta_c}{2} - \frac{3}{4}\sin\frac{3\theta_c}{2} \right) \tag{4.40}$$

The crack initiation occurs when $\sigma_{\theta\theta}(\theta_c)$ reaches the critical stress $\frac{K_{Ic}}{\sqrt{2\pi r}}$. Therefore, the equivalent stress intensity factor for mixed mode loading is given by

$$K_{eq} = K_I \cos^3\frac{\theta_c}{2} - \frac{3}{2} K_{II} \cos\frac{\theta_c}{2} \sin\theta_c \tag{4.41}$$

4.2.2 Minimum strain energy density

The strain energy density criterion is introduced by Sih [42]. This criterion predicts the crack propagates along the direction which the strain energy density becomes minimum when the strain energy density factor reaches to its critical value.

The strain energy density function can be evaluated from

$$\frac{\mathrm{d}W}{\mathrm{d}V} = \int_0^{\epsilon_{ij}} \sigma_{ij} \mathrm{d}\epsilon_{ij} \tag{4.42}$$

where σ_{ij} and ϵ_{ij} are the stress and strain components

For the plane strain elasticity problems,

$$\frac{\mathrm{d}W}{\mathrm{d}V} = \frac{1}{4\mu}\left[(1-\nu)(\sigma_{xx}+\sigma_{yy})^2 - 2(\sigma_{xx}\sigma_{yy}-\sigma_{xy}^2)\right] \tag{4.43}$$

The strain energy density function $\mathrm{d}W/\mathrm{d}V$ decays with distance r from the crack tip. Then $\mathrm{d}W/\mathrm{d}V$ will be assumed to have the form [61]

$$\frac{\mathrm{d}W}{\mathrm{d}V} = \frac{S}{r} \tag{4.44}$$

The factor S can be defined as $r(\mathrm{d}W/\mathrm{d}V)$ and it represents the local energy energy release for a crack growth r.

For crack propagation in a mixed mode condition, the minimum strain energy density factor can be determined by relations

$$\frac{\partial S}{\partial \theta} = 0, \quad \frac{\partial^2 S}{\partial \theta^2} > 0 \tag{4.45}$$

And crack will initiate when

$$S(\theta_c) = S_c \tag{4.46}$$

where the critical strain energy density factor S_c is given by

$$S_c = \frac{(1-2\nu)}{4\pi\mu} K_{Ic}^2 \tag{4.47}$$

The singular stress field near the crack tip is given by

$$\sigma_{xx} = \frac{K_I}{\sqrt{2\pi r}} \cos\frac{\theta}{2}\left(1 - \sin\frac{\theta}{2}\sin\frac{3\theta}{2}\right) - \frac{K_{II}}{\sqrt{2\pi r}} \sin\frac{\theta}{2}\left(2 + \cos\frac{\theta}{2}\cos\frac{3\theta}{2}\right) \tag{4.48a}$$

$$\sigma_{yy} = \frac{K_I}{\sqrt{2\pi r}} \cos\frac{\theta}{2}\left(1 + \sin\frac{\theta}{2}\sin\frac{3\theta}{2}\right) + \frac{K_{II}}{\sqrt{2\pi r}} \sin\frac{\theta}{2}\sin\frac{\theta}{2}\cos\frac{\theta}{2}\cos\frac{3\theta}{2} \tag{4.48b}$$

$$\sigma_{xy} = \frac{K_I}{\sqrt{2\pi r}} \cos\frac{\theta}{2}\sin\frac{\theta}{2}\cos\frac{3\theta}{2} + \frac{K_{II}}{\sqrt{2\pi r}} \cos\frac{\theta}{2}\left(1 - \sin\frac{\theta}{2}\sin\frac{3\theta}{2}\right) \tag{4.48c}$$

By substituting Eq. (4.48) into Eq. (4.43), we obtain the following quadratic form of the strain energy density factor S

$$S = c_{11}k_I^2 + 2c_{12}k_I k_{II} + c_{22}k_{II}^2 \tag{4.49}$$

where the coefficients $c_{ij}(i,j=1,2)$ are given by

$$c_{11} = \frac{1}{16\mu}(1+\cos\theta)(3-4\nu-\cos\theta) \tag{4.50}$$

$$c_{12} = \frac{1}{16\mu}\sin\theta\left[2\cos\theta - (2-4\nu)\right] \tag{4.51}$$

$$c_{22} = \frac{1}{16\mu}\left[(4-4\nu)(1-\cos\theta) + (1+\cos\theta)(3\cos\theta - 1)\right] \tag{4.52}$$

and $k_j = K_j/\sqrt{\pi}$ $(j = I, II)$

By substituting Eq. (4.49) into Eq. (4.45) we obtain

$$\left[\cos\theta - (1-2\nu)\right]\sin\theta k_I^2 + 2\left[\cos 2\theta - (1-2\nu)\cos\theta\right]k_I k_{II} + \left[(1-2\nu-3\cos\theta)\sin\theta\right]k_{II}^2 = 0 \tag{4.53}$$

$$\left[\cos\theta - (1-2\nu)\cos\theta\right]k_I^2 + 2\left[(1-2\nu)\sin\theta - 2\sin 2\theta\right]k_I k_{II} + \left[(1-2\nu)\cos\theta - 3\cos 2\theta\right]k_{II}^2 > 0 \tag{4.54}$$

The crack initiation angle θ_c can be obtained by solving Eq. (4.53) and Eq. (4.54).

4.2.3 Maximum strain energy release rate

The maximum energy release rate criterion is proposed by Erdogan and Sih [60]. This theory is based on Griffith energy theory and predicts the crack will propagate along the direction that the elastic energy release per unit length is maximum when the energy reaches its critical value.

The relation between the stress intensity factors $K_I(\theta)$ and $K_{II}(\theta)$ for a crack with an infinitesimal kink at an angle θ and the stress intensity factors K_I and K_{II} of the original crack is given by [62]

$$K_I(\theta) = \kappa(\theta)\left(K_I - \frac{3}{2}K_{II}\sin\theta\right) \tag{4.55a}$$

$$K_{II}(\theta) = \kappa(\theta)\left(K_{II} - \frac{1}{2}K_I\sin\theta\right) \tag{4.55b}$$

where

$$\kappa(\theta) = \left(\frac{4}{3+\cos^2\theta}\right)\left(\frac{1-\theta/\pi}{1+\theta/\pi}\right)^{\frac{\theta}{2\pi}} \tag{4.56}$$

By substitution of Eq. (4.55) to Irwin's energy release rate equation, we obtain

$$G(\theta) = \frac{2G}{1-\nu}\left(K_I^2(\theta) + K_{II}^2(\theta)\right) \tag{4.57}$$

Then, above equation becomes

$$G(\theta) = \frac{8G}{1-\nu}\left(\frac{1}{3+\cos^2\theta}\right)\left(\frac{1-\theta/\pi}{1+\theta/\pi}\right)^{\frac{\theta}{2\pi}}\left[\left(1+3\cos^2\theta\right)K_I^2 - 8\sin\theta\cos\theta K_I K_{II} + \left(9-5\cos^2\theta\right)K_{II}^2\right] \tag{4.58}$$

The crack initiation occurs when the $G(\theta_c)$ reaches to its critical value of $G_c = \dfrac{2G}{1-\nu}K_{Ic}^2$. And, the angle θ_c can be determined by solving the equations

$$\frac{\partial G(\theta)}{\partial \theta} = 0, \quad \frac{\partial^2 G(\theta)}{\partial \theta^2} < 0 \tag{4.59}$$

The angle θ_c is limited by $-75.2\,\text{deg} \leq \theta \leq 75.2\,\text{deg}$ where the limits are for pure mode II loading.

4.2.4 Minimum local shear stress

The minimum local shear stress criterion is basically similar to the maximum circumferential tensile stress criterion, but this theory is based on displacement discontinuity method which is numerical method. When the mode I stress intensity factor K_I at the crack tip element reaches the critical stress intensity factor K_{Ic}, the initiation angle θ_c is determined by follow. The initial range is reasonably set to $\theta_1 \leq \theta_c \leq \theta_2$. we assume the crack is extended by unit crack length Δl to each angle. Then the local shear stress caused by displacement discontinuities in main crack is calculated. The local shear stress is given by

$$\sigma_t^{\theta_i} = \sum_{j=1}^{n} K_{tt}^{\theta_i j} u_t^j + \sum_{j=1}^{n} K_{tn}^{\theta_i j} u_n^j \tag{4.60}$$

where the influence coefficient K^{θ_i} is evaluated at $\left(x_{\text{tip}} + \frac{\Delta l}{2}\cos\theta_i, y_{\text{tip}} + \frac{\Delta l}{2}\sin\theta_i\right)$ by displacement discontinuity method in curved crack problem Eq. (4.23) and Eq. (4.28). When the local shear stress $\sigma_t^{\theta_i}$ is successfully defined at the angle θ_1 and θ_2, the crack initiation angle θ_c can be determined by the secant iterative root finding method given by

$$\theta_i = \theta_{i-1} - f(\theta_{i-1})\frac{\theta_{i-1} - \theta_{i-2}}{f(\theta_{i-1}) - f(\theta_{i-2})} \tag{4.61}$$

where $f(\theta_i) = \sigma_t^{\theta_i}$.

4.2.5 Crack path comparison

Propagation of an inclined crack under tensile field

Consider an inclined crack under tensile as shown in Fig. 4.4. The displacement discontinuity equation is given in Eq. (4.28) with locally transformed components. The tensile stress is kept increasing to open and propagate the crack. The crack propagation criteria discussed in previous section are compared. The simulation parameters are listed in Table 4.1.

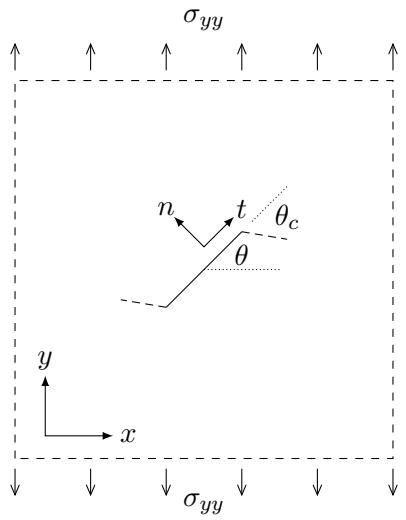

Figure 4.4: Inclined crack under tensile

Simulation parameters					
G	$= 1.0$ GPa	ν	$= 0.2$	K_{Ic}	$= 0.5$ MPa$\sqrt{m}$
L_0	$= 20$m	$L_{\max}$	$= 100$m	θ_0	$= \pi/6$
Δx	$= 1$m	σ_{yy}	$= 1.0\times10^4 - 1.0 \times 10^6$ Pa		

[H]

Table 4.1: Simulation parameters (inclined tensile crack)

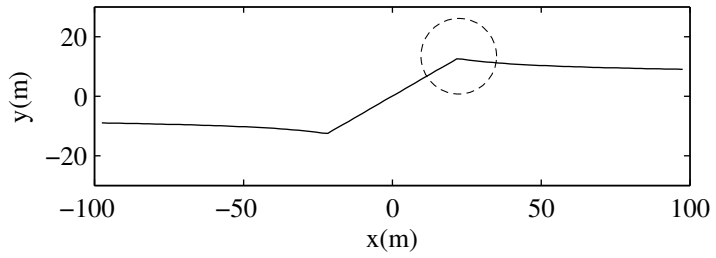

Figure 4.5: Crack path prediction based on crack propagation criteria

The predicted crack path in given conditions is shown in Fig. 4.5. The detailed comparison of crack path predictions in different criteria are shown in Fig. 4.6 and Fig. 4.7. In the first ten initiation of crack (dotted area in Fig. 4.5), the minimum local shear stress, stress intensity factor ratio and minimum strain energy density criterion show smoother predictions while the maximum hoop stress and minimum energy release rate criterion are a little scattered along their mean path.

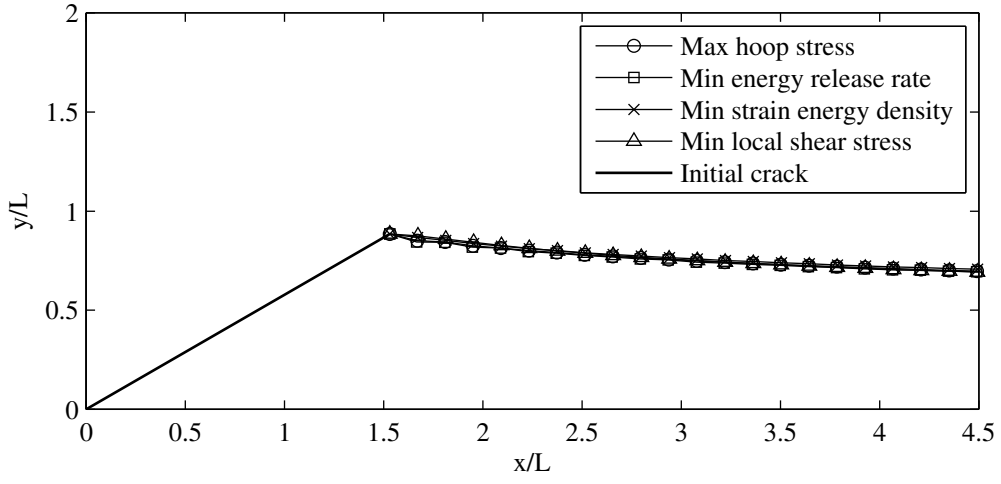

Figure 4.6: Crack path comparison

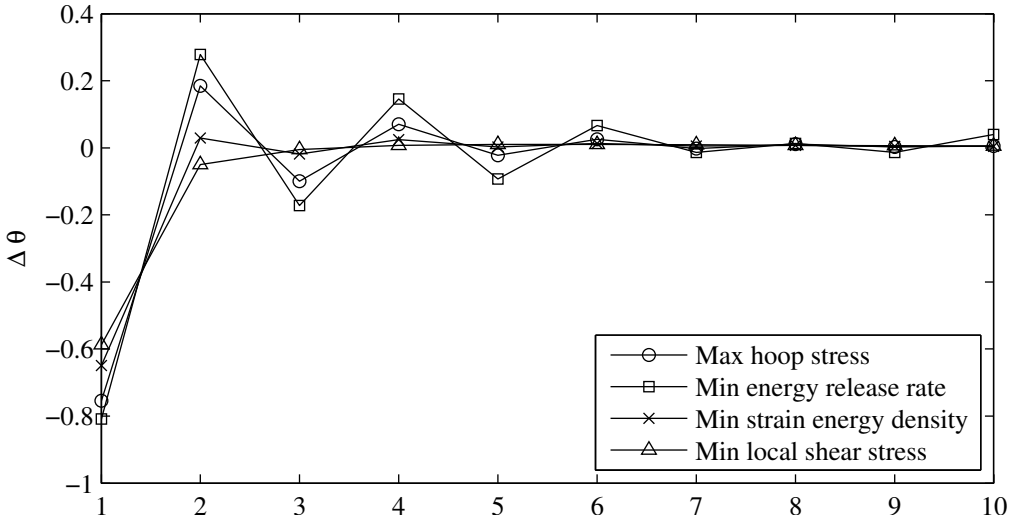

Figure 4.7: Crack initiation angle comparison

Propagation of an inclined crack induced by internal fracturing fluid flow

Consider an inclined crack under tensile as shown in Fig. 4.8. The crack is subjected to in-situ stress σ_{yy} and σ_{xx} and opened by internal fluid flow.

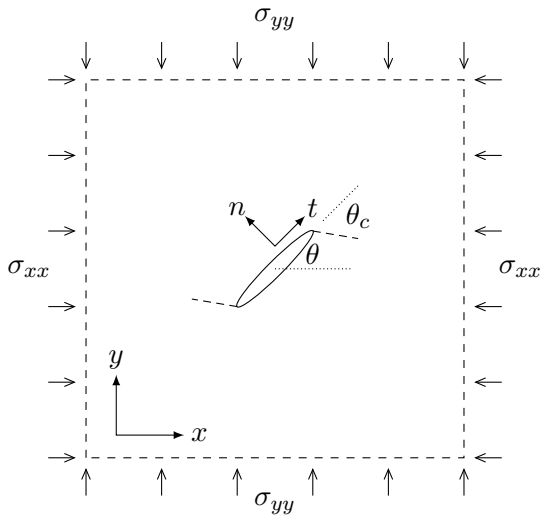

Figure 4.8: Inclined crack with internal fluid flow

The discretization of fluid flow equations in *Grid II* for implicit solution gives a system of nonlinear equations $r_i(w) = 0$ for elements $1 \leq i \leq n$

$$r_i = w_i - \lambda \left[w_{i+1}^{2n'+1} \left(p_{i+1} - p_i \right) \right]^{\frac{1}{n'}} + \lambda \left[w_i^{2n'+1} \left(p_i - p_{i-1} \right) \right]^{\frac{1}{n'}} - w_i^0, \quad \text{for } 2 \leq i \leq \frac{n}{2} - 1 \tag{4.62a}$$

$$r_i = w_i - \lambda \left[w_i^{2n'+1} \left(p_{i+1} - p_i \right) \right]^{\frac{1}{n'}} + \lambda \left[w_{i-1}^{2n'+1} \left(p_i - p_{i-1} \right) \right]^{\frac{1}{n'}} - w_i^0, \quad \text{for } \frac{n}{2} + 2 \leq i \leq n - 1 \tag{4.62b}$$

$$r_1 = w_1 - \lambda \left[w_2^{2n'+1} \left(p_2 - p_1 \right) \right]^{\frac{1}{n'}} - w_1^0 \tag{4.62c}$$

$$r_n = w_n + \lambda \left[w_{n-1}^{2n'+1} \left(p_n - p_{n-1} \right) \right]^{\frac{1}{n'}} - w_n^0 \tag{4.62d}$$

$$r_{\frac{n}{2}} = w_{\frac{n}{2}} + \lambda \left[w_{\frac{n}{2}}^{2n'+1} \left(p_{\frac{n}{2}} - p_{\frac{n}{2}-1} \right) \right]^{\frac{1}{n'}} - w_{\text{inj}} - w_{\frac{n}{2}}^0 \tag{4.62e}$$

$$r_{\frac{n}{2}+1} = w_{\frac{n}{2}+1} - \lambda \left[w_{\frac{n}{2}+1}^{2n'+1} \left(p_{\frac{n}{2}+2} - p_{\frac{n}{2}+1} \right) \right]^{\frac{1}{n'}} - w_{\text{inj}} - w_{\frac{n}{2}+1}^0 \tag{4.62f}$$

where

$$w_{\text{inj}} = \frac{\Delta t}{\Delta x} \frac{q_I}{2}$$

$$\lambda = \frac{n' \Delta t}{\Delta x (2 + 4n') (2K' \Delta x)^{\frac{1}{n'}}}$$

and the pressure p is provided from the displacement discontinuity equation in Eq. (4.30) given by

$$p_i = \sum_{k=1}^{n} \left[A_{ik} w_k + B_{ik} \left(\sigma_t^{\text{situ}} \right)_k + \left(\sigma_n^{\text{situ}} \right)_k \right] \tag{4.63}$$

The matrices A and B are given by

$$A = K_{nn} - K_{nt} K_{tt}^{-1} K_{tn} \tag{4.64a}$$

$$B = K_{nt} K_{tt}^{-1} \tag{4.64b}$$

The components of the influence factor K_{ij}, the local stresses $(\sigma_t)_j$ and $(\sigma_n)_j$ are evaluated about local coordinate system by the procedure described in Section 4.1.1 and Section 4.1.2. The propagation of an inclined crack with internal fluid flow is solved by Newton iteration using the analytical Jacobian $\dfrac{\partial r_i}{\partial w_j}$ given in Appendix B.3 and the parameters summarized in Table 4.2.

Simulation parameters					
G	$= 1.0$ GPa	ν	$= 0.2$	K_{Ic}	$= 0.5$ MPa$\sqrt{\mathrm{m}}$
q	$= 0.05\ \ \mathrm{m}^2/\mathrm{s}$	n'	$= 0.5$	K'	$= 0.001\ \mathrm{Pa}\cdot\mathrm{s}^{n'}$
L_0	$= 25$m	$L_{\max}$	$= 200$m	Δx	$= 2.5$m
θ_0	$= \pi/6$	Δt	$= 0.2$s	σ_{yy}	$= -1.0$ Mpa
σ_{xx}	$= 1.05\ \sigma_{yy}$				

Table 4.2: Simulation parameters (inclined crack with internal fluid flow)

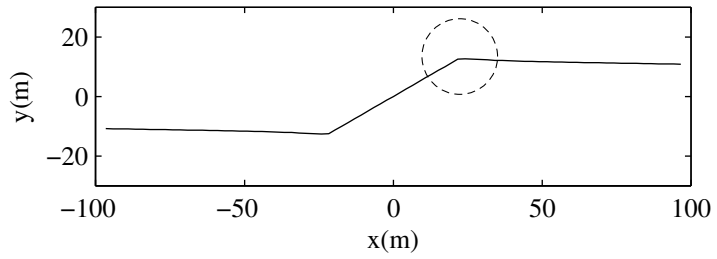

Figure 4.9: Crack path prediction based on crack propagation criteria

The path of an inclined crack propagation driven by internal fluid flow is given in Fig. 4.9. The detailed paths of criteria are described in Fig. 4.10 and Fig. 4.11. The minimum local shear stress provides the most desirable result which is smooth and less scattered in initiation angle.

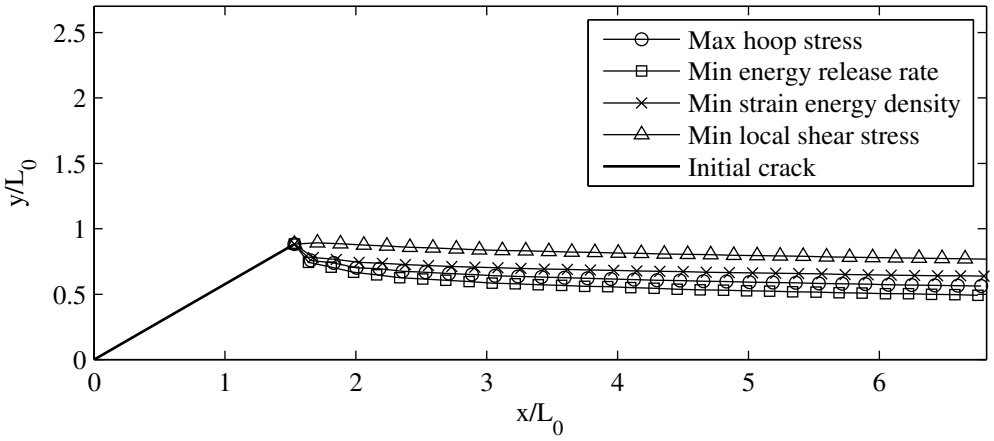

Figure 4.10: Crack path comparison

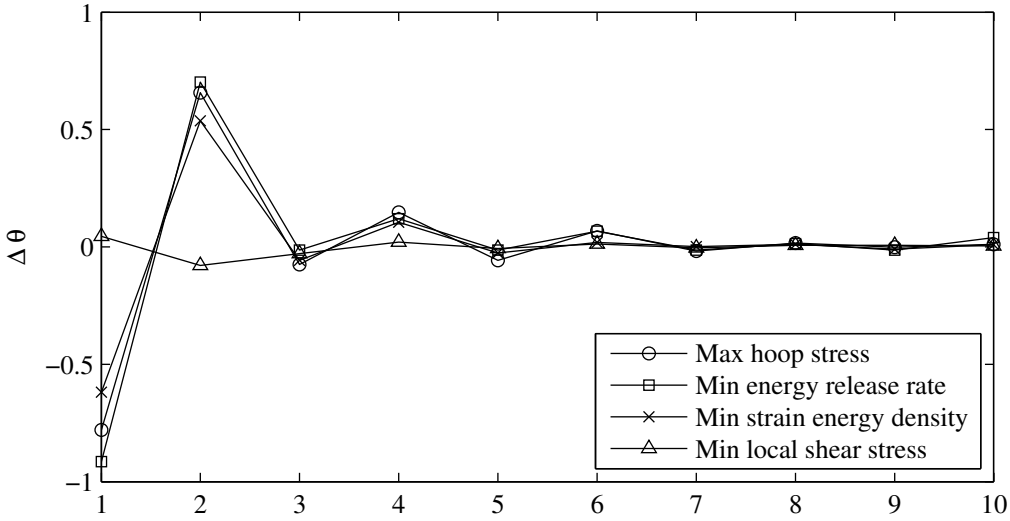

Figure 4.11: Crack initiation angle comparison

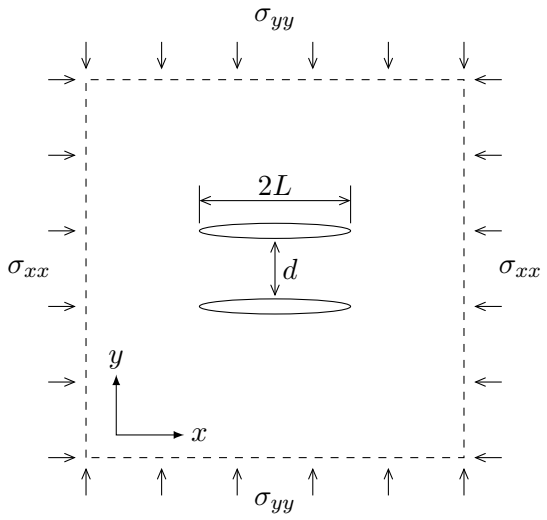

Figure 4.12: Parallel cracks with internal fluid flow

4.3 Propagation of parallel cracks

Consider a pair of parallel cracks subjected to in-situ stress σ_{xx} and σ_{yy} as shown in Fig. 4.12. They have equal length and the space between cracks is given by d. Both cracks will be opened by injecting a fluid at the center of each crack. The volume injection rate q_I for both cracks are kept constant. When the crack start opening, the displacement discontinuity in one crack affect to the other. The interaction between two cracks and its effect on the propagation are described.

The displacement discontinuity method gives the stress - displacement relationship of *Crack a* and *Crack b* given by

$$K_{tt}u_t + K_{tn}u_n = P_t = \sigma_t^{\text{situ}} \tag{4.65a}$$

$$K_{nt}u_t + K_{nn}u_n = P_n = p_f - \sigma_n^{\text{situ}} \tag{4.65b}$$

where u_t and u_n are the combined local shear and normal displacements of *Crack a* and *Crack b*. Also, the net pressure P_n and P_t, stresses σ_t and σ_n of both cracks are evaluated

about its local coordinates and combined. The influence matrix K_{ij} are obtained from Eq. (4.23) and procedure described in Section 4.1.1 and Section 4.1.2.

From Eq. (4.65), shear displacement u_t can be expressed in terms of normal displacement u_n

$$u_t = K_{tt}^{-1}\left(\sigma_t^{\text{situ}} - K_{tn}u_n\right) \tag{4.66}$$

Then the fluid pressure p_f can be found by

$$p_f = \left(K_{nn} - K_{nt}K_{tt}^{-1}K_{tn}\right)u_n + K_{nt}K_{tt}^{-1}\sigma_t^{\text{situ}} + \sigma_n^{\text{situ}} \tag{4.67}$$

The fluid flow equations are discretized in *Grid II* for implicit solution and this provides a system of nonlinear equations $r_i(w) = 0$ for elements $1 \le i \le 2n$

for $2 \le i \le \dfrac{n}{2} - 1$, $n + 2 \le i \le \dfrac{3n}{2} - 1$

$$r_i = w_i - \lambda\left[w_{i+1}^{2n'+1}\left(p_{i+1} - p_i\right)\right]^{\frac{1}{n'}} + \lambda\left[w_i^{2n'+1}\left(p_i - p_{i-1}\right)\right]^{\frac{1}{n'}} - w_i^0 \tag{4.68a}$$

for $\dfrac{n}{2} + 2 \le i \le n - 1$, $\dfrac{3n}{2} + 2 \le i \le 2n - 1$

$$r_i = w_i - \lambda\left[w_i^{2n'+1}\left(p_{i+1} - p_i\right)\right]^{\frac{1}{n'}} + \lambda\left[w_{i-1}^{2n'+1}\left(p_i - p_{i-1}\right)\right]^{\frac{1}{n'}} - w_i^0 \tag{4.68b}$$

for $i = 1, n + 1$

$$r_i = w_i - \lambda\left[w_{i+1}^{2n'+1}\left(p_{i+1} - p_i\right)\right]^{\frac{1}{n'}} - w_i^0 \tag{4.68c}$$

for $i = n, 2n$

$$r_i = w_i + \lambda\left[w_{i-1}^{2n'+1}\left(p_i - p_{i-1}\right)\right]^{\frac{1}{n'}} - w_i^0 \tag{4.68d}$$

for $i = \dfrac{n}{2}, \dfrac{3n}{2}$

$$r_i = w_i + \lambda\left[w_i^{2n'+1}\left(p_i - p_{i-1}\right)\right]^{\frac{1}{n'}} - w_{\text{inj}} - w_i^0 \tag{4.68e}$$

for $i = \dfrac{n}{2}+1, \dfrac{3n}{2}+1$

$$r_i = w_i - \lambda \left[w_i^{2n'+1} \left(p_{i+1} - p_i \right) \right]^{\frac{1}{n'}} - w_{\mathrm{inj}} - w_i^0 \tag{4.68f}$$

where

$$\lambda = \frac{n' \Delta t}{\Delta x (2+4n')(2K' \Delta x)^{\frac{1}{n'}}}$$

$$w_{\mathrm{inj}} = \frac{\Delta t}{\Delta x} \frac{q_I}{2}$$

The pressure p is provided from Eq. (4.67).

$$p_i = \sum_{k=1}^{2n} \left[A_{ik} w_k + B_{ik} \left(\sigma_t^{\mathrm{situ}} \right)_k + \left(\sigma_n^{\mathrm{situ}} \right)_k \right] \tag{4.69}$$

The matrices A and B are given by

$$A = K_{nn} - K_{nt} K_{tt}^{-1} K_{tn} \tag{4.70a}$$

$$B = K_{nt} K_{tt}^{-1} \tag{4.70b}$$

Above nonlinear equations are solved by Newton iteration using the analytical Jacobian $\dfrac{\partial r_i}{\partial w_j}$ given in Appendix B.4 and the parameters summarized in Table 4.3

Simulation parameters					
G	$= 1.0$ GPa	ν	$= 0.2$	K_{Ic}	$= 0.5$ MPa$\sqrt{\mathrm{m}}$
q	$= 0.01 \leq q \leq 0.11$ m^2/s	n'	$= 0.25 \leq n' \leq 1.0$	K'	$= 0.001$ Pa $\cdot$ s$^{n'}$
L_0	$= 25$m	$L_{\max}$	$= 2000$m	Δx	$= 5$m
d	$= 20 < d < 50$m	Δt	$= 1$s	σ_{yy}	$= -1$ MPa
σ_{xx}	$= 1.05\ \sigma_{yy}$	$2n_0$	$= 20$	$2n_{\max}$	$= 1600$

Table 4.3: Simulation parameters (parallel cracks with internal fluid flow)

The propagation path of a pair of parallel cracks having gap distance 20m is shown in Fig. 4.13. Each end of cracks is displaced approximately by 91m when the length of crack path reaches to 2000m and it is about 4.6% of L. The criteria based on minimum local

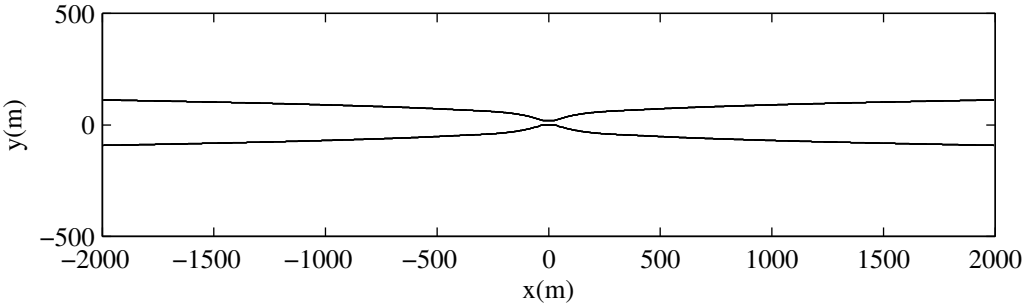

Figure 4.13: Path prediction of parallel cracks

shear stress shows a good prediction as shwon in Fig. 4.14. Several relations between the

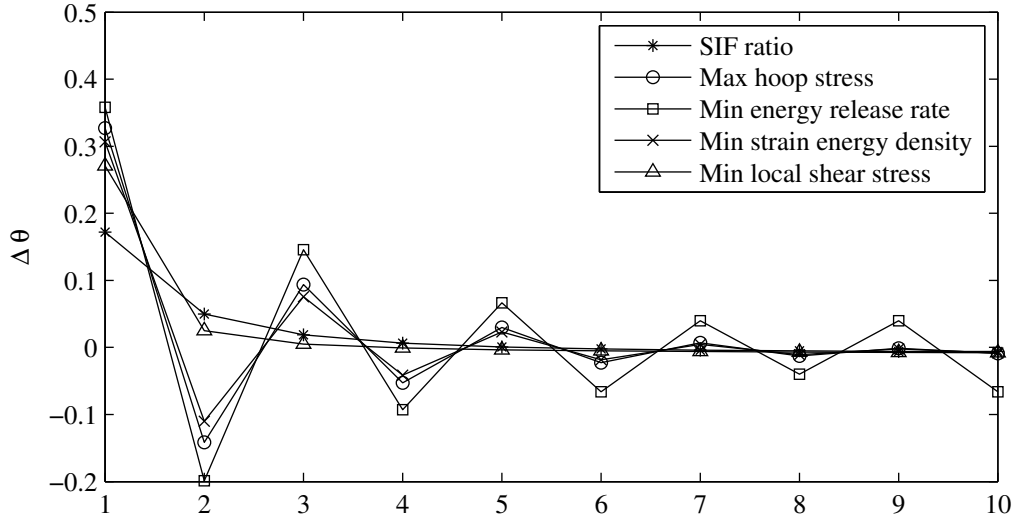

Figure 4.14: Crack initiation angle comparison

displacement of crack path from the original path are compared in Fig. 4.15, Fig. 4.16 and Fig. 4.17. The displacement are not much affected by the initial gap distance, but it is highly related with the power-law index n' and the volume flow rate q. The gap distance

increases with increasing n' and q. This result is caused by the difference in crack width w. As shown in Fig. 4.18, the higher power-law index n' produce larger crack widths both in normal ans shear. The stress caused by larger crack width affect the interaction between two cracks more than the one created by a lower n'. The change in normal and shear stress due to the growth of parallel cracks are provided in Fig. 4.19 and Fig. 4.20.

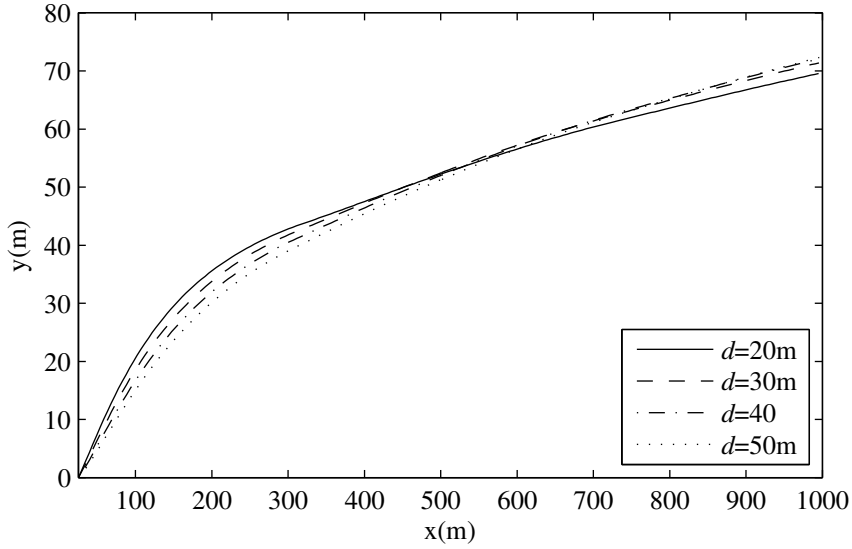

Figure 4.15: Displacement - initial gap distance

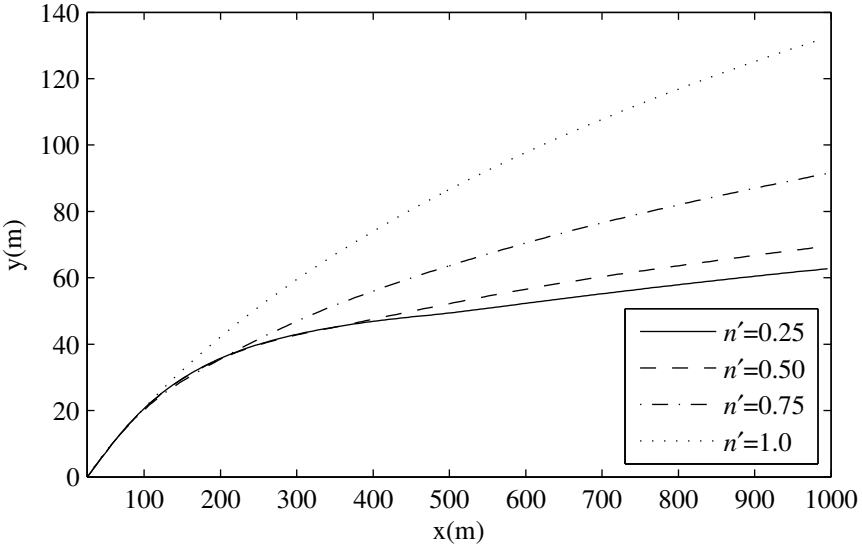

Figure 4.16: Displacement - power-law index

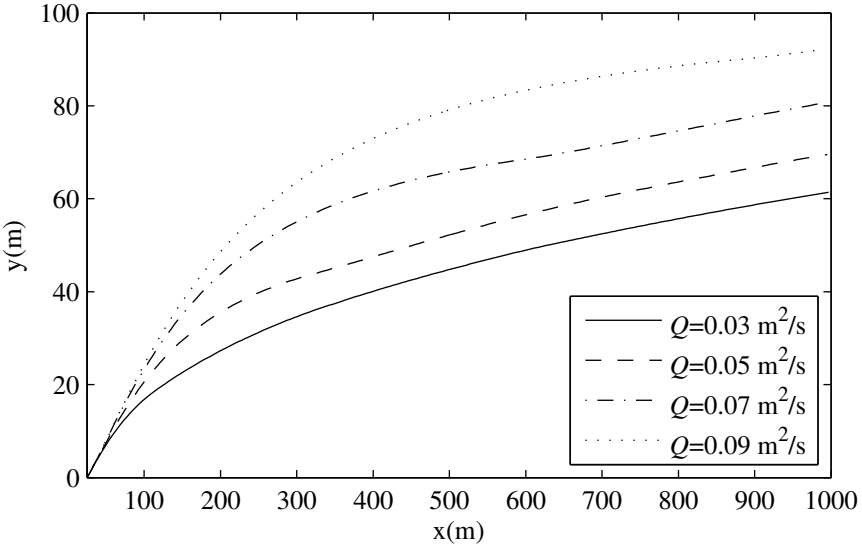

Figure 4.17: Displacement - flow rate

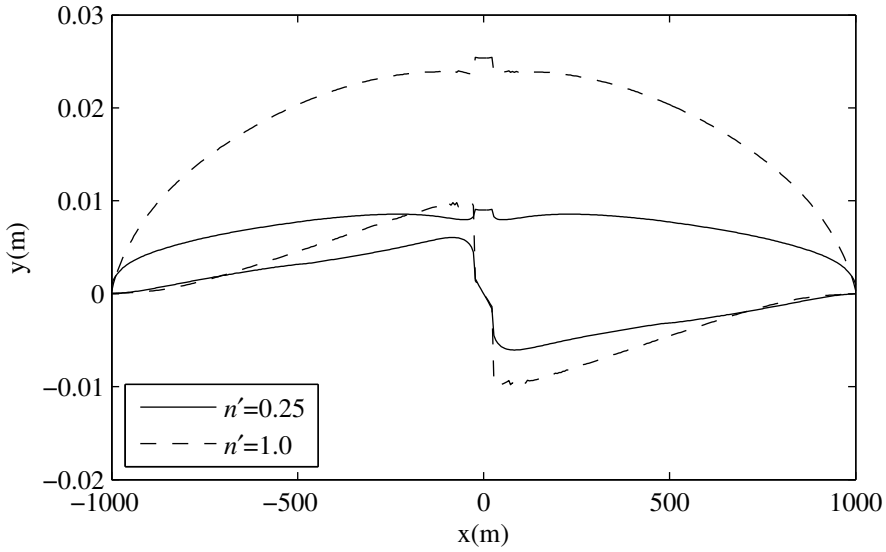

Figure 4.18: Displacement profile

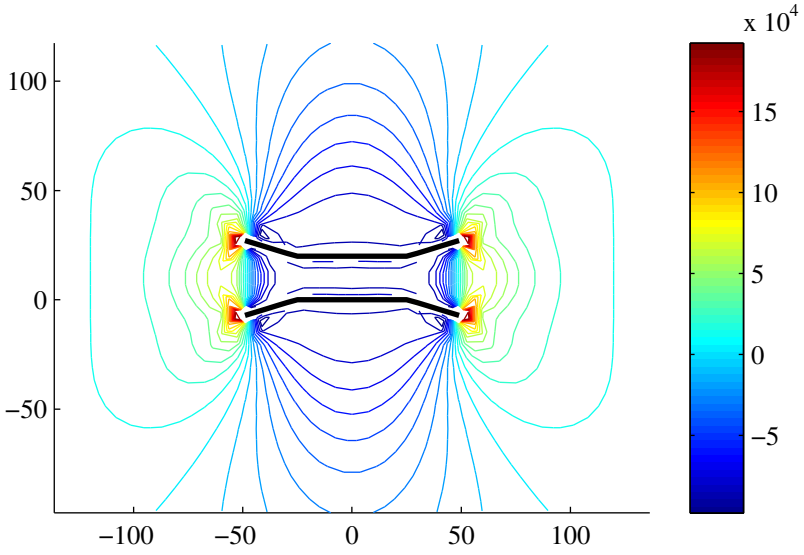

Figure 4.19: Change in stress field (σ_{yy})

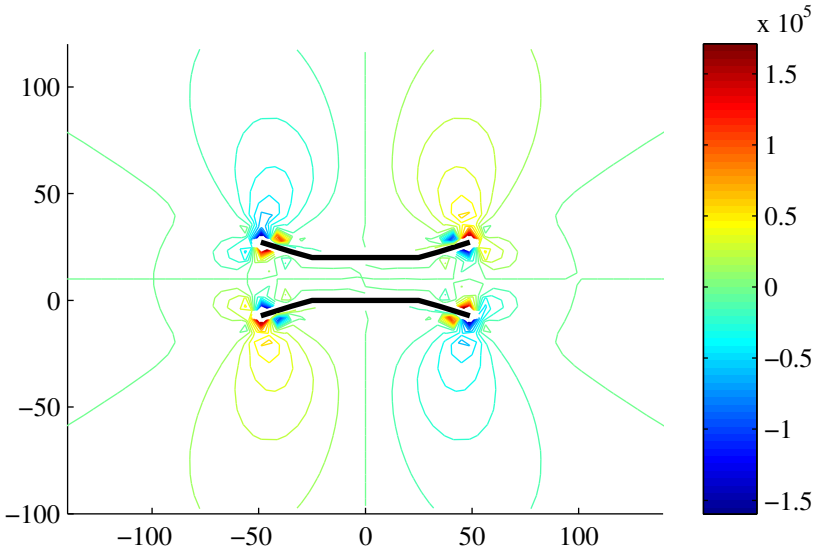

Figure 4.20: Change in stress field (σ_{xy})

Chapter 5

Conclusions and ongoing works

Concluding remarks

An efficient highly nonlinear numerical model of crack propagation driven by internal fluid flow is developed using displacement discontinuity boundary element method and finite difference method. The elasticity problem in solid is modeled with displacement discontinuity method and the fluid flow is by finite difference method. The solution of coupled field problem of solid-fluid interaction is obtained by matching the stresses along the surface of opening crack under tensile with the pressure gradient created by the fluid flow inside channel. Use of boundary element method allow the crack system has less elements compare to the conventional methods such as finite element method and finite difference method. And this leads the elasticity model to have more improved efficiency. The internal fluid flow is discretized by both explicit and implicit finite difference schemes. The results of both schemes successfully solve the problem, but the implicit scheme showed better performance in speed and robustness because the explicit scheme has a limitation on selecting time step

restricted by Courant–Friedrichs–Lewy (CFL) condition or von Newmann condition. The dual grid system which allowing an additional grid for fluid flow improved volume accuracy and utilization of special crack tip element helps us to reduce the numerical error on stresses and displacements near the crack tip region.

The system of nonlinear equations in implicit scheme is solved by Newton iteration trust-region and quasi-Newton Broyden's method. By implementing the line search method of Wolfe and backtracking, the performance of iterative solver is improved and the stability issue when the system faces ill-conditioned Jacobian matrix is overcomed with the singular value decomposition, Levenberg-Marquardt method and modified Cholesky factorization. The quasi-Newton method shows the remarkable speed when the fluid is close to Newtonian fluid, but is unstable when the power-law index is lower than 0.5. The Newton iteration with line search provides a good accuracy and efficiency overall in wide range of power-law index n'. The trust-region method combined with line search is a little slower than Newton iteration, but it gives more robust results in various conditions controlled by simulation parameters.

The prediction of crack path under mixed loading condition is presented and studied with existing criteria, such as stress intensity factor ratio, maximum circumferential tensile stress, minimum strain energy density, maximum strain energy release rate and a new proposed numerical approach for crack initiation criterion, minimum local shear stress criterion. The new criterion gives the most stable results and smoother path of hydraulically driven crack propagation among the given criteria.

The growth of two parallel cracks case is simulated and analyzed using the numerical solutions discussed so far. The interaction between two cracks and effect of in-situ stress are

well implemented. The crack path prediction shows that the distance between cracks are rapidly increase when cracks start growing, but eventually have stable strait path along the direction that the effect of interaction is minimized. It also shows that the displaced distance of crack path from their original path is controlled by a fluid power-law index n' and a volume flow rate q. This results provides some useful inputs for optimal design of multiple stage and multiple fracturing treatments along horizontal wells currently adopted by the oil and gas industry.

The numerical model we developed for crack propagation driven by internal fluid flow will provide useful information in the design process of hydraulic fracturing process is designed in site. With the given conditions of rock formation the model will be used for determining the expected fracture geometry and resources required to create desired fracture such as selection of fracturing fluid, pump pressure, injection time, amount of fluid and etc. Also, the safe distance from the unwanted area and optimized crack spacing for maximum production can be obtained form the multiple crack propagation model.

Ongoing works and challenges

The crack propagation model is developed based on elasticity, linear elastic fracture mechanics and fluid dynamics theory, but the real situation in field is more complicated. The goal of this project, developing a numerical model for hydraulic fracturing, is to make our model as close as possible to real situation in field. To achieve this goal following are must be considered and implemented to the numerical model of crack propagation driven by internal fluid flow.

Fluid leak off The permeability of rock we targeted is very small, but still porous. Therefore, there is a volume leak-off to rock formation. The one-dimensional leak-off model is proposed by Carter in 1960s and still used in literatures nowadays. The Carter's leak-off model can be improved by coupling the fluid flow inside crack with the porous media flow of non-Newtonian fluid theory. For plain strain model, this can be solved by two dimensional finite element model near cracked area and matching this with the fluid flow model discretized in finite difference scheme.

Poro-elasticity When there is a fluid leak-off in rock formation, some of leaked volume will be stored in pores of rock. This leads the elastic properties of rock to be changed and affect the crack geometry.

Temperature effect Generally, the temperature underground increases approximately 25 °C per kilometer. Therefore, the hydraulic fracture process will face the complexity caused by existing vertical temperature gradient. If temperature sensitive fluid is used, its properties will be changed and the difference in temperature between the fluid and rock formation in depth will create a thermal stress in rock. Thus, the temperature effect on fluid properties and the thermal stress must be included in the model.

Proppant transport The proppant is a sand-like material transported by fluid to the fracture. Then, the crack is filled with proppants and keep opened during the production after the fluid pressure is removed. The properties of a fracturing fluid is changed due to the concentration of proppant.

Filter cake The fracturing fluid usually includes natural polymers and these polymers are built up on the surfaces of well bore and crack during the hydraulic fracturing process. This filter cake lower the permeability of the wall and reduces the rate of fluid volume leak-off to rock formation.

Layered formation and material anisotropy The current model assumes that crack is in an isotropic and homogeneous medium. But, crack can be created in an anisotropic medium or in layered structure with the different material properties. In this case, the elasticity equation modeled with displacement discontinuity method should be modified to handle stiffness tensor and multiple materials.

Bibliography

[1] B. Brady, J. Elbel, M. Mack, H. Morales, K. Nolte, and B. Poe, "Cracking rock: progress in fracture treatment design," *Oilfield Review*, vol. 4, no. 4, pp. 4–17, 1992.

[2] M. Economides, K. Nolte, and U. Ahmed, *Reservoir stimulation*, vol. 2. Prentice Hall, 1989.

[3] J. L. Gidley, "Recent advances in hydraulic fracturing," 1989.

[4] C. Montgomery and M. Smith, "Hydraulic fracturing: History of an enduring technology," *Journal of Petroleum Technology*, vol. 62, no. 12, p. 26, 2010.

[5] D. Hill, E. Neme, C. Ehlig-Economides, and M. Mollinedo, "Reentry drilling gives new life to aging fields," *Technology*, vol. 34, no. 9, pp. 25–33, 1995.

[6] L. Helms, "Horizontal drilling," *DMR Newsletter*, vol. 35, no. 1, 2008.

[7] E. Fjaer, *Petroleum related rock mechanics*. Elsevier Science, 2008.

[8] U. S. E. P. Agency, "Hydraulic fracturing white paper," 2004.

[9] I. Sneddon and H. Elliot, "The opening of a griffith crack under internal pressure," *Quart. Appl. Math*, vol. 4, no. 3, pp. 262–267, 1946.

[10] T. Perkins and L. Kern, "Widths of hydraulic fractures," *Journal of Petroleum Technology*, vol. 13, no. 9, pp. 937–949, 1961.

[11] R. Nordgren, "Propagation of a vertical hydraulic fracture," *Old SPE Journal*, vol. 12, no. 4, pp. 306–314, 1972.

[12] S. Khristianovic and Y. Zheltov, "Formation of vertical fractures by means of highly viscous fluids," in *Proceedings of the 4th World Petroleum Congress, Rome*, vol. 2, pp. 579–586, 1955.

[13] J. Geertsma and F. De Klerk, "A rapid method of predicting width and extent of hydraulically induced fractures," *Journal of Petroleum Technology*, vol. 21, no. 12, pp. 1571–1581, 1969.

[14] A. Daneshy, "On the design of vertical hydraulic fractures," *Journal of Petroleum Technology*, vol. 25, no. 1, pp. 83–97, 1973.

[15] J. Geertsma, "Two-dimensional fracture-propagation models," *Recent Advances in Hydraulic Fracturing*, vol. 12, pp. 81–94, 1989.

[16] C. Yew, *Mechanics of hydraulic fracturing*. Gulf Professional Publishing, 1997.

[17] C. Wright, L. Weijers, E. Davis, and M. Mayerhofer, "Understanding hydraulic fracture growth: Tricky but not hopeless," in *SPE Annual Technical Conference and Exhibition*, 1999.

[18] E. Detournay, "Propagation regimes of fluid-driven fractures in impermeable rocks," *International Journal of Geomechanics*, vol. 4, no. 1, pp. 35–45, 2004.

[19] R. Clifton and A. Abou-Sayed, "A variational approach to the prediction of the three-dimensional geometry of hydraulic fractures," in *SPE/DOE Low Permeability Gas Reservoirs Symposium*, 1981.

[20] R. Clifton and A. Abou-Sayed, "On the computation of the three-dimensional geometry of hydraulic fractures," in *Symposium on Low Permeability Gas Reservoirs*, 1979.

[21] R. Clifton, "Three-dimensional fracture-propagation models," *Recent Advances in Hydraulic Fracturing–SPE Monographs*, vol. 12, pp. 95–108, 1989.

[22] G. Blandford, A. Ingraffea, and J. Liggett, "Two-dimensional stress intensity factor computations using the boundary element method," *International Journal for Numerical Methods in Engineering*, vol. 17, pp. 387–404, 1981.

[23] M. Biot, L. Masse, and W. Medlin, "A two-dimensional theory of fracture propagation," *SPE Production Engineering*, vol. 1, no. 1, pp. 17–30, 1986.

[24] J. Adachi and E. Detournay, "Self-similar solution of a plane-strain fracture driven by a power-law fluid," *International Journal for Numerical and Analytical Methods in Geomechanics*, vol. 26, no. 6, pp. 579–604, 2002.

[25] E. Siebrits and A. P. Peirce, "An efficient multi-layer planar 3d fracture growth algorithm using a fixed mesh approach," *International journal for numerical methods in engineering*, vol. 53, no. 3, pp. 691–717, 2002.

[26] J. Adachi, E. Siebrits, A. Peirce, and J. Desroches, "Computer simulation of hydraulic fractures," *International Journal of Rock Mechanics and Mining Sciences*, vol. 44, no. 5, pp. 739–757, 2007.

[27] S. Advani, T. Lee, and J. Lee, "Three-dimensional modeling of hydraulic fractures in layered media. i, finite element formulations," *Journal of energy resources technology*, vol. 112, no. 1, pp. 1–9, 1990.

[28] R. Barree, "A practical numerical simulator for three-dimensional fracture propagation in heterogeneous media," in *SPE Reservoir Simulation Symposium*, 1983.

[29] B. Carter, J. Desroches, A. Ingraffea, and P. Wawrzynek, "Simulating fully 3d hydraulic fracturing," *Modeling in geomechanics*, pp. 525–557, 2000.

[30] R. J. Clifton and J.-J. J. Wang, "Adaptive optimal mesh generator for hydraulic fracturing modeling," in *The 32nd US Symposium on Rock Mechanics (USRMS)*, 1991.

[31] K. Naceur, M. Thiercelin, and E. Touboul, "Simulation of fluid flow in hydraulic fracturing: implications for 3d propagation," *SPE Production Engineering*, vol. 5, no. 2, pp. 133–141, 1990.

[32] L. Vandamme and J. Curran, "A three-dimensional hydraulic fracturing simulator," *International journal for numerical methods in engineering*, vol. 28, no. 4, pp. 909–927, 2005.

[33] S. Timoshenko and J. Goodier, *Theory of Elasticity, McGraw-Hill, New York*. Springer, 1970.

[34] R. Asaro and V. Lubarda, *Mechanics of solids and materials*. Cambridge University Press, 2006.

[35] I. N. Sneddon, *Fourier transforms*, vol. 27. McGraw-Hill, 1951.

[36] S. Crouch, "Solution of plane elasticity problems by the displacement discontinuity method. i. infinite body solution," *International journal for numerical methods in engineering*, vol. 10, no. 2, pp. 301–343, 1976.

[37] S. L. Crouch and A. M. Starfield, *Boundary element methods in solid mechanics*. 9 Winchester Terrace, Winchester, MA 01890, USA: Allen & Unwin, Inc., 1983.

[38] T. L. Anderson, *Fracture mechanics: fundamentals and applications*. CRC, 2005.

[39] E. Gdoutos, *Fracture mechanics: an introduction*, vol. 123. Springer, 2005.

[40] G. Sih, "Some basic problems in fracture mechanics and new concepts," *Engineering Fracture Mechanics*, vol. 5, no. 2, pp. 365–377, 1973.

[41] G. Sih, "Energy-density concept in fracture mechanics," *Engineering Fracture Mechanics*, vol. 5, no. 4, pp. 1037–1040, 1973.

[42] G. C. Sih, "Strain-energy-density factor applied to mixed mode crack problems," *International Journal of Fracture*, vol. 10, no. 3, pp. 305–321, 1974.

[43] R. Clifton and A. Abou-Sayed, "On the mechanics of hydraulic fracturing," in *Proceedings of the 9th US National Congress of Applied Mechanics*, pp. 443–451, 1982.

[44] A. Peirce and E. Siebrits, "A dual mesh multigrid preconditioner for the efficient solution of hydraulically driven fracture problems," *International journal for numerical methods in engineering*, vol. 63, no. 13, pp. 1797–1823, 2005.

[45] J. Nocedal and S. Wright, *Numerical optimization*. Springer verlag, 1999.

[46] P. A. Ramachandran, "Method of fundamental solutions: singular value decomposition analysis," *Communications in numerical methods in engineering*, vol. 18, no. 11, pp. 789–801, 2002.

[47] D. W. Marquardt, "An algorithm for least-squares estimation of nonlinear parameters," *Journal of the Society for Industrial & Applied Mathematics*, vol. 11, no. 2, pp. 431–441, 1963.

[48] C. Kelley, *Iterative Methods for Linear and Nonlinear Equations*. Society for Industrial and Applied Mathematics, 1995.

[49] C. Kelley, *Iterative Methods for Optimization*. Society for Industrial and Applied Mathematics, 1999.

[50] W. Sun and Y. Yuan, *Optimization theory and methods: nonlinear programming*, vol. 1. springer, 2006.

[51] W. H. Press, S. A. Teukolsky, W. T. Vetterling, and B. P. Flannery, *Numerical recipes 3rd edition: The art of scientific computing*. Cambridge University Press, 2007.

[52] J. Wang and R. Clifton, "Application of a quasi-newton method in 3d hydraulic fracturing simulations," in *Proceedings of 8th International Conference of the Association for Computer Methods and Advances in Geomechanics*, 1994.

[53] S. Boyd and L. Vandenberghe, *Convex optimization*. Cambridge university press, 2004.

[54] Y. Yuan, "A review of trust region algorithms for optimization," in *ICM99: Proceedings of the Fourth International Congress on Industrial and Applied Mathematics* (J. Ball and e. JCR Hunt, eds.), pp. 271–282, Oxford University Press, Oxford, 2000.

[55] J. Nocedal and Y.-x. Yuan, "Combining trust region and line search techniques," *Advances in Nonlinear Programming*, vol. 14, p. 153, 1998.

[56] I. S. Sokolnikoff and R. D. Specht, *Mathematical theory of elasticity*, vol. 83. McGraw-Hill New York, 1956.

[57] J. Dundurs, "Elastic interaction of dislocations with inhomogeneities," *Mathematical Theory of Dislocations*, pp. 70–115, 1969.

[58] D. A. Hills, P. Kelly, D. Dai, and A. Korsunsky, *Solution of crack problems: the distributed dislocation technique*, vol. 44. Springer, 1996.

[59] J. Weertman, *Dislocation based fracture mechanics*. World Scientific Publishing Company Incorporated, 1996.

[60] F. Erdogan and G. Sih, "On the crack extension in plates under plane loading and transverse shear," *Journal of basic engineering*, vol. 85, p. 519, 1963.

[61] D. Broek, *Elementary engineering fracture mechanics*. Springer, 1982.

[62] M. Hussain, S. Pu, and J. Underwood, "Strain energy release rate for a crack under combined mode i and mode," *Fracture analysis*, vol. 560, p. 1, 1974.

Appendix A

Plane crack in a tensile field

The stress field for dislocation can be determined from the Flamant's solution. By choosing the terms that give stresses proportional to r^{-1} from the stress component table of the Michell solution, we obtain the stress function given in the Flament's solution:

$$\phi = C_1 r\theta \sin\theta + C_2 r\theta \cos\theta + C_3 r \ln r \cos\theta + C_4 r \ln r \sin\theta \tag{A.1}$$

Due to the symmetry of the problem, the terms in Eq. (A.1) are restricted only to the symmetric terms about $\theta = 0$, which equivalent to the Kelvin's solution.

$$\phi = C_1 r\theta \sin\theta + C_3 r \ln r \cos\theta \tag{A.2}$$

Then, the stress components are:

$$\sigma_{rr} = \frac{2C_1 \cos\theta}{r} + \frac{C_3 \cos\theta}{r} \tag{A.3a}$$

$$\sigma_{r\theta} = \frac{C_3 \sin\theta}{r} \tag{A.3b}$$

$$\sigma_{\theta\theta} = \frac{C_3 \cos\theta}{r} \tag{A.3c}$$

and the displacement components are

$$2Gu_r = \frac{C_1}{2}\left[(\kappa-1)\theta\sin\theta - \cos\theta + (\kappa+1)\ln r\cos\theta\right] + \frac{C_3}{2}\left[(\kappa+1)\theta\sin\theta - \cos\theta + (\kappa-1)\ln r\cos\theta\right] \tag{A.4a}$$

$$2Gu_\theta = \frac{C_1}{2}\left[(\kappa-1)\theta\cos\theta - \sin\theta - (\kappa+1)\ln r\sin\theta\right] + \frac{C_3}{2}\left[(\kappa+1)\theta\cos\theta - \sin\theta - (\kappa-1)\ln r\sin\theta\right] \tag{A.4b}$$

where G is the shear modulus and κ is the Kolosov's constant given by

$$\kappa = 3 - 4\nu, \quad \text{for plane strain} \tag{A.5a}$$

$$\kappa = \frac{3-\nu}{1+\nu}, \quad \text{for plane stress} \tag{A.5b}$$

Consider the equilibrium of a small circle of radius r surrounding the origin and assuming that there be no net force at the origin,

$$\int_0^{2\pi} (\sigma_{rr}\cos\theta - \sigma_{r\theta}\sin\theta)\, r d\theta = 0 \tag{A.6}$$

by substituting Eq. (A.3a) into Eq. (A.6), we have $C_1 = 0$. Therefore we can obtain the stress function for the dislocation solution from Eq. (A.2) with $C_1 = 0$.

$$\phi = C_3 r\ln r\cos\theta \tag{A.7}$$

And the corresponding stress and displacement components are:

$$\sigma_{rr} = \sigma_{\theta\theta} = \frac{C_3\cos\theta}{r} \tag{A.8a}$$

$$\sigma_{r\theta} = \frac{C_3\sin\theta}{r} \tag{A.8b}$$

$$2Gu_r = \frac{C_3}{2}\left[(\kappa+1)\,\theta\sin\theta - \cos\theta + (\kappa-1)\ln r\cos\theta\right] \tag{A.9a}$$

$$2Gu_\theta = \frac{C_3}{2}\left[(\kappa+1)\,\theta\cos\theta - \sin\theta - (\kappa-1)\ln r\sin\theta\right] \tag{A.9b}$$

From Eq. (A.9b), the discontinuity in the displacement u_θ on $y = 0$ is

$$\delta = u_\theta(0) - u_\theta(2\pi) = -\frac{C_3\pi(\kappa+1)}{2G} \tag{A.10}$$

By defining a dislocation of strength u_y as one which opens a gap $\delta = u_y$ in plane strain motion, we can obtain C_3 in terms of u_y.

$$C_3 = -\frac{Gu_y}{2\pi(1-\nu)} \tag{A.11}$$

The stress field can be found by substituting Eq. (A.11) into Eq. (A.8a) and Eq. (A.8b).

$$\sigma_{rr} = \sigma_{\theta\theta} = -\frac{Gu_y \cos\theta}{2\pi(1-\nu)r} \tag{A.12a}$$

$$\sigma_{r\theta} = -\frac{Gu_y \sin\theta}{2\pi(1-\nu)r} \tag{A.12b}$$

The stress components at $y = 0$ are

$$\sigma_{xx} = \sigma_{yy} = -\frac{Gu_y}{2\pi(1-\nu)x} \tag{A.13a}$$

$$\sigma_{yx} = 0 \tag{A.13b}$$

The solution above is for a climb dislocations (mode I).

In case of glide dislocation (mode II), the solution can be obtained from the stress function

$$\phi = r \ln r \sin\theta \tag{A.14}$$

The stress field due to a glide dislocation is given by

$$\sigma_{rr} = \sigma_{\theta\theta} = \frac{G(1+\nu)u_x \sin\theta}{2\pi r} \tag{A.15a}$$

$$\sigma_{r\theta} = -\frac{G(1+\nu)u_x \cos\theta}{2\pi r} \tag{A.15b}$$

On the surface of $y = 0$, the stress components are reduced by

$$\sigma_{xx} = \sigma_{yy} = 0 \tag{A.16a}$$

$$\sigma_{yx} = \frac{G(1+\nu)u_x}{2\pi x} \tag{A.16b}$$

The dislocation u must satisfy the two closure conditions:

$$\int_{\Omega} u_x(x,y)dxdy = 0 \tag{A.17a}$$

$$\int_{\Omega} u_y(x,y)dxdy = 0 \tag{A.17b}$$

which means the total strength of the dislocations in Ω is zero.

The boundary conditions of the crack opening problem given in the Fig. 2.1 are:

$$\sigma_{yx} = \sigma_{yy} = 0, \qquad \text{on} \quad -L < x < L \text{ and } y = 0 \tag{A.18a}$$

$$\sigma_{yy} \to S, \sigma_{xy}, \sigma_{xx} \to 0 \qquad \text{at} \quad r \to \infty \tag{A.18b}$$

The solution can be represented as the sum of the stress field without a crack and a corrective solution for a crack.

first, the body without a crack is subjected to an uniform tension:

$$\sigma_{yy} = S \tag{A.19}$$

And the boundary conditions for the corrective solution are

$$\sigma_{yx} = 0, \quad \sigma_{yy} = -S \qquad \text{on} \quad -L < x < L \text{ and } y = 0 \tag{A.20a}$$

$$\sigma_{yy}, \sigma_{xy}, \sigma_{xx} \to 0 \qquad \text{at} \quad r \to \infty \tag{A.20b}$$

We assume that there is no tangential motion between the crack faces and only consider a distribution of $u_y(x)$ of dislocations per unit length in the range $-L < x < L$ and $y = 0$. The traction $\sigma_{yy}(x,0)$ due to the dislocation $u_y(\xi,0)$ can be expressed by modifying Eq. (A.13a).

$$\sigma_{yy} = -\frac{Gu_y(\xi)d\xi}{2\pi(1-\nu)(x-\xi)} \tag{A.21}$$

The traction due to the whole distribution of dislocations can be written by a integral form:

$$\sigma_{yy} = -\frac{G}{2\pi(1-\nu)} \int_{-L}^{+L} \frac{u_y(\xi)d\xi}{(x-\xi)} \tag{A.22}$$

With the boundary condition in Eq. (A.20), we can construct the Cauchy singular integral equation for $u_y(\xi)$.

$$\int_{-L}^{+L} \frac{u_y(\xi)d\xi}{(x-\xi)} = \frac{2\pi S(1-\nu)}{G}, \quad -L < x < L \tag{A.23}$$

Above equation can be solved by a simple solution based on the change of variable.

$$x = L\cos\phi, \quad \xi = L\cos\theta \tag{A.24}$$

Substituting Eq. (A.24) into Eq. (A.23), we obtain

$$\int_0^{\pi} \frac{u_y(\theta)\sin\theta d\theta}{(\cos\phi - \cos\theta)} = \frac{2\pi S(1-\nu)}{G}, \quad 0 < \phi < \pi \tag{A.25}$$

which can be simplified using the result:

$$\int_0^{\pi} \frac{\cos(n\theta)d\theta}{(\cos\phi - \cos\theta)} = -\frac{\pi\sin(n\phi)}{\sin\phi} \tag{A.26}$$

Then, expand $u_y(\theta)$ in a Fourier series

$$u_y(\theta) = \sum_{n=0}^{\infty} b_n \frac{\cos(n\theta)}{\sin\theta} \tag{A.27}$$

Substituting Eq. (A.27) into Eq. (A.25), we obtain

$$\sum_{n=0}^{\infty} \int_0^{\pi} \frac{b_n\cos(n\theta)d\theta}{(\cos\phi - \cos\theta)} = \frac{2\pi S(1-\nu)}{G} \tag{A.28}$$

Using Eq. (A.26), this becomes

$$-\sum_{n=0}^{\infty} b_n \frac{\sin(n\phi)}{\sin\phi} = \frac{2S(1-\nu)}{G} \tag{A.29}$$

With $n = 1$,

$$b_1 = -\frac{2S(1-\nu)}{G} \tag{A.30}$$

From Eq. (A.27) and Eq. (A.30),

$$u_y(\theta) = -\frac{2S(1-\nu)}{G}\frac{\cos\theta}{\sin\theta} + \frac{b_0}{\sin\theta} \tag{A.31}$$

Then, using Eq. (A.24) and Eq. (A.31),

$$u_y(\xi) = -\frac{2S(1-\nu)}{G}\frac{\xi}{\sqrt{L^2-\xi^2}} + \frac{Lb_0}{\sqrt{L^2-\xi^2}} \tag{A.32}$$

The unknown b_0 can be determined by applying the closure condition Eq. (A.17b) to Eq. (A.32).

$$\int_{-L}^{+L} u_y(\xi)d\xi = 0 \quad \Longrightarrow \quad b_0 = 0 \tag{A.33}$$

and

$$u_y(\xi) = -\frac{2S(1-\nu)}{G}\frac{\xi}{\sqrt{L^2-\xi^2}} \tag{A.34}$$

The stress field surrounding the crack tip in can be determined using Eq. (A.22) and Eq. (A.34),

$$\sigma_{yy} = \frac{S}{\pi}\int_{-L}^{+L}\frac{\xi d\xi}{(x-\xi)\sqrt{L^2-\xi^2}} = S\left(-1+\frac{|x|}{\sqrt{x^2-L^2}}\right), \qquad |x|>L, \quad y=0 \tag{A.35}$$

The complete stress field can be obtained by add uniform stress field in Eq. (A.19) to the above corrective solution.

$$\sigma_{yy} = \frac{S|x|}{\sqrt{x^2-L^2}}, \qquad |x|>L, \quad y=0 \tag{A.36}$$

Finally, the crack opening displacement is given by:

$$u_y(x,0^+) - u_y(x,0^-) = \int_{-L}^{x} u_y(\xi)d\xi = \frac{2S(1-\nu)}{G}\sqrt{L^2-x^2} \tag{A.37}$$

Appendix B

Analytical Jacobian matrices

B.1 For right half-crack in *Grid I*

for $3 \leq i \leq n-2$

$$\begin{aligned} J_{i,j} =& \delta_{ij} - \frac{\lambda_I}{n'}\left[(w_{i+1})^{2n'+1}(p_{i+2}-p_i)\right]^{\frac{1}{n'}-1}(w_{i+1})^{2n'+1}(A_{i+2,j}-A_{i,j}) \\ &+ \frac{\lambda_I}{n'}\left[(w_{i-1})^{2n'+1}(p_i-p_{i-2})\right]^{\frac{1}{n'}-1}(w_{i-1})^{2n'+1}(A_{i,j}-A_{i-2,j}), \\ & \qquad\qquad\qquad\qquad\qquad\qquad\qquad\qquad\qquad\qquad j \neq i-1, i+1 \end{aligned} \tag{B.1a}$$

$$\begin{aligned} J_{i,i-1} =& -\frac{\lambda_I}{n'}\left[(w_{i+1})^{2n'+1}(p_{i+2}-p_i)\right]^{\frac{1}{n'}-1}(w_{i+1})^{2n'+1}(A_{i+2,i-1}-A_{i,i-1}) \\ &+ \frac{\lambda_I}{n'}\left[(w_{i-1})^{2n'+1}(p_i-p_{i-2})\right]^{\frac{1}{n'}-1}\Big[(2n'+1)(w_{i-1})^{2n'}(p_i-p_{i-2}) \\ & \qquad\qquad\qquad\qquad +(w_{i-1})^{2n'+1}(A_{i,i-1}-A_{i-2,i-1})\Big] \end{aligned} \tag{B.1b}$$

$$\begin{aligned} J_{i,i+1} =& -\frac{\lambda_I}{n'}\left[(w_{i+1})^{2n'+1}(p_{i+2}-p_i)\right]^{\frac{1}{n'}-1}\Big[(2n'+1)(w_{i+1})^{2n'}(p_{i+2}-p_i) \\ &+(w_{i+1})^{2n'+1}(A_{i+2,i+1}-A_{i,i+1})\Big] \\ &+ \frac{\lambda_I}{n'}\left[(w_{i-1})^{2n'+1}(p_i-p_{i-2})\right]^{\frac{1}{n'}-1}(w_{i-1})^{2n'+1}(A_{i,i+1}-A_{i-2,i+1}) \end{aligned} \tag{B.1c}$$

for $i = 1$

$$J_{1,j} = \delta_{ij} - \frac{\lambda_I}{n'}\left[\ (w_2)^{2n'+1}(p_3 - p_1)\right]^{\frac{1}{n'}-1}(w_2)^{2n'+1}(A_{3,j} - A_{1,j}), \quad j \neq 2 \tag{B.1d}$$

$$J_{1,2} = -\frac{\lambda_I}{n'}\left[\ (w_2)^{2n'+1}(p_3 - p_1)\right]^{\frac{1}{n'}-1}\Big[(2n'+1)(w_2)^{2n'}(p_3 - p_1) + (w_2)^{2n'+1}(A_{3,2} - A_{1,2})\Big] \tag{B.1e}$$

for $i = 2$

$$J_{2,j} = \delta_{2j} - \frac{\lambda_I}{n'}\left[(w_3)^{2n'+1}\,(p_4 - p_2)\right]^{\frac{1}{n'}-1}(w_3)^{2n'+1}(A_{4,j} - A_{2,j}) + \frac{\lambda_I}{n'}\left[(w_1)^{2n'+1}\,(p_2 - p_1)\right]^{\frac{1}{n'}-1}(w_1)^{2n'+1}(A_{2,j} - A_{1,j}), \quad j \neq 1, 3 \tag{B.1f}$$

$$J_{2,1} = -\frac{\lambda_I}{n'}\left[(w_3)^{2n'+1}\,(p_4 - p_2)\right]^{\frac{1}{n'}-1}(w_3)^{2n'+1}(A_{4,1} - A_{2,1}) + \frac{\lambda_I}{n'}\left[(w_1)^{2n'+1}\,(p_2 - p_1)\right]^{\frac{1}{n'}-1}\Big[(2n'+1)(w_1)^{2n'}(p_2 - p_1) + (w_1)^{2n'+1}(A_{2,1} - A_{1,1})\Big] \tag{B.1g}$$

$$J_{2,3} = -\frac{\lambda_I}{n'}\left[(w_3)^{2n'+1}\,(p_4 - p_2)\right]^{\frac{1}{n'}-1}\Big[(2n'+1)(w_3)^{2n'}(p_4 - p_2) + (w_3)^{2n'+1}(A_{4,3} - A_{2,3})\Big] + \frac{\lambda_I}{n'}\left[(w_1)^{2n'+1}\,(p_2 - p_1)\right]^{\frac{1}{n'}-1}(w_1)^{2n'+1}(A_{2,3} - A_{1,3}) \tag{B.1h}$$

for $i = n - 1$

$$J_{n-1,j} = \delta_{ij} - \frac{\lambda_I}{n'}\left[(w_n)^{2n'+1}\,(p_n - p_{n-1})\right]^{\frac{1}{n'}-1}(w_n)^{2n'+1}(A_{n,j} - A_{n-1,j}) + \frac{\lambda_I}{n'}\left[(w_{n-2})^{2n'+1}\,(p_{n-1} - p_{n-3})\right]^{\frac{1}{n'}-1}(w_{n-2})^{2n'+1}(A_{n-1,j} - A_{n-3,j}), \quad j \neq n-2, n \tag{B.1i}$$

$$J_{n-1,n-2} = -\frac{\lambda_I}{n'}\left[(w_n)^{2n'+1}\,(p_n - p_{n-1})\right]^{\frac{1}{n'}-1}(w_n)^{2n'+1}(A_{n,n-2} - A_{n-1,n-2}) + \frac{\lambda_I}{n'}\left[(w_{n-2})^{2n'+1}\,(p_{n-1} - p_{n-3})\right]^{\frac{1}{n'}-1}\Big[(2n'+1)(w_{n-2})^{2n'}(p_{n-1} - p_{n-3}) + (w_{n-2})^{2n'+1}(A_{n-1,n-2} - A_{n-3,n-2})\Big] \tag{B.1j}$$

$$J_{n-1,n} = -\frac{\lambda_I}{n'}\left[(w_n)^{2n'+1}(p_n - p_{n-1})\right]^{\frac{1}{n'}-1}\Big[(2n'+1)(w_n)^{2n'}(p_n - p_{n-1}) + (w_n)^{2n'+1}(A_{n,n} - A_{n-1,n})\Big] + \frac{\lambda_I}{n'}\left[(w_{n-2})^{2n'+1}(p_{n-1} - p_{n-3})\right]^{\frac{1}{n'}-1}(w_{n-2})^{2n'+1}(A_{n-1,n} - A_{n-3,n}) \quad \text{(B.1k)}$$

for $i = n$

$$J_{n,j} = \delta_{ij} + \frac{\lambda_I}{n'}\left[(w_{n-1})^{2n'+1}(p_n - p_{n-2})\right]^{\frac{1}{n'}-1}\left[(w_{n-1})^{2n'+1}(A_{n,j} - A_{n-2,j})\right], \quad j \neq n-1 \quad \text{(B.1l)}$$

$$J_{n,n-1} = \frac{\lambda_I}{n'}\left[(w_{n-1})^{2n'+1}(p_n - p_{n-2})\right]^{\frac{1}{n'}-1}\Big[(2n'+1)(w_{n-1})^{2n'}(p_n - p_{n-2}) + (w_{n-1})^{2n'+1}(A_{n,n-1} - A_{n-2,n-1})\Big] \quad \text{(B.1m)}$$

B.2 For right half-crack in *Grid II*

for $2 < i < n-1$

$$J_{i,j} = -\frac{\lambda_{II}}{n'}\left[w_i^{2n'+1}(p_{i+1} - p_i)\right]^{\frac{1}{n'}-1} w_i^{2n'+1}(A_{i+1,j} - A_{i,j}) + \frac{\lambda_{II}}{n'}\left[w_{i-1}^{2n'+1}(p_i - p_{i-1})\right]^{\frac{1}{n'}-1} w_{i-1}^{2n'+1}(A_{i,j} - A_{i-1,j}), \quad j \neq i, i-1 \quad \text{(B.2a)}$$

$$J_{i,i} = 1 - \frac{\lambda_{II}}{n'}\left[w_i^{2n'+1}(p_{i+1} - p_i)\right]^{\frac{1}{n'}-1}\Big[(2n'+1)w_i^{2n'}(p_{i+1} - p_i) + w_i^{2n'+1}(A_{i+1,j} - A_{i,j})\Big] + \frac{\lambda_{II}}{n'}\left[w_{i-1}^{2n'+1}(p_i - p_{i-1})\right]^{\frac{1}{n'}-1} w_{i-1}^{2n'+1}(A_{i,j} - A_{i-1,j}) \quad \text{(B.2b)}$$

$$J_{i,i-1} = -\frac{\lambda_{II}}{n'}\left[w_i^{2n'+1}(p_{i+1} - p_i)\right]^{\frac{1}{n'}-1} w_i^{2n'+1}(A_{i+1,i-1} - A_{i,i-1}) + \frac{\lambda_{II}}{n'}\left[w_{i-1}^{2n'+1}(p_i - p_{i-1})\right]^{\frac{1}{n'}-1}\Big[(2n'+1)w_{i-1}^{2n'}(p_i - p_{i-1}) + w_{i-1}^{2n'+1}(A_{i,i-1} - A_{i-1,i-1})\Big] \quad \text{(B.2c)}$$

for $i = 1$

$$J_{1,j} = -\frac{\lambda_{II}}{n'}\left[w_1^{2n'+1}(p_2 - p_1)\right]^{\frac{1}{n'}-1} w_1^{2n'+1}(A_{2,j} - A_{1,j}), \quad j \neq 1 \tag{B.2d}$$

$$J_{1,1} = 1 - \frac{\lambda_{II}}{n'}\left[w_1^{2n'+1}(p_2 - p_1)\right]^{\frac{1}{n'}-1}\left[(2n'+1)w_1^{2n'}(p_2 - p_1) + w_1^{2n'+1}(A_{2,1} - A_{1,1})\right] \tag{B.2e}$$

for $i = n$

$$J_{n,j} = \delta_{nj} + \frac{\lambda_{II}}{n'}\left[w_{n-1}^{2n'+1}(p_n - p_{n-1})\right]^{\frac{1}{n'}-1} w_{n-1}^{2n'+1}(A_{n,j} - A_{n-1,j}), \quad j \neq n-1 \tag{B.2f}$$

$$J_{n,n-1} = \frac{\lambda_{II}}{n'}\left[w_{n-1}^{2n'+1}(p_n - p_{n-1})\right]^{\frac{1}{n'}-1}\left[(2n'+1)w_{n-1}^{2n'}(p_n - p_{n-1}) + w_{n-1}^{2n'+1}(A_{n,n-1} - A_{n-1,n-1})\right]^{\frac{1}{n'}} \tag{B.2g}$$

B.3 For full inclined crack in *Grid II*

for $2 \leq i \leq \frac{n}{2} - 1$

$$J_{ij} = -\frac{\lambda}{n'}\left[w_{i+1}^{2n'+1}(p_{i+1} - p_i)\right]^{\frac{1}{n'}-1} w_{i+1}^{2n'+1}(A_{i+1,j} - A_{i,j}) + \frac{\lambda}{n'}\left[w_i^{2n'+1}(p_i - p_{i-1})\right]^{\frac{1}{n'}-1} w_i^{2n'+1}(A_{i,j} - A_{i-1,j}), \quad j \neq i, i+1 \tag{B.3a}$$

$$J_{i,i} = 1 - \frac{\lambda}{n'}\left[w_{i+1}^{2n'+1}(p_{i+1} - p_i)\right]^{\frac{1}{n'}-1} w_{i+1}^{2n'+1}(A_{i+1,i} - A_{i,i}) + \frac{\lambda}{n'}\left[w_i^{2n'+1}(p_i - p_{i-1})\right]^{\frac{1}{n'}-1}\left[(2n'+1)w_i^{2n'}(p_i - p_{i-1}) + w_i^{2n'+1}(A_{i,i} - A_{i-1,i})\right] \tag{B.3b}$$

$$J_{i,i+1} = -\frac{\lambda}{n'}\left[w_{i+1}^{2n'+1}(p_{i+1} - p_i)\right]^{\frac{1}{n'}-1}\left[(2n'+1)w_{i+1}^{2n'}(p_{i+1} - p_i) + w_{i+1}^{2n'+1}(A_{i+1,i+1} - A_{i,i+1})\right] + \frac{\lambda}{n'}\left[w_i^{2n'+1}(p_i - p_{i-1})\right]^{\frac{1}{n'}-1} w_i^{2n'+1}(A_{i,i+1} - A_{i-1,i+1}) \tag{B.3c}$$

for $\frac{n}{2}+2 \leq i \leq n-1$

$$J_{ij} = -\frac{\lambda}{n'}\left[w_i^{2n'+1}\left(p_{i+1}-p_i\right)\right]^{\frac{1}{n'}-1} w_i^{2n'+1}\left(A_{i+1,j}-A_{i,j}\right) + \frac{\lambda}{n'}\left[w_{i-1}^{2n'+1}\left(p_i-p_{i-1}\right)\right]^{\frac{1}{n'}-1} w_{i-1}^{2n'+1}\left(A_{i,j}-A_{i-1,j}\right), \quad j \neq i, i-1 \tag{B.3d}$$

$$J_{i,i} = 1 - \frac{\lambda}{n'}\left[w_i^{2n'+1}\left(p_{i+1}-p_i\right)\right]^{\frac{1}{n'}-1}\Big[(2n'+1)w_i^{2n'}\left(p_{i+1}-p_i\right) + w_i^{2n'+1}\left(A_{i+1,i}-A_{i,i}\right)\Big] + \frac{\lambda}{n'}\left[w_{i-1}^{2n'+1}\left(p_i-p_{i-1}\right)\right]^{\frac{1}{n'}-1} w_{i-1}^{2n'+1}\left(A_{i,i}-A_{i-1,i}\right) \tag{B.3e}$$

$$J_{i,i-1} = -\frac{\lambda}{n'}\left[w_i^{2n'+1}\left(p_{i+1}-p_i\right)\right]^{\frac{1}{n'}-1} w_i^{2n'+1}\left(A_{i+1,i-1}-A_{i,i-1}\right) + \frac{\lambda}{n'}\left[w_{i-1}^{2n'+1}\left(p_i-p_{i-1}\right)\right]^{\frac{1}{n'}-1}\Big[(2n'+1)w_{i-1}^{2n'}\left(p_i-p_{i-1}\right) + w_{i-1}^{2n'+1}\left(A_{i,i-1}-A_{i-1,i-1}\right)\Big] \tag{B.3f}$$

for $i = 1$

$$J_{1j} = \delta_{1j} - \frac{\lambda}{n'}\left[w_2^{2n'+1}\left(p_2-p_1\right)\right]^{\frac{1}{n'}-1} w_2^{2n'+1}\left(A_{2j}-A_{1j}\right), \quad j \neq 2 \tag{B.3g}$$

$$J_{12} = -\frac{\lambda}{n'}\left[w_2^{2n'+1}\left(p_2-p_1\right)\right]^{\frac{1}{n'}-1}\Big[(2n'+1)w_2^{2n'}\left(p_2-p_1\right) + w_2^{2n'+1}\left(A_{22}-A_{12}\right)\Big] \tag{B.3h}$$

for $i = n$

$$J_{n,j} = \delta_{nj} + \frac{\lambda}{n'}\left[w_{n-1}^{2n'+1}\left(p_n-p_{n-1}\right)\right]^{\frac{1}{n'}-1} w_{n-1}^{2n'+1}\left(A_{nj}-A_{n-1,j}\right), \quad j \neq n-1 \tag{B.3i}$$

$$J_{n,n-1} = \frac{\lambda}{n'}\left[w_{n-1}^{2n'+1}\left(p_n-p_{n-1}\right)\right]^{\frac{1}{n'}-1}\Big[(2n'+1)w_{n-1}^{2n'}\left(p_n-p_{n-1}\right) + w_{n-1}^{2n'+1}\left(A_{n,n-1}-A_{n-1,n-1}\right)\Big]^{\frac{1}{n'}} \tag{B.3j}$$

for $i = \frac{n}{2}$

$$J_{\frac{n}{2},j} = \frac{\lambda}{n'}\left[w_{\frac{n}{2}}^{2n'+1}\left(p_{\frac{n}{2}}-p_{\frac{n}{2}-1}\right)\right]^{\frac{1}{n'}-1} w_{\frac{n}{2}}^{2n'+1}\left(A_{\frac{n}{2},j}-A_{\frac{n}{2}-1,j}\right), \quad j \neq n/2 \tag{B.3k}$$

$$J_{\frac{n}{2},\frac{n}{2}} = 1 + \frac{\lambda}{n'}\left[w_{\frac{n}{2}}^{2n'+1}\left(p_{\frac{n}{2}}-p_{\frac{n}{2}-1}\right)\right]^{\frac{1}{n'}-1}\Big[(2n'+1)w_{\frac{n}{2}}^{2n'}\left(p_{\frac{n}{2}}-p_{\frac{n}{2}-1}\right)$$

$$+w_{\frac{n}{2}}^{2n'+1}\left(A_{\frac{n}{2},\frac{n}{2}}-A_{\frac{n}{2}-1,\frac{n}{2}}\right)\Big] \tag{B.3l}$$

for $i=\dfrac{n}{2}+1$

$$J_{\frac{n}{2}+1,j}=-\frac{\lambda}{n'}\left[w_{\frac{n}{2}+1}^{2n'+1}\left(p_{\frac{n}{2}+2}-p_{\frac{n}{2}+1}\right)\right]^{\frac{1}{n'}-1}w_{\frac{n}{2}+1}^{2n'+1}\left(A_{\frac{n}{2}+2,j}-A_{\frac{n}{2}+1,j}\right),$$

$$j\neq n/2+1 \tag{B.3m}$$

$$\begin{aligned}J_{\frac{n}{2}+1,\frac{n}{2}+1}=&1-\frac{\lambda}{n'}\left[w_{\frac{n}{2}+1}^{2n'+1}\left(p_{\frac{n}{2}+2}-p_{\frac{n}{2}+1}\right)\right]^{\frac{1}{n'}-1}\Big[(2n'+1)w_{\frac{n}{2}+1}^{2n'}\left(p_{\frac{n}{2}+2}-p_{\frac{n}{2}+1}\right)\\&+w_{\frac{n}{2}+1}^{2n'+1}\left(A_{\frac{n}{2}+2,\frac{n}{2}+1}-A_{\frac{n}{2}+1,\frac{n}{2}+1}\right)\Big]\end{aligned} \tag{B.3n}$$

B.4 For double parallel cracks in *Grid II*

for $2\leq i\leq\dfrac{n}{2}-1$, $n+2\leq i\leq\dfrac{3n}{2}-1$

$$\begin{aligned}J_{ij}=&-\frac{\lambda}{n'}\left[w_{i+1}^{2n'+1}\left(p_{i+1}-p_i\right)\right]^{\frac{1}{n'}-1}w_{i+1}^{2n'+1}\left(A_{i+1,j}-A_{i,j}\right)\\&+\frac{\lambda}{n'}\left[w_i^{2n'+1}\left(p_i-p_{i-1}\right)\right]^{\frac{1}{n'}-1}w_i^{2n'+1}\left(A_{i,j}-A_{i-1,j}\right),\quad j\neq i,i+1\end{aligned} \tag{B.4a}$$

$$\begin{aligned}J_{i,i}=&1-\frac{\lambda}{n'}\left[w_{i+1}^{2n'+1}\left(p_{i+1}-p_i\right)\right]^{\frac{1}{n'}-1}w_{i+1}^{2n'+1}\left(A_{i+1,i}-A_{i,i}\right)\\&+\frac{\lambda}{n'}\left[w_i^{2n'+1}\left(p_i-p_{i-1}\right)\right]^{\frac{1}{n'}-1}\Big[(2n'+1)w_i^{2n'}\left(p_i-p_{i-1}\right)\\&+w_i^{2n'+1}\left(A_{i,i}-A_{i-1,i}\right)\Big]\end{aligned} \tag{B.4b}$$

$$\begin{aligned}J_{i,i+1}=&-\frac{\lambda}{n'}\left[w_{i+1}^{2n'+1}\left(p_{i+1}-p_i\right)\right]^{\frac{1}{n'}-1}\Big[(2n'+1)w_{i+1}^{2n'}\left(p_{i+1}-p_i\right)\\&+w_{i+1}^{2n'+1}\left(A_{i+1,i+1}-A_{i,i+1}\right)\Big]\\&+\frac{\lambda}{n'}\left[w_i^{2n'+1}\left(p_i-p_{i-1}\right)\right]^{\frac{1}{n'}-1}w_i^{2n'+1}\left(A_{i,i+1}-A_{i-1,i+1}\right)\end{aligned} \tag{B.4c}$$

for $\dfrac{n}{2}+2\leq i\leq n-1$, $\dfrac{3n}{2}+2\leq i\leq 2n-1$

$$\begin{aligned}J_{ij}=&-\frac{\lambda}{n'}\left[w_i^{2n'+1}\left(p_{i+1}-p_i\right)\right]^{\frac{1}{n'}-1}w_i^{2n'+1}\left(A_{i+1,j}-A_{i,j}\right)\\&+\frac{\lambda}{n'}\left[w_{i-1}^{2n'+1}\left(p_i-p_{i-1}\right)\right]^{\frac{1}{n'}-1}w_{i-1}^{2n'+1}\left(A_{i,j}-A_{i-1,j}\right),\quad j\neq i,i-1\end{aligned} \tag{B.4d}$$

$$J_{i,i} =1 - \frac{\lambda}{n'}\left[w_i^{2n'+1}\left(p_{i+1}-p_i\right)\right]^{\frac{1}{n'}-1}\Big[(2n'+1)w_i^{2n'}\left(p_{i+1}-p_i\right) +w_i^{2n'+1}\left(A_{i+1,i}-A_{i,i}\right)\Big] + \frac{\lambda}{n'}\left[w_{i-1}^{2n'+1}\left(p_i-p_{i-1}\right)\right]^{\frac{1}{n'}-1} w_{i-1}^{2n'+1}\left(A_{i,i}-A_{i-1,i}\right) \tag{B.4e}$$

$$J_{i,i-1} =-\frac{\lambda}{n'}\left[w_i^{2n'+1}\left(p_{i+1}-p_i\right)\right]^{\frac{1}{n'}-1} w_i^{2n'+1}\left(A_{i+1,i-1}-A_{i,i-1}\right) + \frac{\lambda}{n'}\left[w_{i-1}^{2n'+1}\left(p_i-p_{i-1}\right)\right]^{\frac{1}{n'}-1}\Big[(2n'+1)w_{i-1}^{2n'}\left(p_i-p_{i-1}\right) +w_{i-1}^{2n'+1}\left(A_{i,i-1}-A_{i-1,i-1}\right)\Big] \tag{B.4f}$$

for $i = 1, n+1$

$$J_{i,j} =\delta_{1j} - \frac{\lambda}{n'}\left[w_{i+1}^{2n'+1}\left(p_{i+1}-p_i\right)\right]^{\frac{1}{n'}-1} w_{i+1}^{2n'+1}\left(A_{i+1,j}-A_{i,j}\right), \quad j \neq i+1 \tag{B.4g}$$

$$J_{i,i+1} =-\frac{\lambda}{n'}\left[w_{i+1}^{2n'+1}\left(p_{i+1}-p_i\right)\right]^{\frac{1}{n'}-1}\Big[(2n'+1)w_{i+1}^{2n'}\left(p_{i+1}-p_i\right) +w_{i+1}^{2n'+1}\left(A_{i+1,i+1}-A_{i,i+1}\right)\Big] \tag{B.4h}$$

for $i = n, 2n$

$$J_{i,j} =\delta_{nj} + \frac{\lambda}{n'}\left[w_{i-1}^{2n'+1}\left(p_i-p_{i-1}\right)\right]^{\frac{1}{n'}-1} w_{i-1}^{2n'+1}\left(A_{i,j}-A_{i-1,j}\right), \quad j \neq i-1 \tag{B.4i}$$

$$J_{i,i-1} =\frac{\lambda}{n'}\left[w_{i-1}^{2n'+1}\left(p_i-p_{i-1}\right)\right]^{\frac{1}{n'}-1}\Big[(2n'+1)w_{i-1}^{2n'}\left(p_i-p_{i-1}\right) +w_{i-1}^{2n'+1}\left(A_{i,i-1}-A_{i-1,i-1}\right)\Big]^{\frac{1}{n'}} \tag{B.4j}$$

for $i = \frac{n}{2}, \frac{3n}{2}$

$$J_{i,j} =\frac{\lambda}{n'}\left[w_i^{2n'+1}\left(p_i-p_{i-1}\right)\right]^{\frac{1}{n'}-1} w_i^{2n'+1}\left(A_{i,j}-A_{i-1,j}\right), \quad j \neq i \tag{B.4k}$$

$$J_{i,i} =1 + \frac{\lambda}{n'}\left[w_i^{2n'+1}\left(p_i-p_{i-1}\right)\right]^{i-1}\Big[(2n'+1)w_i^{2n'}\left(p_i-p_{i-1}\right) +w_{\frac{n}{2}}^{2n'+1}\left(A_{i,i}-A_{i-1,i}\right)\Big] \tag{B.4l}$$

for $i = \dfrac{n}{2} + 1, \dfrac{3n}{2} + 1$

$$J_{i,j} = -\frac{\lambda}{n'}\left[w_i^{2n'+1}\left(p_{i+1} - p_i\right)\right]^{\frac{1}{n'}-1} w_i^{2n'+1}\left(A_{i+1,j} - A_{i,j}\right), \quad j \neq i \tag{B.4m}$$

$$J_{i,i} = 1 - \frac{\lambda}{n'}\left[w_i^{2n'+1}\left(p_{i+1} - p_i\right)\right]^{\frac{1}{n'}-1}\left[(2n'+1)w_i^{2n'}\left(p_{i+1} - p_i\right) + w_i^{2n'+1}\left(A_{i+1,i} - A_{i,i}\right)\right] \tag{B.4n}$$

Part II

Previous Works

Chapter 6

Fabrication and characterization of THUNDER actuators, prestress-induced nonlinearity in the actuation response

Abstract

This paper documents an experimental and theoretical investigation in characterizing the mechanical configurations and performances of THUNDER actuators, a type of piezoelectric actuators known for their large actuation displacements, through fabrication, measurements and finite element analysis. Five groups of such actuators with different dimensions were fabricated using identical fabrication parameters. The as-fabricated arched configurations,

resulting from the thermo-mechanical mismatch among the constituent layers, and their actuation performances were characterized using an experimental setup based on a laser displacement sensor and through numerical simulations with ANSYS, a widely-used commercial software for finite element analysis. This investigation shows that the presence of large residue stresses within the piezoelectric ceramic layer, built up during the fabrication process leads to significant nonlinear electromechanical coupling in the actuator response to the driving electric voltage, and it is this nonlinear coupling that is responsible for the large actuation displacements. Furthermore, the severity of the residue stresses and thus the nonlinearity increases with the increasing substrate/piezoelectric thickness ratio and, to a less extent, with the decreasing in-plane dimensions of the piezoelectric layer.

6.1 Introduction

There have been numerous investigations on piezoelectric ceramics for developing electrically-driven actuators [1–18], for instance. Widely recognized piezoelectric actuators include MOONIE (Moon-Shaped Actuator) [19], RAINBOW (Reduced and Internally Biased Oxide Wafer) [20], CRESCENT (Stress-biased Ceramic-metal Composite Actuator) [21], THUNDER (Thin-layer Composite Unimorph Ferroelectric Driver and Sensor) [22], and LIPCA (Lightweight Piezo-composite Curved Actuator) [23]. THUNDER is referred to a type of high-performance piezoelectric actuators, which was developed originally by researchers at NASA Langley Research Center and is currently manufactured and marketed by FACE International Corporations [24]. What distinguishes THUNDER actuators from conventional piezoelectric actuators appears to be the utilization of the residue stresses in the piezoelec-

tric ceramic layer caused by the mismatch in the coefficients of thermal expansion (CTE) among the piezoelectric ceramic layer and the metallic substrate and the metallic top layer during the cooling stage of the fabrication process [25]. These stresses lead to an arched or bowed configuration as shown in Fig. 6.1.

In operation, the arch curvature increases or decreases in response to a transversely applied

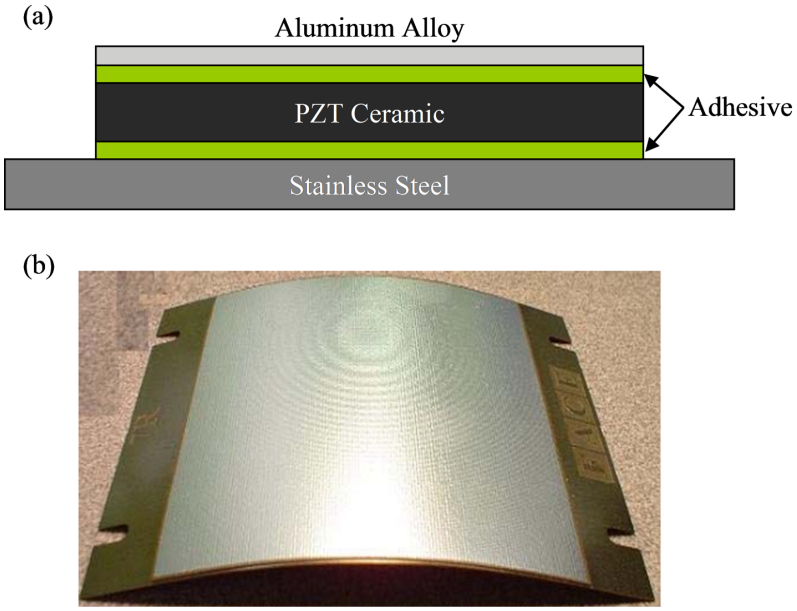

Figure 6.1: (a) A schematic illustration of the constituent layers of THUNDER Assembly (non-scale) (b) The resulting arched configuration of a THUNDER actuator due to thermal mismatch.

electric voltage, according to the poling direction of the piezoelectric ceramic layer. While, an alternating voltage potential drives the pumping motion of a THUNDER actuator. The advantages of THUNDER actuators in some applications compared to conventional actuators include large deflection and high actuation strength. In addition, THUNDER has a wide range of operation temperature from -40°C to 200°C and it can be effective even above the ultrasonic frequency (20 KHz). Furthermore, these actuators have been found

to be durable from the environmental shocks, vibrations and chemicals [24, 26–28]. A considerable amount of efforts have been made to evaluate the performances of THUNDER actuators with various dimensions, particularly concerned with the aspect ratio effect on the performance parameters [28–37]. This paper documents our effort in characterizing the arched configuration resulting from the cooling stage of the fabrication process and the deflection response to a transversely applied electric voltage. The next section describes the fabrication of five groups of THUNDER actuators, of which the dimensions have been standardized by FACE International Corporations, named Model 6R, 7R, 8R, 9R and 10R, respectively, and discusses the measurements on these actuators under the as-fabricated condition and under the loading of an electric voltage, respectively. We present, in Section 3, a finite element model and the corresponding analysis using ANSYS. The results show that the curvature of the arched configuration resulting from the cooling stage increases with the increasing substrate-to-piezoelectric thickness ratio, and, to a less extent, with the decreasing in-plane dimensions of the piezoelectric layer. Correspondingly, the magnitude of the compressive stress within the piezoelectric ceramic layer resulting from the CTE mismatch follows the same trends. These stresses are large enough to cause significant nonlinear effects in the deflection response of THUNDER actuators to applied electric voltages, rending the invalidity of the linear piezoelectric model. The nonlinear effect is responsible for the large actuation displacements of these actuators.

6.2 Fabrication and measurements

6.2.1 Fabrication

The structure of THUNDER actuator consists of five layers: a metal substrate made of stainless steel, a piezoelectric ceramic layer, an aluminum top layer and adhesive layers for bonding. The specific materials of these layers are described in Table 6.1 [25].

The five constituent layers were first assembled in a vacuum bag and then heated from

Layers	**Materials**
1st layer (Metal Substrate)	Stainless Steel 304
2nd layer (Adhesive)	LaRC^{TM}-SI Polyamide
3rd layer (Piezoelectric Ceramic)	PZT-5A (CTS-3195HD)
4th layer (Adhesive)	LaRC^{TM}-SI Polyamide
5th layer (Top Coating)	Aluminum Alloy 3003

Table 6.1: Constituent layers of THUNDER actuators

room temperature to 204°C in an autoclave. The assembly was subsequently pressurized to 241.3kPa with nitrogen and heated to 325°C, and it was kept under this condition for 30 minutes, before being depressurized and cooled down to 52°C. The rate of temperature change was maintained at 5.6°C/min during the fabrication process. During the cooling stage, LaRC^{TM}-SI polyamide is expected to solidify at the temperature range of 248-251°C, building incremental bonding between the ceramic and metallic layers. The stresses due to the inter-layer CTE mismatch result in the arched configuration, which depends primarily upon the dimensions and mechanical/thermal properties of the constituent layers as well as the solidification temperature of adhesive. There is some loss of polarization in the

piezoelectric ceramic layer during the fabrication process, because the assembly was heated very close to Curie temperature of PZT-5A (350°C). To compensate the loss of polarization, the actuators were re-poled at room temperature by applying 90 Volts per mil of ceramic thickness [22, 28].

6.2.2 Measurements

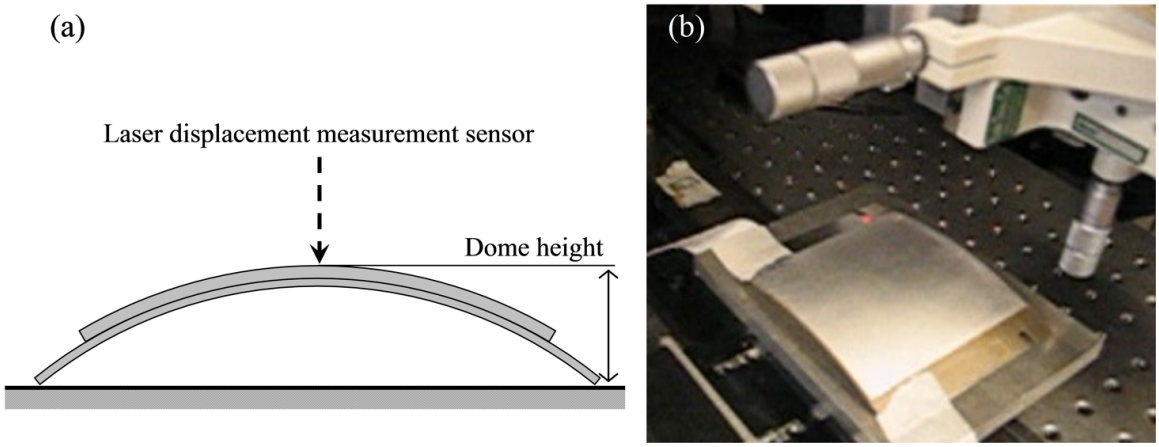

Figure 6.2: Measurements of dome heights (a) A schematic of the arched configuration under the simply supported condition, (b) Detection of the dome height using a laser displacement sensor.

Model	**6-R**	**7-R**	**8-R**	**9-R**	**10-R**
substrate (L×W, mm)	76.2×51.8	97.7×73.4	63.5×13.7	22.2×10.5	25.4×13.7
PZT layer (L×W, mm)	50.8×50.8	72.3×72.3	38.1×13.7	9.5×9.5	12.7×12.7
substrate (T, mm)	0.254	0.203	0.152	0.152	0.152
PZT layer (T, mm)	0.381	0.254	0.203	0.203	0.203

Table 6.2: Dimension comparison chart

Five models of THUNDER actuator (Model 6R, 7R, 8R, 9R and 10R) were prepared for the measurements. The dimensions of each model are given in Table 6.2 [24]. The measurements of the arched configuration and actuation performances under applied voltages were conducted by measuring the dome heights of THUNDER actuators using a laser displacement sensor under the simply supported condition as shown in Fig. 6.2. The sensor was installed perpendicular to the top surface of THUNDER. For measuring the dome heights, the THUNDER actuators were placed on a flat plate and the laser sensor scanned heights of the top surface through the center line of the actuator. Each scan consisted of over 100 data points, where were fitted to a curve and reduced to a single dome height. The displacements were calculated by comparing the as-fabricated dome heights to the dome heights under the applied electric voltages. To evaluate the performance of these THUNDER actuators, five different voltages were applied to each model. We note that the electromechanical response is constitutively related to the electric field strength, i.e., the electric voltage per unit thickness. Because the thickness differs significantly among the five models (0.381 mm for Model 6R, 0.254 mm for Model 7R, and 0.203 mm for Models 8R, 9R and 10R), the maximum electric voltages are chosen so that the maximum electric field strengths across the thickness are about 2000 V/mm for all these models. The measured dome heights and displacements under applied electrical voltages are given, respectively, in Tables 6.3 and 6.3. In these measurements, multiple samples were used for each model and significant variations between different samples were found, particularly for Models 9-R and 10-R with smaller in-plane dimensions.

Model	**6-R**	**7-R**	**8-R**	**9-R**	**10-R**
Dome Height	4.31 mm	9.57 mm	3.32 mm	0.85 mm	0.90 mm

Table 6.3: The as-fabricated dome heights of the THUNDER actuators

6-R	Applied voltage (V)	165	330	495	660	825
	(Electric field, V/mm)	(433)	(866)	(1299)	(1732)	(2165)
	Displacement (μm)	88.7	324.2	649.2	973.2	1297.2
7-R	Applied voltage (V)	103	206	309	412	515
	(Electric field, V/mm)	(406)	(811)	(1217)	(1622)	(2028)
	Displacement (μm)	236.2	653.4	1136.1	1660.7	2150.9
8-R	Applied voltage (V)	80	160	240	320	400
	(Electric field, V/mm)	(394)	(787)	(1181)	(1575)	(1969)
	Displacement (μm)	17.6	170.2	286.6	426.9	724.6
9-R	Applied voltage (V)	80	160	240	320	400
	(Electric field, V/mm)	(394)	(787)	(1181)	(1575)	(1969)
	Displacement (μm)	33.7	36.7	51.7	91.7	124.7
10-R	Applied voltage (V)	80	160	240	320	400
	(Electric field, V/mm)	(394)	(787)	(1181)	(1575)	(1969)
	Displacement (μm)	-103.0	-64.5	-7.5	40.0	85.3

Table 6.4: Displacements under applied electric voltages

6.3 Finite element analysis

6.3.1 Finite element model

We have developed a numerical model to analyze the THUNDER actuators, using the commercial finite element analysis software ANSYS [38]. The relevant properties of the constituent layers are listed in Tables 6.5 and 6.6.

The mechanical and electrical properties of PZT-5A provided by the vendor (CTS Cor-

Material	E (Gpa)	ν	CTE (10^{-6}/°C)
Stainless Steel 304	193.0	0.29	17.8
Aluminum Alloy 3003	68.9	0.33	25.1
PZT-5A (CTS-3195HD)		0.31	3.0
LaRC^{TM}-SI Polyamide	3.8	0.4	46.0 (23-150°C)
			60.0 (150-200°C)

Table 6.5: Material properties used in the finite element analysis [26, 39]

Dielectric Constant (1kHz)	Piezoelectric Charge Coefficient ($\times 10^{-12}$m/V)		Elastic Constant ($\times 10^{-12}$m^2/N)			
K_3^T	d_{31}	d_{33}	S_{11}^E	S_{33}^E	S_{11}^D	S_{33}^D
1900	-190	390	16.2	18.6	14.6	9.6

Table 6.6: Mechanical and electrical properties of PZT-5A (CTS-3195HD) [39]

poration) were converted to the form required by ANSYS. The vendor supplied properties are in following forms [40]:

$$S = s^E T + dE \tag{6.1}$$

$$D = d^t T + \varepsilon^T E \tag{6.2}$$

where $S,\ T,\ E,\ D,\ s^E$, d and ε^T are the mechanical strain vector, mechanical stress vector, electric field vector or electric flux density, electric displacement vector, compliance matrix, piezoelectric matrix relating strain/electric field and dielectric matrix evaluated at constant stress, respectively. However, ANSYS requires the matrices in forms below:

$$T = c^E S - eE \tag{6.3}$$

$$D = e^t S + \varepsilon^S E \tag{6.4}$$

where $c^E,\ e$ and ε^S are the stiffness matrix, piezoelectric matrix relating stress/electric field and dielectric matrix evaluated at constant strain, respectively.

Therefore, the vendor supplied matrices can be converted using the following relationships.

$$c^E = \left[s^E\right]^{-1} \tag{6.5}$$

$$\varepsilon^S = \varepsilon^T d^t - \left[s^E\right]^{-1} d \tag{6.6}$$

$$e = d^t \left[s^E\right]^{-1} \tag{6.7}$$

We take the assemblys configuration at the glass transition temperature of adhesive layer to be the initial stress-free state, from which our finite element simulation for the cooling stage begins. In the simulation, SOLID 226 (3-D coupled field 20-nodes solid) elements were applied to every constituent layer of the THUNDER assembly to analyze the thermo-mechanically coupled response of the assembly during the cooling stage. The el-

ement degrees of freedom for the metallic and adhesive layers are the three-dimensional displacements and temperature (DOF: UX, UY, UZ, TEMP). The PZT layer was considered as a thermal-piezoelectric model and its degrees of freedom were the displacements, temperature and electric voltage (DOF: UX, UY, UZ, TEMP, VOLT). The cooling stage is modeled as a quasi-static process, and thus the temperature is the sole variation variable in the corresponding simulation. For the subsequent electric loading, we are interested in the resulting deflection, instead of the transient behavior. Thus the voltage is the sole variation variable in the simulation for the electric loading stage that follows the cooling stage. Therefore, the static analysis was performed and SPARSE iterative solver was utilized during these simulations [41]. Although the linear constitutive relations listed above were adopted, the geometrical non-linear analysis was performed throughout the simulations on both the cooling and electrical loading stages. We note the technical challenges in using ANSYS to retain the residue stresses along with the arched configurations in the subsequent electric-loading process simulations.

6.3.2 Simulation results

The cooling stage

The arched configuration of a THUNDER actuator (7-R model) upon the completion of the cooling stage is shown in Fig. 6.3, in which the contoured color bands represent the transverse displacement, i.e., the z-component of the displacement in the coordinate system indicated in the figure. The dome heights obtained from our ANSYS simulations for all five models of THUNDER actuators are listed in Table 6.7, together with the measured dome heights and the values published on the website of the FACE International Corporation [24].

Note that the measured dome height was obtained by measuring the distance between the center of the actuator top surface and the sitting plate under the simply supported condition, as illustrated schematically in Fig. 6.2. The comparisons indicate that the simulation results are consistent with our measurements for all five models of THUNDER actuators. We note, however, that our measured dome heights are correlated well to those published by FACE only for the three large actuators, i.e., Models 6R, 7R and 8R, and there are significant discrepancies for two small actuators, i.e., Models 9R and 10R. It is known that there are variations among sample actuators, and the relative variations are larger for smaller actuators. Note that the measurement values obtained from FACE are single-point data and they are provided here for comparison.

The variation of the lateral stress (the x-component) along the PZT thickness at the

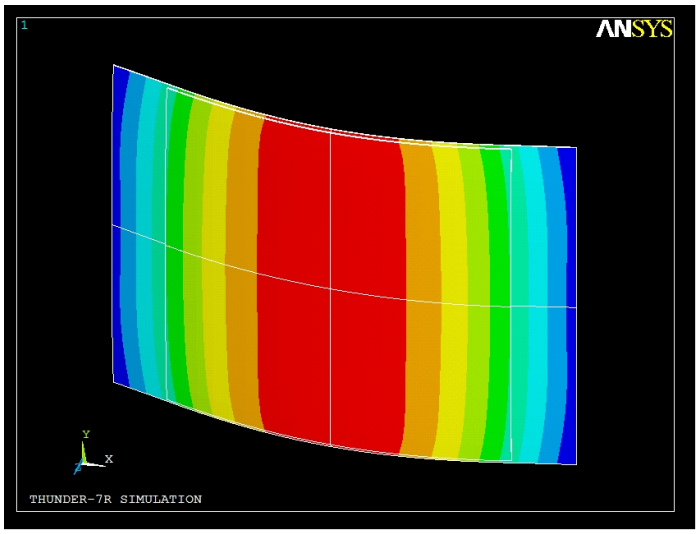

Figure 6.3: The arched configuration of THUNDER 7-R model resulting from the cooling stage simulation

midpoint ($x = 0$ and $y = 0$) is plotted in Fig. 6.4, for each of the five model actuators.

Model	6-R	7-R	8-R	9-R	10-R
Measured	4.31 mm	9.57 mm	3.32 mm	0.85 mm	0.90 mm
FACE International	4.24 mm	9.55 mm	3.84 mm	0.61 mm	0.64 mm
Calculated	4.56 mm	9.41 mm	3.19 mm	0.74 mm	0.91 mm
Measured vs. FACE	1.5%	0.2%	-13.6%	38.86%	41.1%
Calculated vs. Measured	6.0%	-1.6%	-3.7%	-12.3%	0.7%

Table 6.7: Comparison of dome heights data

Note that the vertical axis in Fig. 6.4 is the actuator thickness normalized to the unity. The thermal stresses caused by the CTE mismatch are compressive within the PZT layer and tensile in the metallic layers (not plotted). These stresses are responsible for the resulting arched configurations. We note that this stress distribution qualitatively differs from the stress distribution in a layered beam under bending. From the conventional theory for layered beams under bending, there exists a neutral surface and the stresses are tensile on one side of this surface and are compressive on the other side.

The electrical loading process

In Fig. 6.5, we have plotted the actuation displacements versus the transversely applied electric voltages for Model 6-R and 7-R[1] . The actuation displacements obtained from the finite element analysis correlate well with the measured values and those from FACE International Corporation only for small deflections under relatively low electric voltages. The

[1]1 For small actuators, our measured deflection values differ significantly from those of FACE International Corporation. We attribute these discrepancies to the sample variations and the error margins as well as the uncertainties associated with the measurement methods. With our laser sensor setup, we measured the dome height at each value of the applied electric voltage and derived the corresponding deflection by subtracting the measured dome height without the electric loading. While the details of measurement procedures of FACE International Corporation were not provided

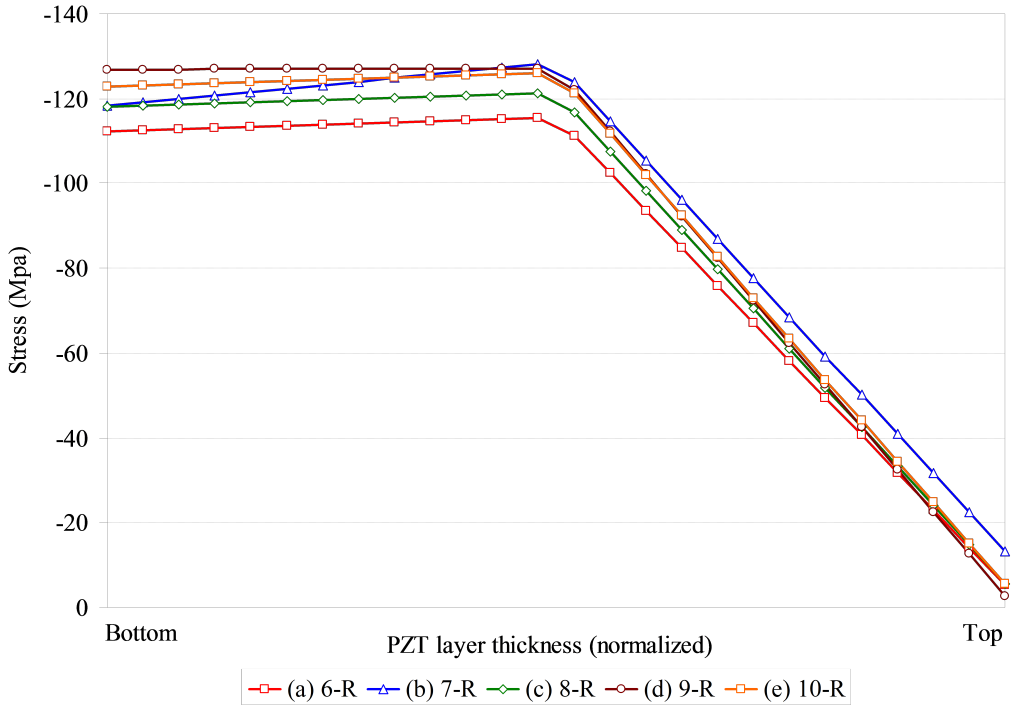

Figure 6.4: Distribution of the residual thermal stresses (x-component) in the PZT layer along the actuator thickness, normalized to the unity for each of the five models

discrepancies increase with the increasing applied voltages. In particular, the measured values exhibit significant nonlinearity in the actuator deflection response to the applied electric voltages, while the finite element analysis results correspond to a linear response, as expected from ANSYS. It is known in the literature, [42–44] for example, that stresses can cause changes in macroscopic polarization, and even polarization switching, of piezoelectric materials, leading to nonlinear macroscopic responses to mechanical and electrical loading programs. We have conducted finite element analyses and simulations on a large number of samples with various dimensions. The results conclude that the curvature of the arched configuration resulting from the cooling stage increases with the increasing substrate-to-piezoelectric thickness ratio, and, to a less extent, with the decreasing in-plane dimensions of the piezoelectric layer, as shown in Table 6.8. Correspondingly, the magnitude of the

compressive stress within the piezoelectric ceramic layer resulting from the CTE mismatch follows the same trends. As shown in Fig. 6.4, Model 7R of the largest thickness ratio (0.799) has the largest compressive stress, while Model 6R of the smallest thickness ratio (0.667) has the smallest compressive stress. Correspondingly, Model 7R exhibits larger nonlinear effect than Model 6R in the deflection response to the applied electric voltage, as seen in Fig. 6.5. In the figure, our multiple-point measurements are indicated by the error bars, while the data from FACE International and our finite element calculations are single-point values. Note that the curves are fitted with second-order polynomials. It is apparent that the stresses resulting from the cooling stage are large enough to cause significant electromechanical coupling, leading to the nonlinear effects, and thus the conventional linear piezoelectric theory should be modified in order to model the deflection responses of THUNDER actuators to high electric voltages.

There have been many investigations, both experimental and theoretical, on the nonlinear

Model	**6-R**	**7-R**	**8-R**	**9-R**	**10-R**
S/P thickness ratio	0.67	0.80	0.75	0.75	0.75
PZT in-plane dimension(mm)	50.8×50.8	72.3×72.3	38.1×13.7	9.59.5	12.7×12.7
Curvature	5.12	7.66	6.72	7.36	7.08

Table 6.8: Relation between thickness ratio, PZT in-plane dimension and curvature

responses of piezoelectric ceramics under coupled electro-mechanical loading programs, such as [45–51]. We hope to develop a numerical model from one of these theories for analyzing THUNDER actuators, and this model would have to be simple enough to be implemented

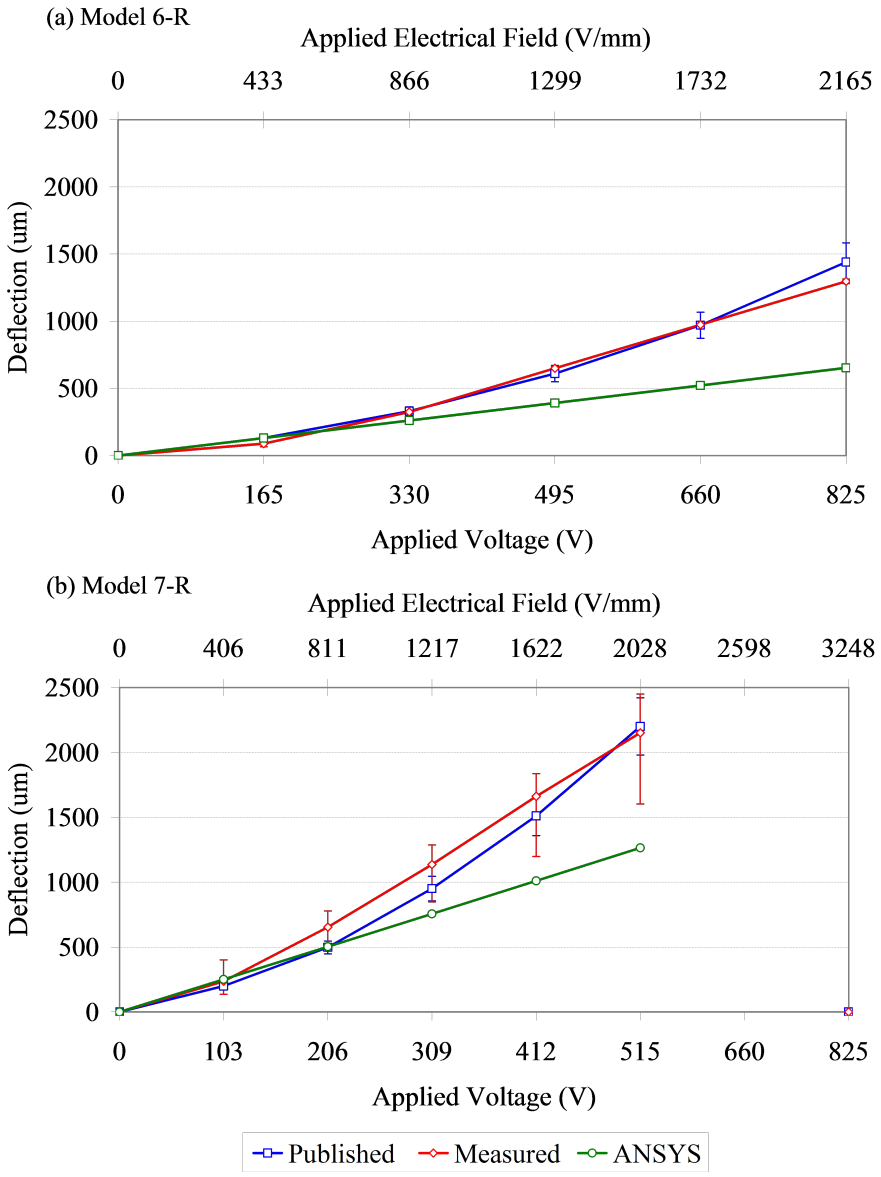

Figure 6.5: Deflections under applied voltages (a) Model 6-R, (b) Model 7-R

into ANSYS to serve the community of engineering researchers who are interested in the applications of THUNDER actuators.

6.4 Concluding remarks

The experimental measurements and the numerical simulations show excellent consistency in characterizing the arched configurations resulting from the cooling stage of the fabrication process due to the mismatch in the coefficients of thermal expansion of the constituent layers. For the actuation displacements in the electric loading stage, the measurements indicate the significant nonlinearity in the THUNDER actuator response to applied electrical voltage variations, rending the invalidity of the linear piezoelectric model deployed with ANSYS. The observed nonlinear response is attributed to the fact that the residue stresses within the piezoelectric layer of the arched actuator configuration cause significant nonlinear electromechanical coupling in the actuation performance under the driving electric voltage. It is this nonlinear coupling that is responsible for the large actuation displacements. The residue stresses increases with the increasing substrate-to-piezoelectric thickness ratio, and to a less extent, with the decreasing in-plane dimensions of the piezoelectric layer.

Bibliography

[1] E. V. Ardelean, D. G. Cole, and R. L. Clark, "High performance V-stack piezoelectric actuator," *Journal of intelligent material systems and structures*, vol. 15, no. 11, pp. 879–889, 2004.

[2] A. Bechet, Y. H. Berthelot, and C. S. Lynch, "A stress gradient-enhanced piezoelectric actuator composite (GEPAC) with integrated ultrasonic NDE capability for continuous health monitoring," *Journal of intelligent material systems and structures*, vol. 16, no. 1, pp. 85–93, 2005.

[3] S. Dong, K. Uchino, L. Li, and D. Viehland, "Analytical solutions for the transverse deflection of a piezoelectric circular axisymmetric unimorph actuator," *Ultrasonics, Ferroelectrics and Frequency Control, IEEE Transactions on*, vol. 54, no. 6, pp. 1240–1249, 2007.

[4] B. Edinger, M. Frecker, and J. Gardner, "Dynamic modeling of an innovative piezoelectric actuator for minimally invasive surgery," *Journal of intelligent material systems and structures*, vol. 11, no. 10, pp. 765–770, 2000.

[5] J. Gao and L. Cheng, "Modelling of a high performance piezoelectric actuator assembly for active and passive vibration control," *Smart materials and structures*, vol. 13, no. 2, p. 384, 2004.

[6] G. H. Haertling, "Ferroelectric ceramics: history and technology," *Journal of the American Ceramic Society*, vol. 82, no. 4, pp. 797–818, 1999.

[7] G. Huang and C. Sun, "The dynamic behaviour of a piezoelectric actuator bonded to an anisotropic elastic medium," *International Journal of Solids and Structures*, vol. 43, no. 5, pp. 1291 – 1307, 2006.

[8] Y.-T. Huang, W.-J. Wu, Y.-C. Wang, and C.-K. Lee, "Multilayer modal actuator-based piezoelectric transformers," *Ultrasonics, Ferroelectrics and Frequency Control, IEEE Transactions on*, vol. 54, no. 2, pp. 359–367, 2007.

[9] S. Lee, B. C. Cho, H. C. Park, N. S. Goo, and K. J. Yoon, "Piezoelectric actuator–sensor analysis using a three-dimensional assumed strain solid element," *Journal of intelligent material systems and structures*, vol. 15, no. 5, pp. 329–338, 2004.

[10] D.-c. Lee, D.-w. Yun, and C.-s. Han, "A material rigidity effect of a bimorph piezoelectric actuator," *Smart materials and structures*, vol. 16, no. 4, p. 1043, 2007.

[11] C. Lim and C. Lau, "A new two-dimensional model for electro-mechanical response of thick laminated piezoelectric actuator," *International journal of solids and structures*, vol. 42, no. 20, pp. 5589–5611, 2005.

[12] Y. Liu, H. Fan, and J. Yang, "Analysis of the shear stress transferred from a partially electroded piezoelectric actuator to an elastic substrate," *Smart materials and structures*, vol. 9, no. 2, p. 248, 2000.

[13] C. Mo, R. Wright, W. S. Slaughter, and W. W. Clark, "Behaviour of a unimorph circular piezoelectric actuator," *Smart materials and structures*, vol. 15, no. 4, p. 1094, 2006.

[14] A. Mtawa, B. Sun, and J. Gryzagoridis, "An investigation of the influence of substrate geometry and material properties on the performance of the C-shape piezoelectric actuator," *Smart materials and structures*, vol. 16, no. 4, p. 1036, 2007.

[15] J. Park, G. P. Carman, and H. T. Hahn, "Design and testing of a mesoscale piezoelectric inchworm actuator with microridges," *Journal of intelligent material systems and structures*, vol. 11, no. 9, pp. 671–684, 2000.

[16] S.-C. Woo, K. H. Park, and N. S. Goo, "Influences of dome height and stored elastic energy on the actuating performance of a plate-type piezoelectric composite actuator," *Sensors and Actuators A: Physical*, vol. 137, no. 1, pp. 110–119, 2007.

[17] T. Zhang and Q.-M. Wang, "Performance evaluation of a valveless micropump driven by a ring-type piezoelectric actuator," *Ultrasonics, Ferroelectrics and Frequency Control, IEEE Transactions on*, vol. 53, no. 2, pp. 463–473, 2006.

[18] G. Zhou and Q. Wang, "Design of a smart piezoelectric actuator based on a magnetorheological elastomer," *Smart materials and structures*, vol. 14, no. 4, p. 504, 2005.

[19] K. Onitsuka, A. Dogan, J. F. Tressler, Q. Xu, S. Yoshikawa, and R. E. Newnham, "Metal-ceramic composite transducer, the Moonie," *Journal of Intelligent Material Systems and Structures*, vol. 6, no. 4, pp. 447–455, 1995.

[20] G. H. Haertling, "Rainbow ceramics- a new type of ultra-high-displacement actuator," *American Ceramic Society Bulletin*, vol. 73, no. 1, pp. 93–96, 1994.

[21] S. Chandran, V. D. Kugel, and L. E. Cross, "CRESCENT: a novel piezoelectric bending actuator," in *Smart Structures and Materials' 97*, pp. 461–469, International Society for Optics and Photonics, 1997.

[22] R. F. Hellbaum, R. G. Bryant, and R. L. Fox, "Thin layer composite unimorph ferroelectric driver and sensor," May 27 1997. US Patent 5,632,841.

[23] K. J. Yoon, S. Shin, H. C. Park, and N. S. Goo, "Design and manufacture of a lightweight piezo-composite curved actuator," *Smart Materials and Structures*, vol. 11, no. 1, p. 163, 2002.

[24] THUNDER data sheets, Face International Corporation, 427 W 35TH St. Norfolk, VA 23508, USA, http://www.faceco.com.

[25] C. Niezrecki, D. Brei, S. Balakrishnan, and A. Moskalik, "Piezoelectric actuation: state of the art," *The shock and vibration digest*, vol. 33, no. 4, pp. 269–280, 2001.

[26] R. G. Bryant, "LaRC^{TM}-SI: a soluble aromatic polyimide," *High Performance Polymers*, vol. 8, no. 4, pp. 607–615, 1996.

[27] T. Hou and R. Bryant, "Processing and properties of IM7/LaRC^{TM}-SI polyimide composites," *High performance polymers*, vol. 9, no. 4, pp. 437–448, 1997.

[28] K. M. Mossi, G. V. Selby, and R. G. Bryant, "Thin-layer composite unimorph ferroelectric driver and sensor properties," *Materials Letters*, vol. 35, no. 1, pp. 39–49, 1998.

[29] S. Aimmanee and M. Hyer, "A comparison of the deformations of various piezoceramic actuators," *Journal of intelligent material systems and structures*, vol. 17, no. 2, pp. 167–186, 2006.

[30] M. Capozzoli, J. Gopalakrishnan, K. Hogan, J. Massad, T. Tokarchik, S. Wilmarth, H. T. Banks, K. M. Mossi, and R. C. Smith, "Modeling aspects concerning THUNDER actuators," in *Proceedings of the SPIE, Smart Structures and Materials*, vol. 3667, pp. 719–727, 1999.

[31] S. W. Chung and S. J. Kim, "Investigation of actuating displacement performance of curved actuator by large-scale computation," *Smart materials and structures*, vol. 14, no. 4, p. 615, 2005.

[32] M. Hyer and A. Jilani, "Predicting the deformation characteristics of rectangular unsymmetrically laminated piezoelectric materials," *Smart Materials and Structures*, vol. 7, no. 6, p. 784, 1999.

[33] C. Kennedy, T. Usher, J. Mulling, and A. Kingon, "Modeling and simulation of THUNDER actuators using ANSYS finite element analysis," in *Modeling and Simulation of Microsystems*, pp. 330–3, 2001.

[34] K. M. Mossi, R. P. Bishop, R. C. Smith, and H. T. Banks, "Evaluation criteria for THUNDER actuators," in *Proc. SPIE Smart Struct. Mater*, vol. 3667, pp. 738–743, 1999.

[35] K. M. Mossi and R. P. Bishop, "Characterization of different types of high performance THUNDER actuators," *Stainless Steel*, vol. 302, pp. 0–1524, 1999.

[36] B. K. Taleghani, "Validation of high displacement piezoelectric actuator finite element models," in *Symposium on Applied Photonics*, pp. 37–45, International Society for Optics and Photonics, 2000.

[37] S. A. Wise, "Displacement properties of RAINBOW and THUNDER piezoelectric actuators," *Sensors and Actuators A: Physical*, vol. 69, no. 1, pp. 33–38, 1998.

[38] ANSYS® Academic Research, Release 11.0.

[39] PZT5A & 5H materials technical data, CTS Electronic Component, Inc., 4800 Alameda Blvd. NE, Albuquerque, NM 87113, USA, http://www.ctswireless.com.

[40] ANSYS® Academic Research, Release 11.0, Help System, Theory Reference Manual, ANSYS, Inc.

[41] ANSYS® Academic Research, Release 11.0, Help System, Coupled Field Analysis Guide, ANSYS, Inc.

[42] J. Huber, N. Fleck, C. Landis, and R. McMeeking, "A constitutive model for ferroelectric polycrystals," *Journal of the Mechanics and Physics of Solids*, vol. 47, no. 8, pp. 1663–1697, 1999.

[43] M. Kamlah and Q. Jiang, "A constitutive model for ferroelectric PZT ceramics under uniaxial loading," *Smart materials and structures*, vol. 8, no. 4, p. 441, 1999.

[44] D. Zhou, M. Kamlah, and D. Munz, "Effects of uniaxial prestress on the ferroelectric hysteretic response of soft PZT," *Journal of the European Ceramic Society*, vol. 25, no. 4, pp. 425–432, 2005.

[45] N. W. Hagood IV and A. J. McFarland, "Modeling of a piezoelectric rotary ultrasonic motor," *Ultrasonics, Ferroelectrics and Frequency Control, IEEE Transactions on*, vol. 42, no. 2, pp. 210–224, 1995.

[46] R. E. Loge and Z. Suo, "Nonequilibrium thermodynamics of ferroelectric domain evolution," *Acta materialia*, vol. 44, no. 8, pp. 3429–3438, 1996.

[47] C. Lynch, L. Chen, Z. Suo, R. McMeeking, and W. Yang, "Crack growth in ferroelectric ceramics driven by cyclic polarization switching," *Journal of Intelligent Material Systems and Structures*, vol. 6, no. 2, pp. 191–198, 1995.

[48] T. Usher and A. Sim, "Nonlinear dynamics of piezoelectric high displacement actuators in cantilever mode," *Journal of applied physics*, vol. 98, no. 6, pp. 064102–064102, 2005.

[49] V. V. Varadan, J. Kim, and V. K. Varadan, "Modeling of piezoelectric sensor fidelity," *Ultrasonics, Ferroelectrics and Frequency Control, IEEE Transactions on*, vol. 44, no. 3, pp. 538–547, 1997.

[50] D. Viehland and Y.-H. Chen, "Random-field model for ferroelectric domain dynamics and polarization reversal," *Journal of Applied Physics*, vol. 88, no. 11, pp. 6696–6707, 2000.

[51] M.-L. Zhu, S.-W. Lee, T.-Y. Zhang, and P. Tong, "Modeling of a rotary motor driven by an anisotropic piezoelectric composite laminate," *Ultrasonics, Ferroelectrics and Frequency Control, IEEE Transactions on*, vol. 47, no. 6, pp. 1561–1574, 2000.

Chapter 7

Design and analysis of micro SAW-IDT accelerometer based on the perturbation of surface acoustic wave on strained surface

Abstract

A new four cantilevered micro SAW-IDT accelerometer is proposed and analyzed by theoretical and finite element analysis. The accelerometer is based on Rayleigh type surface wave propagating over the surface of the plate cantilever made of single crystal silicon. It operates at 1 GHz wirelessly with an external driving electric signal and the corresponding wavelength is 4.917μm. The frequency shift of the surface acoustic wave is determined under

an initial biasing field caused by an applied initial force. The analysis is performed by the first-order perturbation integral theory for small fields superposed on finite biasing fields in an elastic body and the prestressed full transient finite element analysis which is developed for embodiment of the first-order perturbation theory in computer simulation. The results of both theoretical and finite element analysis show excellent consistency in sensitivity and it provides a good insight for the more complicated system design which requires a large scale computation.

7.1 Introduction

The technology using surface acoustic wave (SAW) induced by the inter-digital transducer (IDT) is widely used in communication devices and sensors. For the sensor application, SAW-IDT device basically convert the change of environment such as temperature and inertial force to the change in wave properties such as frequency and phase. During the conversion in SAW-IDT devices, a small environmental factor affecting acoustic wave properties causes a relatively large shift in the electromagnetic properties. Using the characteristics of SAW-IDT device, which is highly sensitive to its environment, there have been numerous investigations for developing highly sensitive mechanical, thermal, chemical and bio-medical sensors [1–8], for instance, a high sensitivity resonator pressure sensor [9, 10], a MEMS-IDT based accelerometer utilizing a movable reflectors [11], a wireless SAW temperature sensor [12] and a SAW resonator chemical vapor detection sensor [13]. In this paper, we primarily focus on the sensitivity of the frequency response of micro SAW-IDT accelerometer to the applied inertial force. Thus, we study the perturbation of surface acoustic wave

properties under the initial bias fields caused by the various external inertial forces acting on the normal direction. The new four cantilevered micro SAW-IDT accelerometer is proposed and analyzed by theoretical and finite element analysis. The first-order perturbation integral theory by Tiersten is adopted to show the effect of the initial field on the wave frequency in theoretical analysis [14]. Then the prestressed full transient finite element model is developed to observe the effect of the perturbed second-order elastic constant under an initial field. The the modified second-order elastic constants under an initial field form the perturbation integral theory is implemented in the finite element model. The computer simulation is performed and analyzed using ANSYS, a widely used commercial software for finite element analysis.

7.2 Design of micro SAW-IDT accelerometer

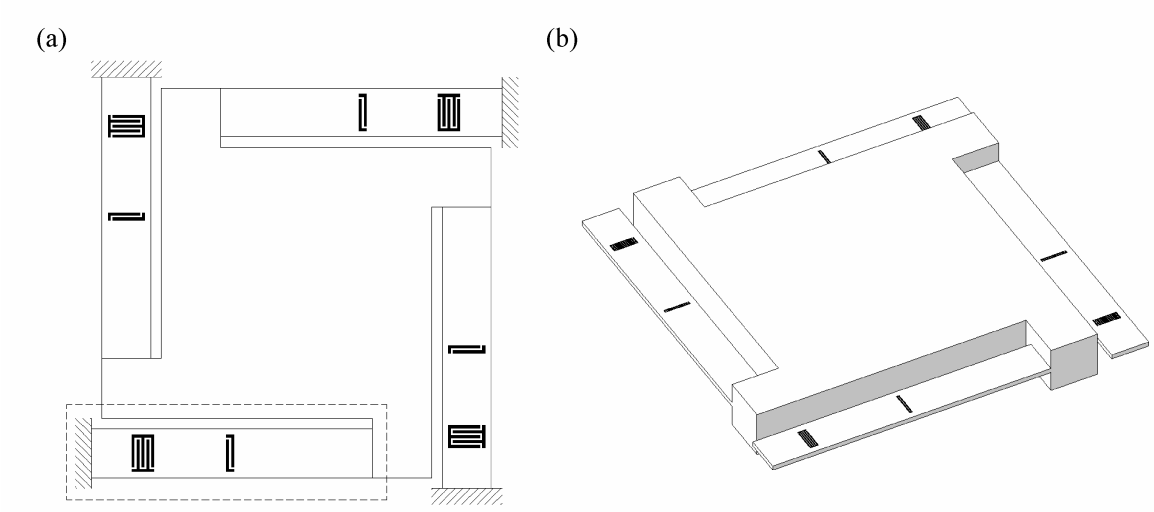

Figure 7.1: Schematic design of Micro SAW-IDT accelerometer

A schematic design of micro SAW-IDT accelerometer is proposed as shown in Fig. 7.1. The proof mass is supported by four cantilever plates and a pair of transmitter and receiver IDTs are placed on the each cantilever. The other ends of cantilevers are fixed to the support structure or casing. Therefore, each cantilever supports one-quarter of proof mass and works as an independent sensor with a pair of IDTs in four different locations. When an external force P is applied on normal direction of the surface of proof mass, a small bias field will be created along the the cantilever, where the external inertial force can be expressed by a product of mass of proof mass and applied acceleration. The transmitter IDTs are connected to the antenna which activate the IDTs wirelessly by an external electric driving signal to generate surface acoustic wave for propagation along the surface of cantilever plate. The receiver IDTs convert the mechanical force created by wave propagation into the electrical signal and send it back to the local station for analysis. If it is assumed that the properties of surface acoustic wave (i.e. frequency, phase or velocity) are perturbed by the small biasing field during the propagation, then, the external force P can be determined by measuring the change in properties of the surface acoustic wave between the transmitter and receiver IDTs. Then, the sensitivity and sensing range can be adjusted by changing geometrical parameters and materials. The advantage of using the configuration of this design is that the acceleration or external force P can be detected in four different locations which gives more stable and reliable data. And, the accelerometer can be easily calibrated by putting the thin electrode film on the top and bottom surfaces of the proof mass and the casing. This allows the electric actuation force replaces the initial force in calibration mode and also provides another differential capacitance accelerometer in sensing mode.

7.3 Theoretical analysis

7.3.1 Unperturbed surface acoustic wave

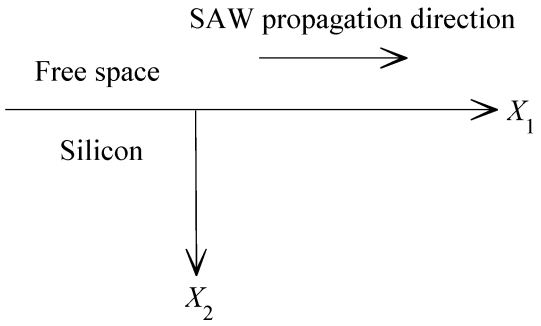

Figure 7.2: An elastic half-space and the coordinate system for surface acoustic wave

Consider an elastic half-space of silicon in a Cartesian coordinate system $X_k(X_2 > 0)$ as shown in Fig. 7.2. Silicon has the crystallographic characteristics of $m3m$ cubic crystal symmetry and allows plane-strain motions with $u_3 = 0$ and $\partial_3 = 0$. Rayleigh waves propagating in the [100] direction of the (001) plane is studied. The Rayleigh wave solutions in a half-space of $m3m$ cubic crystals with a traction-free boundary surface are given by [15]:

$$u_1 = \exp\left(-2\pi h\frac{X_2}{\lambda_R}\right)\cos\left(2\pi g\frac{X_2}{\lambda_R}+\alpha\right)\exp i\left[\omega\left(t-\frac{X_1}{V_R}\right)-\alpha\right] \tag{7.1a}$$

$$u_2 = ir\exp\left(-2\pi h\frac{X_2}{\lambda_R}\right)\cos\left(2\pi g\frac{X_2}{\lambda_R}-\alpha\right)\exp i\left[\omega\left(t-\frac{X_1}{V_R}\right)-\alpha\right] \tag{7.1b}$$

where $h,\ \lambda_R,\ g,\ \alpha,\ V_R$ and r depend on material parameters.

The real parts solutions of displacements in Eq. (7.1) are:

$$\mathrm{Re}[u_1] = U_1(X_2)\cos\left[\omega\left(t-\frac{X_1}{V_R}\right)-\alpha\right] \tag{7.2a}$$

$$\mathrm{Re}[u_2] = U_2(X_2)\sin\left[\omega\left(t-\frac{X_1}{V_R}\right)-\alpha\right] \tag{7.2b}$$

where the longitudinal and the shear amplitudes of Eq. (7.2) are:

$$U_1(X_2) = \exp\left(-2\pi h\frac{X_2}{\lambda_R}\right)\cos\left(2\pi g\frac{X_2}{\lambda_R}+\alpha\right) \tag{7.3a}$$

$$U_2(X_2) = r\exp\left(-2\pi h\frac{X_2}{\lambda_R}\right)\cos\left(2\pi g\frac{X_2}{\lambda_R}-\alpha\right) \tag{7.3b}$$

The Rayleigh wave solutions provide displacements of surface wave with frequency ω and wave number ξ in absence of initial fields.

7.3.2 Initial fields

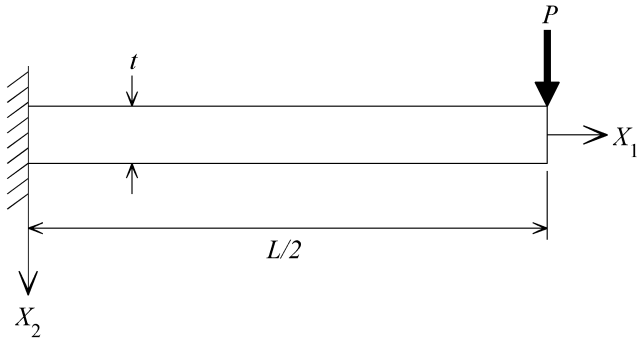

Figure 7.3: Simplified model for theoretical and finite element analysis

To determine the initial fields on the cantilevers created by an external force P, the dashed area of Fig. 7.1 is simplified as shown in Fig. 7.3. The cantilever Fig. 7.1 is fixed and guided by proof mass at each end, but only the first half of cantilever from the fixed support is modeled because we are interested in this portion of cantilever where the pair of transmitter and receiver IDTs are placed. The initial fields are to be found using the classical plate theory and they will be implemented to the perturbation integral in following chapter to find the effect of the existence of the initial fields on propagation of surface acoustic wave. In case of shown in Fig. 7.3, the cantilever is subjected to the bending moment, $M(X_1) =$

$P(L/2 - X_1)$. For plane-strain motion with $w_3 = 0$ and $\partial_3 = 0$, the deflection $w_2(X_1)$ is given by:

$$-\frac{t^3}{12}\gamma_{11}w_{2,11} = M(X_1) = P\left(\frac{L}{2} - X_1\right) \tag{7.4}$$

and this leads to:

$$w_2 = \frac{6P}{\gamma_{11}t^3}\left(\frac{X_1^3}{3} - \frac{L}{2}X_1^2\right) \tag{7.5}$$

where $0 \leq X_1 \leq L/2,\ -h \leq X_2 \leq h,\ t = 2h$ and Voigt's anisotropic plate elastic constant is given by [16]:

$$\gamma_{11} = c_{11} - \frac{c_{12}^2}{c_{11}} \tag{7.6}$$

The displacement gradients required for the perturbation integral can be determined from the procedure in [9] as follows. w_1 can be obtained by:

$$w_1(X_1, X_2) = -w_{2,1}(X_1)X_2 \tag{7.7}$$

Then, $w_{1,1},\ w_{1,2}$ and $w_{2,1}$ can be obtained by differentiating w_1 and w_2 or from the shear strain in the classical theory of flexure:

$$E_{12}^0 = \frac{1}{2}(w_{1,2} + w_{2,1}) = 0 \tag{7.8}$$

And, $w_{2,2}$ is found by the stress relaxation condition:

$$T_{22}^0 = c_{21}E_{11}^0 + c_{22}E_{22}^0 + c_{23}E_{33}^0 = 0 \tag{7.9}$$

The determined initial displacement gradients through the procedure described above are:

$$w_{1,1} = -\frac{6P}{\gamma_{11}t^3}(2X_1 - L)X_2 \tag{7.10a}$$

$$w_{1,2} = -\frac{6P}{\gamma_{11}t^3}(X_1^2 - LX_1)X_2 \tag{7.10b}$$

$$w_{2,1} = \frac{6P}{\gamma_{11} t^3}(X_1^2 - LX_1)X_2 \tag{7.10c}$$

$$w_{2,2} = \frac{c_{12}}{c_{11}}\frac{6P}{\gamma_{11} t^3}(2X_1 - L)X_2 \tag{7.10d}$$

$$w_{1,3} = w_{2,3} = w_{3,1} = w_{3,2} = w_{3,3} = 0 \tag{7.10e}$$

7.3.3 Perturbation integral

Consider a homogeneous material body occupying an elastic half-space V with $X_2 > 0$ as shown in Fig. 7.2. The body is free from any deformations and fields. Suppose that the governing equations and boundary conditions allow the propagation of a small-amplitude Rayleigh wave with frequency ω, wave number ξ, phase speed $V_R = \omega/\xi$ in X_1 direction and displacement u_α. Because the region is unbounded, we have an eigenvalue problem with a continuous spectrum. Given a wave number ξ, there always exist a wave with a frequency ω such that $V_R = \omega/\xi$ which depends on material properties only.

When an initial displacement field w with initial stress T^0 and initial strain E^0 is applied, the frequency of surface wave will be perturbed and it can be denoted by $\omega + \Delta\omega$. The change of wave frequency caused by the existence of an initial field is represented by the following integral from a first-order perturbation analysis [17] (see Appendix C for detail):

$$\frac{\Delta\omega}{\omega} \simeq \frac{1}{2\omega^2}\frac{\int_V \hat{c}_{L\gamma M\alpha} u_{\gamma,L} u_{\alpha,M} dV}{\int_V \rho_0 u_\alpha u_\alpha dV} \tag{7.11}$$

where the perturbation of second-order elastic constants under the initial fields are given by:

$$\hat{c}_{L\gamma M\alpha} = T^0_{LM}\delta_{\gamma\alpha} + c_{L\gamma KM} w_{\alpha,K} + c_{LKM\alpha} w_{\gamma,K} + c_{L\gamma M\alpha AB} E^0_{AB} \tag{7.12a}$$

$$T^0_{LM} = c_{LMAB} E^0_{AB} \tag{7.12b}$$

$$E^0_{AB} = \frac{1}{2}(w_{A,B} + w_{B,A}) \tag{7.12c}$$

The quantities T^0_{LM}, E^0_{AB} and w_k are the static biasing stress, strain and displacement field, respectively. The coefficients c_{LMAB} and $c_{L\gamma M\alpha AB}$ are the second- and third-order elastic constants, respectively. And ρ_0 is the mass density.

In addition to the normal stresses due to the bending, the shear stress T^0_{12} exist in non-pure bending case as shown in Fig. 7.3. But, the shear stress T^0_{12} cannot be obtained from the relation Eq. (7.12) because the shear strain E^0_{12} vanishes in the classical Kirchhoff flexural theory. Instead, the shear force T^0_{12} can be found using the first moment $Q(X_2)$ and shear force $V(X_1)$ over a rectangular cross section as follows [18]:

$$T^0_{12} = \frac{V(X_1)Q(X_2)}{I} = -\frac{6P}{t^3}\left(\frac{t^2}{4} - X_2^2\right) \tag{7.13}$$

The coordinate X_2 in Eqs. (7.1) to (7.3) is adjusted to $\bar{X}_2$ to correlate it with the one used in the initial field model where $\bar{X}_2 = X_2 + t/2$.

7.3.4 Material properties and geometrical parameters

For silicon, $\rho_0 = 2,332\text{Kg/m}^3$ and the second-order elastic constants are [19]:

$$c_{11} = 165.7, \quad c_{12} = 63.9, \quad c_{44} = 79.56 \text{ GPa} \tag{7.14}$$

Silicon has 20 non zero ones in its third-order elastic constants and six are independent as given below [19]:

$$c_{111} = -825,\ c_{112} = -451,\ c_{123} = -64,\ c_{144} = 12,\ c_{155} = -310,\ c_{456} = -64 \text{ GPa} \tag{7.15}$$

The other 14 can be obtained from the following relations [20]:

$$\begin{aligned} &c_{113} = c_{112},\ c_{122} = c_{112},\ c_{133} = c_{112},\ c_{166} = c_{155},\ c_{222} = c_{111}, \\ &c_{223} = c_{112},\ c_{233} = c_{112},\ c_{244} = c_{155},\ c_{255} = c_{144},\ c_{266} = c_{155}, \\ &c_{333} = c_{111},\ c_{344} = c_{155},\ c_{355} = c_{155},\ c_{366} = c_{144} \end{aligned} \tag{7.16}$$

The calculated parameters of silicon for the surface acoustic wave solutions Eqs. (7.1) to (7.3) are calculated and given below [21]:

$$V_R = 4,917\text{m/s}, \quad g = 0.4808, \quad h = 0.4556, \quad r = 1.226, \quad \alpha = 58°1' \tag{7.17}$$

It is not required in the theoretical analysis, but in the finite element analysis in following chapter, a piezoelectric thin layer will be used to generate surface wave with IDTs. PZT-5A is chosen and the properties of PZT-5A are given as follows [22]:

$$\begin{aligned} &s_{11} = 16.4,\ s_{12} = -5.74,\ s_{13} = -7.22,\ s_{33} = 18.8,\ s_{44} = 47.5 \times 10^{-12}\text{m}^2/\text{N} \\ &d_{31} = -1.71,\ d_{33} = 3.74,\ d_{15} = 5.84 \times 10^{-10}\text{m/V} \\ &K_{11}^T = 1730,\ K_{33}^T = 1700 \end{aligned} \tag{7.18}$$

The constants s, d and K^T are the compliance, piezoelectric coupling and relative permittivity, respectively. And, the mass density of PZT-5A is 7,750 Kg/m^3.

We are interested in the sensitivity of an accelerometer based on the surface acoustic wave of the frequency $f_0 = 1$ GHz and the corresponding wave length of Rayleigh type wave of silicon is $\lambda_0 = 4,917\mu$m. For the geometrical parameters, the length and thickness of the cantilever as shown in Fig. 7.3 are set to $L = 40\lambda_0$ and $t = 2\lambda_0$, respectively. The distance between transmitter and receiver IDTs is $10\lambda_0$. The plate thickness is enough to prevent any disturbance due to the reflection of wave from the bottom surface. Theoretical analysis

shows the maximum penetrating depth of Rayleigh type wave in silicon is no more than $2\lambda_0$ [21].

7.4 Finite element analysis

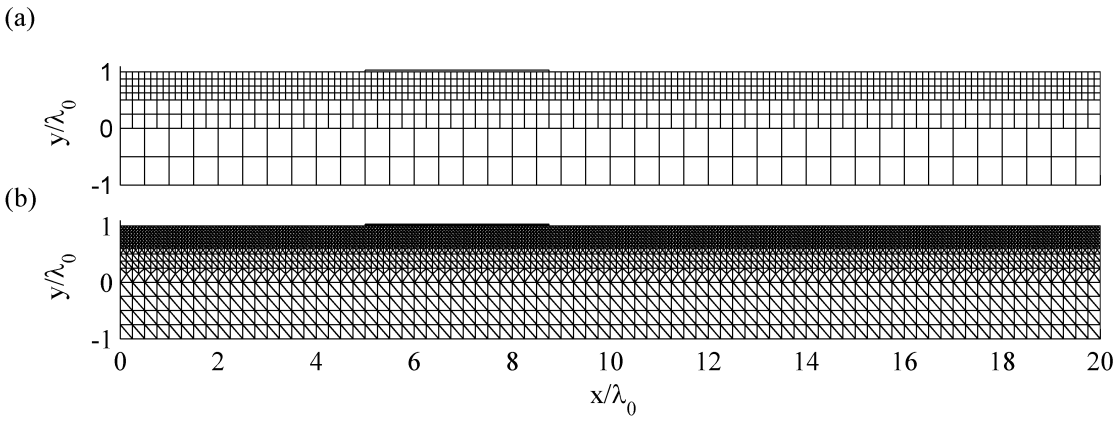

Figure 7.4: Finite element model (a) constructed with finite areas and (b) meshed with triangular elements

We have developed a numerical model to analyze the propagation of the surface acoustic wave under initial bias field using commercial finite element analysis software ANSYS. To simulate the perturbation of surface acoustic wave, the effective second-order elastic constant must be utilized in the model, but this cannot be archived in ANSYS. Instead, the constants calculated in Eq. (7.12) are used. Because the perturbed second-order elastic constants $G_{L\gamma M\alpha}$ are not constant over the its length and thickness, so the model shown in Fig. 7.3 is divided into finite areas as shown in Fig. 7.4. Then, the effective second-order

elastic constant is applied to each area based on the coordinate of an area centroid. The perturbed second-order elastic constant is given by:

$$G_{L\gamma M\alpha} = c_{L\gamma M\alpha} + \hat{c}_{L\gamma M\alpha} \tag{7.19}$$

Because the ANSYS use different form of material properties, the constants and matrices given in Eqs. (7.12), (7.14) and (7.18) are converted by following relationships [23, 24]:

$$[c^E] = [s^E]^{-1} \tag{7.20}$$

$$[\varepsilon^S] = [\varepsilon^T] - [d]^t[s^E]^{-1}[d] \tag{7.21}$$

$$[e] = [s^E]^{-1}[d] = [d]^t[s^E]^{-1} \tag{7.22}$$

where, $c^E,\ s^E,\ \varepsilon^S,\ \varepsilon^T,\ d$ and e are stiffness, compliance, dielectric (evaluated at constant strain), dielectric (evaluated at constant stress), piezoelectric coupling (relating strain/electric field) and piezoelectric coupling (relating stress/electric field) matrices, respectively.

Then, the areas are meshed with triangular elements as shown in Fig. 7.4. 2-D 8-node or 6-node structural solid element PLANE183 is used for the areas of silicon structure so that the elements have the degrees of freedom of displacements u_x and u_y only and for the piezoelectric thin layer, 2-D 8-node coupled-field solid PLANE223 is applied to have degrees of freedom of displacements $u_x,\ u_y$ and electrical volt V. Both elements of PLANE183 and PLANE223 are set to have plane-strain motion and triangular mesh [25].

The computer simulation consists of three stages. First, a static analysis is performed to create initial field in the model. Because the displacement of proof mass is linearly proportional to the applied force P in small displacement from Eq. (7.5), a static displacement is applied to the free end of the cantilever while the left end is fixed. The original second-order elastic constants are used in the first stage. Then, a pre-stressed full transient analysis is

performed. The elastic property of the cantilever is updated with the perturbed one using Eq. (7.19) in this stage. The one period of sinusoidal electrical signal of $V_0 \sin(\omega_0 t)$ and $-V_0 \sin(\omega_0 t)$ are applied to the each pair of fingers of the transmitter IDT to generate an elastic wave in the surrounding of surface. The model is also subjected to the pre-stressing loads created in preliminary static analysis. In last stage, the driving electrical voltages are removed and the surface acoustic wave propagates along the surface of cantilever in both directions. Throughout the simulation, the time step size is set to $T_0/40$ and the element size along the surface is set to $\lambda_0/16$, where T_0 and λ_0 are the period and wavelength of center frequency [26, 27].

Fig. 7.5 shows the propagation of the surface acoustic wave along the strained surface of

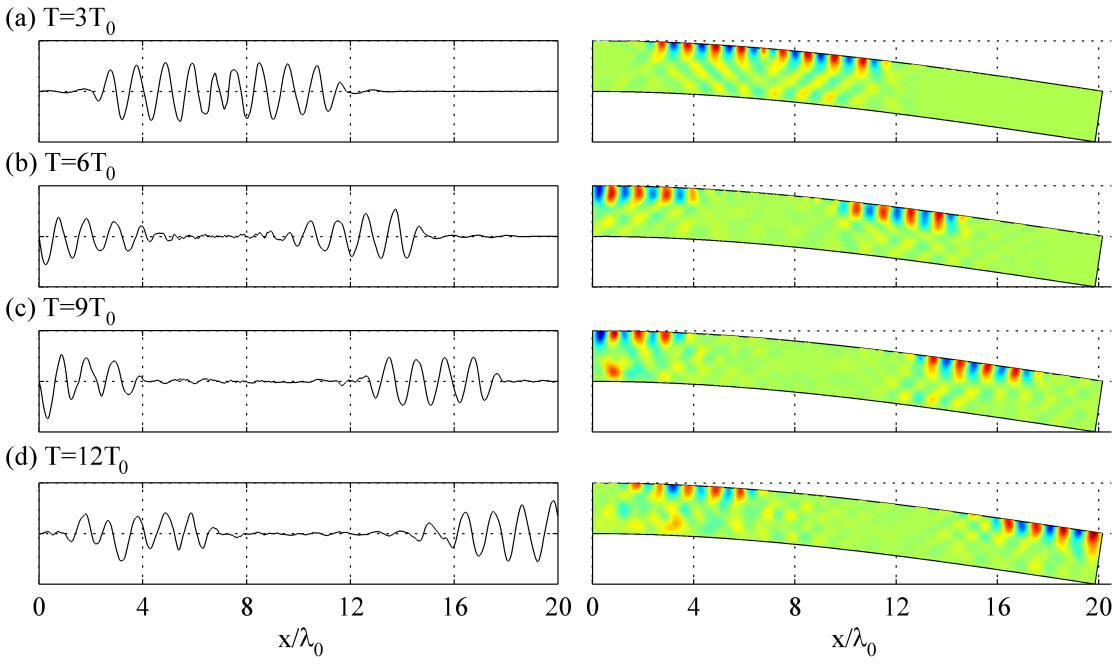

Figure 7.5: Displacement $\bar{u}_2$ due to the propagation of surface acoustic wave

cantilever at the designated time with the distributions of the displacements in the can-

tilever. Because the amplitude of the surface acoustic wave is very small compare to the displacement of initial field, the displacement $\bar{u}_2$ is normalized to the initial displacement field. From Fig. 7.5, a reflection from the left boundary is observed. The reflection can be minimized by putting a damping material around the left boundary or the interferences of reflected wave at the receiver IDT can be filtered out by changing period of the sinusoidal impulse applied to the transmitter IDT.

The results of theoretical and finite element analysis are compared in Fig. 7.6. The fre-

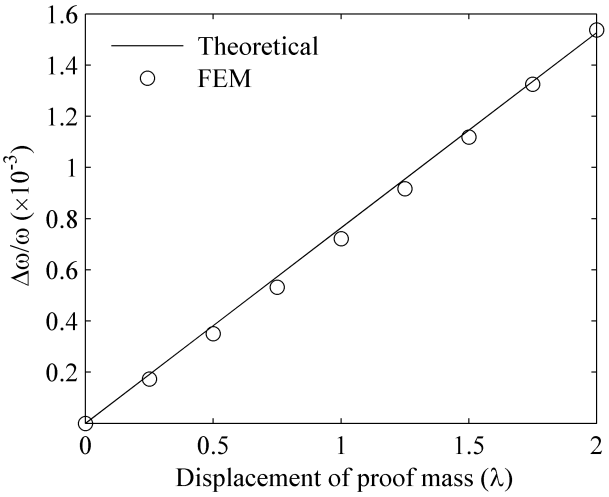

Figure 7.6: Frequency shift of surface acoustic wave under various displacements of proof mass

quency shifts are calculated without an initial field and with initial fields which the displacement of the proof mass is vary from 0 to $2\lambda_0$. The results of both theoretical and finite element analysis show excellent consistency in sensitivity. As shown in the figure, the frequency shifts are all linearly dependent of the displacements of proof mass and the displacement is proportional to the applied force. Therefore, the data of frequency shift

presented in Fig. 7.6 can be converted into the applied external acceleration with the given proof mass and the width of cantilever plate.

7.5 Concluding remarks

The four cantilevered micro SAW-IDT accelerometer is proposed which is operating with a surface acoustic wave propagating over the surface of a silicon plate subjected to non-pure bending. The operating frequency of the accelerometer is 1GHz and the corresponding wavelength is 4.917μm. The frequency shifts in the response to the displacements of proof mass due to the applied loads can be determined locally through the local variations of the effective material constants. The theoretical and the finite element analysis are performed to analyze the effect of the existence of initial biasing fields on the properties of surface acoustic wave. The first-order perturbation theory for small fields superposed on biasing fields is used in the theoretical analysis and the perturbation of second-order elastic constants obtained from the theoretical analysis is utilized in the finite element analysis. The perturbation theory is well interpreted into the pre-stressed full transient finite element model. In both analysis, the frequency shifts under the initial fields of various loading conditions show excellent consistency in sensitivity and can be translated to the applied load or acceleration with an effective proof mass and the cantilever plate width. The sensitivity and sensing range can be easily achieved by controlling the geometrical parameters of sensor structure or material properties for the purpose. The finite element model is now only valid for the small deflection and 2-D plane-strain motion, but it will provide a good insight for the more complicated system design which requires a large scale computation.

Bibliography

[1] E. Benes, M. Gröschl, W. Burger, and M. Schmid, "Sensors based on piezoelectric resonators," *Sensors and Actuators A: Physical*, vol. 48, no. 1, pp. 1–21, 1995.

[2] S. Datta and S. Datta, *Surface acoustic wave devices*. Prentice-Hall Englewood Cliffs, NJ, USA, 1986.

[3] T. M. Gronewold *et al.*, "Surface acoustic wave sensors in the bioanalytical field: Recent trends and challenges," *analytica chimica acta*, vol. 603, no. 2, pp. 119–128, 2007.

[4] K.-y. Hashimoto, *Surface acoustic wave devices in telecommunications: modelling and simulation*. Springer, 2000.

[5] K. Lange, B. E. Rapp, and M. Rapp, "Surface acoustic wave biosensors: a review," *Analytical and Bioanalytical Chemistry*, vol. 391, no. 5, pp. 1509–1519, 2008.

[6] F. Seifert, W.-E. Bulst, and C. Ruppel, "Mechanical sensors based on surface acoustic waves," *Sensors and Actuators A: Physical*, vol. 44, no. 3, pp. 231–239, 1994.

[7] M. Thompson and D. C. Stone, *Surface-launched acoustic wave sensors: chemical sensing and thin-film characterization*. Wiley, 1997.

[8] M. J. Vellekoop, "Acoustic wave sensors and their technology," *Ultrasonics*, vol. 36, no. 1, pp. 7–14, 1998.

[9] Q. Jiang, X. Yang, H. Zhou, and J. Yang, "Analysis of surface acoustic wave pressure sensors," *Sensors and Actuators A: Physical*, vol. 118, no. 1, pp. 1–5, 2005.

[10] J. Yang and X. Zhang, "A high sensitivity resonator pressure sensor," *Sensors and Actuators A: Physical*, vol. 101, no. 3, pp. 332–337, 2002.

[11] H. Subramanian, V. K. Varadan, V. V. Varadan, and M. Vellekoop, "Design and fabrication of wireless remotely readable MEMS based microaccelerometers," *Smart materials and structures*, vol. 6, no. 6, p. 730, 1999.

[12] L. Reindl, I. Shrena, S. Kenshil, and R. Peter, "Wireless measurement of temperature using surface acoustic waves sensors," in *Frequency Control Symposium and PDA Exhibition Jointly with the 17th European Frequency and Time Forum, 2003. Proceedings of the 2003 IEEE International*, pp. 935–941, IEEE, 2003.

[13] S.-M. Chang, E. Tamiya, and I. Karube, "Chemical vapour sensor using a SAW resonator," *Biosensors and Bioelectronics*, vol. 6, no. 1, pp. 9–14, 1991.

[14] H. Tiersten and B. Sinha, "A perturbation analysis of the attenuation and dispersion of surface waves," *Journal of Applied Physics*, vol. 49, no. 1, pp. 87–95, 1978.

[15] R. Stoneley, "The propagation of surface elastic waves in a cubic crystal," *Proceedings of the Royal Society of London. Series A. Mathematical and Physical Sciences*, vol. 232, no. 1191, pp. 447–458, 1955.

[16] H. Tiersten and B. Sinha, "Temperature dependence of the resonant frequency of electroded doubly-rotated quartz thickness-mode resonators," *Journal of Applied Physics*, vol. 50, no. 12, pp. 8038–8051, 1979.

[17] H. Tiersten, "Perturbation theory for linear electroelastic equations for small fields superposed on a bias," *The Journal of the Acoustical Society of America*, vol. 64, p. 832, 1978.

[18] J. Gere and B. Goodno, *Mechanics of Materials*. Cengage learning, 2008.

[19] H. Hellwege, *Numerical Data and Functional Relationships in Science and Technology*, vol. 11/15. Springer-Verlag, Berlin, Heidelberg, New York, 1987.

[20] D. F. Nelson and D. Nelson, *Electric, optic, and acoustic interactions in dielectrics*. Wiley New York, 1979.

[21] D. Royer and E. Dieulesaint, *Elastic Waves in Solids, Free and Guided Propagation, vol. 1*. Springer, Berlin, 1999.

[22] J. F. Tressler, S. Alkoy, and R. E. Newnham, "Piezoelectric sensors and sensor materials," *Journal of electroceramics*, vol. 2, no. 4, pp. 257–272, 1998.

[23] ANSYS® Academic Research, Release 11.0, Help System, Theory Reference Manual, ANSYS, Inc.

[24] Y. Kim, L. Cai, T. Usher, and Q. Jiang, "Fabrication and characterization of THUNDER actuators: pre-stress-induced nonlinearity in the actuation response," *Smart Materials and Structures*, vol. 18, no. 9, p. 095033, 2009.

[25] ANSYS® Academic Research, Release 11.0, Help System, Element Reference Manual, ANSYS, Inc.

[26] G. Xu, "Direct finite-element analysis of the frequency response of a YZ lithium niobate SAW filter," *Smart materials and structures*, vol. 9, no. 6, p. 973, 2000.

[27] G. Xu and Q. Jiang, "A finite element analysis of second order effects on the frequency response of a SAW device," *Journal of intelligent material systems and structures*, vol. 12, no. 2, pp. 69–77, 2001.

Appendix C

Perturbation integral

The equation for the first perturbation of the eigenvalue is given by:

$$\Delta_\mu = \frac{H_\mu}{2\omega_\mu}, \quad \omega = \omega_\mu - \Delta_\mu \tag{C.1}$$

where ω_μ and ω are the unperturbed and perturbed eigenfrequencies, respectively.

$$H_\mu = -\int_V \tilde{K}^n_{L\gamma} g^\mu_{\gamma,L} dV \tag{C.2}$$

where V is the undeformed volume of the plate and

$$\tilde{K}^n_{L\gamma} = \hat{c}_{L\gamma M\alpha} g^\mu_{\alpha,M} \tag{C.3}$$

$g^\mu_{\alpha,M}$ is the normalized mechanical displacement vector and $\tilde{K}^n_{L\gamma}$ is the position of the Piola-Kirchhoff stress tensor resulting from the biasing state in the presence of the $g^\mu_{\alpha,M}$.

$$\hat{c}_{L\gamma M\alpha} = T^0_{LM}\delta_{\gamma\alpha} + c_{L\gamma KM} w_{\alpha,K} + c_{LKM\alpha} w_{\gamma,K} + c_{L\gamma M\alpha AB} E^0_{AB} \tag{C.4}$$

$$T^0_{LM} = c_{LMAB} E^0_{AB} \tag{C.5}$$

$$E^0_{AB} = \frac{1}{2}(w_{A,B} + w_{B,A}) \tag{C.6}$$

The quantities $T^0_{LM},\ E^0_{AB}$ and w_k are the static biasing stress, strain and displacement field, respectively. The coefficients c_{LMAB} and $c_{L\gamma M\alpha AB}$ are the second- and third-order elastic constants, respectively.

The present position y is related to the reference position X by

$$y(X_L, t) = X + w(X_L) + u(X_L, t) \tag{C.7}$$

The normalized solutions g^μ_γ and $\hat{f}^\mu$ are defined by

$$g^\mu_\gamma = \frac{u^\alpha_\gamma}{N_\mu} \tag{C.8}$$

$$\hat{f}^\mu = \frac{\tilde{\varphi}^\mu}{N_\mu} \tag{C.9}$$

$$N^2_\mu = \int_V \rho u^\mu_\gamma u^\mu_\gamma dV \tag{C.10}$$

where u^μ_γ and $tilde\varphi^\mu$ are the mechanical displacement and electric potential, respectively, which satisfy the equations of linear piezoelectricity subject to the appropriate boundary conditions.

$$\tilde{K}^0_{L\gamma} = c_{L\gamma M\alpha} u_{\alpha,M} + e_{ML\gamma}\tilde{\varphi}_{,M} \tag{C.11}$$

$$\tilde{D}^0_L = e_{ML\gamma} u_{\gamma,M} - \varepsilon_{LM}\tilde{\varphi}_{,M} \tag{C.12}$$

$$\tilde{K}^0_{L\gamma,L} = \rho\ddot{u}_\gamma \tag{C.13}$$

$$\tilde{D}^0_{L,L} = 0 \tag{C.14}$$

The quantities $\tilde{K}^0_{L\gamma},\ \tilde{D}^0_L,\ e_{ML\gamma}$ and ε_{LM} denote the linear stress tensor, the electric displacement vector and the piezoelectric and dielectric constants, respectively, and ρ is mass density. With Eqs. (C.2) and (C.3),

$$H_\mu = -\int_V \hat{c}_{L\gamma M\alpha} g^\mu_{\alpha,M} g^\mu_{\gamma,L} dV \tag{C.15}$$

Since $g^{\mu}_{\alpha,M}$ is the normalized surface wave mode shape and $\hat{c}_{L\gamma M\alpha}$ depends on the biasing state, H_μ can be evaluated when the surface wave mode shape and biasing state are known. Thus, evaluation of Eq. (C.1) with Eq. (C.15) gives the perturbation integral

$$\frac{\Delta\omega}{\omega} \simeq \frac{1}{2\omega^2} \frac{\int_V \hat{c}_{L\gamma M\alpha} u_{\gamma,L} u_{\alpha,M} dV}{\int_V \rho_0 u_\alpha u_\alpha dV} \tag{C.16}$$